Shear-normal coupled deformations in anisotropic structured materials

Thesis by
Purna Chandra Jagannadh (Jag) Kumar Boddapati

In Partial Fulfillment of the Requirements for the
Degree of
Doctor of Philosophy in Mechanical Engineering

Caltech

CALIFORNIA INSTITUTE OF TECHNOLOGY
Pasadena, California

2025
Defended August 09, 2024

ACKNOWLEDGEMENTS

I am deeply grateful to have had Prof. Chiara Daraio as my thesis advisor. I treasured every conversation we shared during our research meetings and our interactions outside of them. Every meeting with her was an opportunity to learn something new. Chiara has a great way of making each discussion both energizing and thought-provoking while trying to push the boundaries of my creativity. I always eagerly anticipated our weekly research meetings. She was incredibly supportive, offering me a great deal of freedom in my research endeavors. She also guided me to become a better researcher, emphasizing the importance of being humble, seeking help, and collaborating with others. I continue to learn from her, including the art of engaging conversations across diverse scientific topics, delivering captivating lectures, and breaking down a huge task into simple tangible steps.

I would also like to extend my gratitude to my thesis committee. Prof. Guruswami Ravichandran has played a pivotal role in shaping my academic journey and offered invaluable support. During my initial years of graduate school, Ravi served as my interim advisor, and as an examiner for my qualification and candidacy exams. His expertise in experimental design and experimental techniques significantly led me to work on the virtual fields method. I will always remember his encouraging way of saying "excellent" whenever I update him on my research progress. Discussions with Prof. Kaushik Bhattacharya greatly enhanced my theoretical understanding of solid mechanics. Kaushik's ME221 class was very helpful for my research on understanding extremal composites. The group meetings with Ravi and Kaushik were a highlight of my first year, exposing me to various branches of solid mechanics. Additionally, Prof. Michael Ortiz's AE214 class significantly deepened my understanding of computational mechanics. I strived to adhere to Michael's philosophy of "think before you do (or code)."

I would like to thank several collaborators who guided me in this process. I am very grateful to have worked with Dr. Liwei Wang (Northwestern), Prof. Wei Chen, Prof. Cate Brinson, Dr. Ke Liu, Dr. Doksoo Lee (Northwestern). All the metamine project meetings have been enlightening, teaching me about data-driven design in metamaterial research. It was a privilege to collaborate with Dr. Moritz Flaschel (ETH Zurich), Prof. Laura De Lorenzis (ETH Zurich), and Prof. Siddhant Kumar (TU Delft). Moritz generously dedicated an extensive time to our Zoom interactions, patiently addressing my questions and promptly scheduling meetings despite the time zone differences. Prof. De Lorenzis serves as a remarkable role model, exemplifying humility in the pursuit of groundbreaking research. Dr. Alex Ogren is another chap I cherished having conversations with any day on any topic. Discussions with him taught me so much about machine learning, wave mechanics, plants, biking, and many more things. Dr. Andrew Akerson and Dr. Vatsa Gandhi

provided key inputs into my research when I was getting settled with my thesis research and I am very grateful for that. I would also like to thank Dr. Filippo Agnelli (École Polytechnique) for teaching me digital-image correlation and sharing his DIC codes.

Being part of the Daraio research group, which is very diverse, I learned a lot about scientific topics outside solid mechanics. I deeply appreciate the invaluable assistance provided by Sai Sharan Injeti, Connor Mcmahan, Alex Ogren, and Petros Arakelien. Petros was really fast in delivering 3D printed parts in a very timely manner and is there for help on any matter related to hardware troubleshooting. I would like to thank Jihoon Ahn for his help in the design of experimental setups and the electronics integration. I also want to thank Gunho Kim, Tracy Lu, Sujeeka Nadarajah, Max Kudisch, Tommasso Magrini, Hesham Zaini, Chelsea Fox, Joong Hwan, Anya Wallace, Joaquin Garcia Suarez for being such great colleagues. I would also like to thank Dr. Skylar Wei from Burdick's lab. Her help was very crucial in analyzing the potential design mistakes with my experimental setup.

Guiding undergraduates Perry, Evan, and America as summer research mentees was an enriching experience. Throughout this process, I gained valuable insights, particularly in enhancing my communication skills during mentorship. My experience as a teaching assistant for Domniki Asimaki and Ares Rosakis significantly enhanced my ability to convey complex concepts effectively. I would also like to thank the MCE staff: Lynn Seymour, Jenni Campbell, Carolina Oseguera, Sonya Lincoln, Stacie Takase, and, Holly Golcher. I want to thank Mr. Ross Brown for the first-year von Karman Graduate Fellowship. His generosity has significantly fueled my passion for research and science. All the special solid mechanics seminars on special occasions were truly the icing on the cake. I will dearly miss those gatherings in GT135. Every instructor I learned from, particularly Justin Bois, imparted valuable insights into intuitive thinking. All my cohort especially Rigoberto Moncada Lopez, Prithvi Akella, and Eric Ocegueda, were great to hang out with any time of the day. Prithvi was a great stress buster being my roommate initially and then as an office mate. His pertinent question 'what next' couldn't irritate me more. I would also like to acknowledge the support from the International Student Program (ISP), especially Laura and Daniel. The library's tech lab, which provided invaluable assistance with 3D printing during lockdown, deserves acknowledgment. Additionally, the Hixon Writing Center played a crucial role in refining my scientific writing skills.

I'd like to express my heartfelt appreciation to the Caltech Cricket Club (CCC). During my tenure as an officer at CCC, the team taught me the delicate balance of valuing others' opinions while standing firm on my own ideas. Dr. Siddharth Jain, Dr. Nachiket Naik, Dr. Sumit Goel, and Dr. Akshay Sridhar were exceptional companions, creating countless cherished memories and enriching my journey beyond research. I also gained valuable scientific insights during our drives

to match grounds. The on-field banter, such as "Keeper has no clue, Nash equilibrium, Bella Ciao" is a unique part of being on Caltech's team. Having witnessed different generations of players, the team feels like a family away from home.

I would also like to acknowledge my non-cricket workout friends at different stages: Dr. Forte Shinko, Dr. Sunghyuk Park, Dr. Ashmeet Singh, Frid Fu, Dr. Kate Huang, Berthy Feng, and Dr. Danilo Kusanovic. I would also like to thank Ashok Vardhan, Krishna Phanindra, Somu Dhulipala, Dr. Deepan Kishore Kumar, Dr. Harsha Reddy Narravula, Dr. Anushri Dixit, Prachi Thureja, and Dr. Akshay Joshi for their friendship. I am also glad to be part of the Caltech Surf Club and the Caltech Badminton Club. I would also like to acknowledge Jan Boyd for being such a great host and friend. Her wisdom and the experiences shared by her and her friends have taught me valuable life lessons during my stay at her place. And a special shoutout to my trusty bike, *Sparrow*, which has accompanied me on numerous adventures into the woods.

I would also like to thank my undergraduate teachers and mentors at IIT Madras, especially Prof. Ratna Kumar Annaattuala, Prof. K. Ramesh, and Prof. Sathyan Subbiah. Their guidance instilled in me a research-oriented mindset. Prof. Ratna's friendly demeanor and inspiring talks on research philosophy continue to motivate me everyday. I am equally thankful to Prof. Liang Pan and Prof. Justin Weibel, who graciously allowed me to spend time with them during my undergraduate internship at Purdue. I would also like to thank Dr. Edvin Cetegen from the Assembly and Test Technology Development team at Intel Corporation. During my internship, his mentorship emphasized scientific rigor and attention to detail, and helped shape me into a more focused researcher.

I extend my heartfelt gratitude to Sourya Varenya, my best friend and an exceptionally intelligent individual. His unwavering encouragement motivated me to embark on my Ph.D. journey, and our bond allows me to confide in him freely. I am immensely thankful for the countless hours he spent critiquing me, addressing critical personal aspects that ultimately enabled me to perform at my best. Finally, I express deep appreciation to my parents, sister, and especially my grandmothers. Their nurturing support sustained me during challenging times, shaping my path and contributing significantly to my achievements. Family has been my anchor, providing unwavering love and strength throughout this journey.

"I like to be buckled, tensed, stretched, wrinkled, dislocated, defected, tortured, bent, and broken. In the end, everything is solid mechanics" - Jagannadh

<div align="center">

ఎందరో మహానుభావులు అందరికీ వందనములు
Salutations to all those great men in this world.

</div>

ABSTRACT

The advent of additive manufacturing has allowed the design and engineering of a new class of materials known as metamaterials, or structured/architected materials. These metamaterials exhibit unique functionalities, such as ultrahigh strength-to-density ratios, which their base materials cannot achieve. Often designed to exhibit near-isotropic behavior, metamaterials derive their special properties from the distinctive deformation, dynamic motion, and elastic energy distribution of their micro- and meso-architectures. However, designing metamaterials for anisotropy, despite their ability to attain unique properties, is challenging. Fully characterizing anisotropic stiffness in planar loading requires six independent elastic tensor moduli. This high number of independent elastic stiffness parameters also expands the design space of structured materials and leads to unusual phenomena, such as materials that can shear under uniaxial compression. This direction-dependent shear-axial coupling is crucial for many applications such as shape-morphing, elastic wave manipulation devices and impact redirection.

This thesis aims to understand the fundamental limits of shear-normal coupled deformations in anisotropic structured materials. Currently, there are no established upper and lower bounds on anisotropic moduli achieving extreme elastic anisotropy, similar to the Hashin-Shtrikman bounds in isotropic composites. This range is known as G-closure and provides limits for the achievable tensors. To date, there are no experimental methods that can measure the stiffness parameters of fully anisotropic structured materials from a single experiment. To address these challenges, we first introduce a method to generate two-phase periodic anisotropic unit cell geometries and construct a database of unit cells with a diverse range of effective elasticity tensors. The constructed database is compared with the properties achieved by hierarchical laminates and identify the regions where hierarchical designs are necessary to reach a specific extreme elasticity tensor.

We then propose an experimental methodology to evaluate the anisotropic material properties. Our technique, which utilizes the virtual fields method, allows for the determination of six separate stiffness tensor parameters of two-dimensional structured materials using just one tension test. This method thus eliminates the need for multiple experiments as is typical in traditional methods. We show the accuracy of our method using synthetic data generated from finite element simulations as well as by conducting experiments on four additively manufactured specimens. The approach requires no stress data and uses the full-field displacement data measured using digital image correlation and global force data.

We present a method for creating functionally graded anisotropic structures that smoothly transition between unit cells with distinct patterns. Isotropic materials with spatially varying density gradients

have been shown to exhibit unique characteristics such as superior energy absorption. However, achieving smooth spatial gradients in the anisotropic mechanical properties while ensuring the connectivity of adjacent meso-architectures is non-trivial. This method allows for independent control of several functional gradients, such as porosity, anisotropic moduli, and symmetry. We show that certain nonlinearly graded structures when designed with unit cells positioned at distinct corners of the property space boundary exhibit novel mechanical behaviors. We conclude by designing specific functionally graded structures that demonstrate peculiar behaviors such as selective strain energy localization, localized rotations, compressive strains under tension, and longitudinal-shear wave mode conversion.

PUBLISHED CONTENT AND CONTRIBUTIONS

[1] Jagannadh Boddapati and Chiara Daraio. Planar structured materials with extreme elastic anisotropy. *Under Review*, July 2024. doi: 10.48550/arXiv.2407.19136.
Chapters 3 and 5 have been adopted from this work. J.B. participated in the conception of the project, performed finite element analysis and experiments on additively manufactured specimens, prepared the data, and participated in the writing of the manuscript.

[2] Jagannadh Boddapati*, Moritz Flaschel*, Siddhant Kumar, Laura De Lorenzis, and Chiara Daraio. Single-test evaluation of directional elastic properties of anisotropic structured materials. *Journal of the Mechanics and Physics of Solids*, 181:105471, December 2023. doi: 10.1016/j.jmps.2023.105471.
*Chapters 2 and 4 have been adopted from this work. J.B. participated in the conception of the project, performed finite element analysis, performed experiments & analyzed experimental data using digital image correlation, and participated in the writing of the manuscript. * Equal contribution.*

[3] Jagannadh Boddapati, Alexander C. Ogren, Jihoon Ahn, Gunho Kim, and Chiara Daraio. Shear-longitudinal wave mode conversion through functionally graded anisotropic metamaterials. *In Preparation*, August 2024.
Chapter 6 has been adopted from this work. J.B. participated in the conception of the project, performed design and finite element analysis, prepared the data, and participated in the writing of the manuscript.

[4] Liwei Wang, Jagannadh Boddapati, Ke Liu, Ping Zhu, Chiara Daraio, and Wei Chen. Mechanical cloak via data-driven aperiodic metamaterial design. *Proceedings of the National Academy of Sciences*, 119(13):e2122185119, March 2022. doi: 10.1073/pnas.2122185119.
This work has not been adapted for this thesis, but a brief summary is included in Chapter 1 as a case study. J.B. participated in the conception of the project, performed experimental validation using digital image correlation, and participated in the writing of the manuscript.

TABLE OF CONTENTS

LIST OF ILLUSTRATIONS

LIST OF TABLES

Chapter 1

INTRODUCTION

1.1 Research objectives

The overarching goal of this thesis is to understand the fundamental limits of shear-normal coupled deformations in anisotropic structured materials in the quasi-static and dynamic regimes. The thesis addresses the following questions.

1.2 Motivation

The discovery of new materials throughout history presented a significant shift in the living standards of human civilization. Metals like bronze (an alloy of copper and tin) and steel (an alloy of iron and carbon) allowed for the creation of more intricate and tougher tools and weapons compared to the Stone Age. The semiconductor industry has benefitted from the invention of transistors in 1947 by introducing defects in Silicon, leading to the invention of computers. These breakthroughs have catalyzed advancements in various domains, such as bridges, railroads, spacecrafts, aircraft, and automobiles. By unlocking new properties and functionalities, materials have enabled innovations that enhance our well-being, foster economic growth, and shape the course of progress.

Initially, efforts were directed towards understanding the underlying mechanisms of the intricate mechanical properties such as ductility that these materials exhibit, rather than engineering those properties. However, the invention of high-performance carbon fibers from polyacrylonitrile (PAN) marked a significant shift. This advancement enabled engineers to tailor mechanical properties, resulting in carbon fiber reinforced polymer matrix composites (CFRPs) with a high strength-to-weight ratio. The combination of carbon fibers' high tensile strength and the versatility of the resin matrix makes carbon fiber composites indispensable especially in the aerospace and automotive industries.

The advent of additive manufacturing has further allowed the design and engineering of a new class of materials known as metamaterials, or structured/architected materials. Metamaterials derive their effective properties from both the micro- and meso-structure and their constitutive material properties. Metamaterials have been studied in various domains of physics, such as electromagnetism, leading to the discovery of materials that exhibit unconventional properties like negative refractive index [7]. These electromagnetic metamaterials have been devised for applications such as invisibility cloaks, flat lenses, and miniaturized antennas. Mechanical metamaterials are a special branch of metamaterials that derive special functionalities from their peculiar deformation,

dynamic motion and/or elastic energy distribution [8–12]. hey often exhibit mechanical properties that deviate from those of their constituent materials, showing unusual behaviors, such as negative Poisson's ratios [13, 14], vanishing shear moduli [15], and negative refractive indices [16]. Thus, metamaterials open up a vast design space and enable a plethora of new functionalities that were previously unattainable with conventional materials. The ability to tailor their electromagnetic, mechanical, and optical properties provides engineers and scientists with unprecedented opportunities to create materials with customized behaviors and functionalities. Metamaterials are an exciting area of research with immense potential for future technological advancements.

Structured materials are not an entirely new concept. Foams, for example, also derive their properties from their mostly hollow microstructure. However, due to the stochastic nature of the foams' geometries, their elastic properties are mostly dependent on the volume fraction of the material [17]. In order to obtain more control on the effective materials' properties of foam-like composites, scientists have began to explore the design and fabrication of lattice structures (see Fig. 1.1). Lattice structures are often periodic assemblies of repeating unit cells, which are designed as a connection of strut elements between nodes distributed along the centers and corners of a cube. Common geometries that have been extensively studied include kelvin, octet, and diamond unit cells [18]. Depending on the number of interconnections between different struts, these structures are either bending dominated and flexible or stretch dominated and rigid. By controlling the geometry of individual struts, it is possible to tune the elastic properties to a varied degree of freedom compared to conventional foam structures or other composite materials [1]. In addition to their tunability, metamaterials have been attracting a lot of attention in engineering because they are lighter weight than bulk solids and can exhibit unconventional mechanical properties, high strength-to-weight ratio [19], acoustic bandgaps [20], shock absorption [21], mechanical cloaking [4, 22], etc. that are otherwise absent in conventional materials.

Among several mechanical properties of the metamaterials, elasticity tensors provide crucial information related to the energy density stored in the material, and directions in which the structure is most stiff or soft to the applied loads. The elastic properties of structured materials are strongly dependent on the geometry of the material's internal architecture. By carefully selecting the geometry of the micro- and meso- structures with varying symmetries beyond lattice structures [15, 23–27], metamaterial designers can explore novel anisotropy classes in the material responses. In such structures with direction-dependent mechanical behavior, the number of descriptors of the elastic properties (e.g., the elasticity constants) will be high (up to 21 independent constants), compared to the case when the properties are direction-independent (2). In turn, the presence of rich anisotropy expands the materials' functionality space, by exploiting coupled-deformation mechanisms that are non-existent in symmetric structures. Examples include metamaterials that

twist under compression [24, 28–30], shear under thermal loading [31] and shape-morph [32–34]. In the dynamic regime, anisotropy allows observing phenomena like conical refraction [35] and control of broadband elastic waves [36–38].
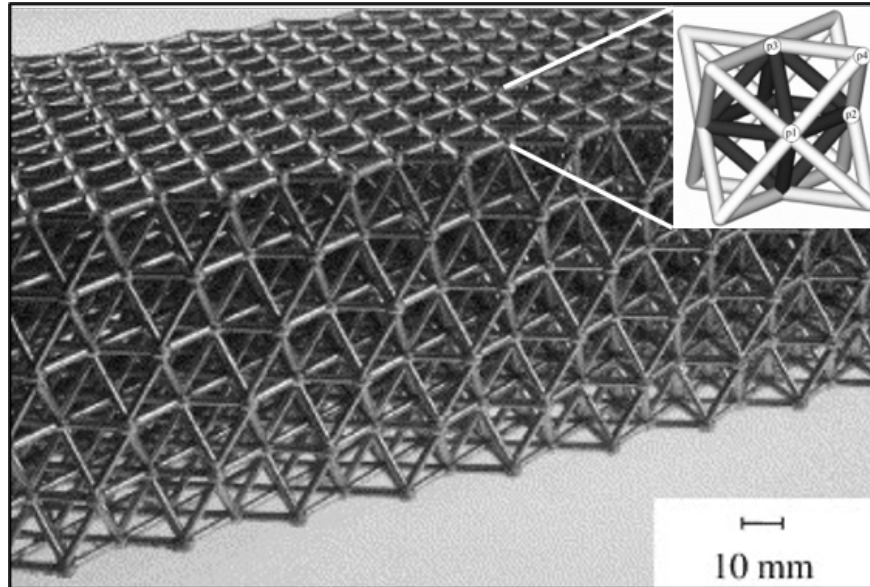
Figure 1.1: An example structured material based on an octet-strut unit cell shown in the inset. The structured material is fabricated using an aluminum alloy. Adopted from [1].

1.3 Research challenges

The ability to fabricate arbitrarily complex composite materials thus opens the door to a richer, relatively unexplored range of elastic properties, such as shear-normal coupling. However, systematic tools for characterizing such properties remain underdeveloped. In engineering design, our intuition regarding specific architectural patterns and their direct impact on elastic coupling constants is still limited. Questions arise: Which architectural features directly influence specific elastic parameters? How can we efficiently evaluate all elastic properties after material fabrication, minimizing the number of experiments? Additionally, what fundamental bounds exist for these elastic parameters? Furthermore, how can we engineer architectures to incorporate gradients in anisotropic properties?

Unit cell design challenges

Recent experimental work has demonstrated shear-normal coupled structures for instance by creating structures that rotate when compressed [2, 39, 40]. These structures, however exhibit diminishing rotations as more unit cells are added Fig. 1.2. Fewer symmetries exist in all of these structures, leading to such shear-normal (torsion-compression) coupling. While, such simple struc-

tures provided initial proof-of-concept experimental validation on coupled deformations, much has not been understood on the fundamental limits of these coupled deformations. Given a vast selection of materials and designs to print from, are there specific designs that provide the most coupling that is predicted using theory? On one hand, achieving a complete characterization of the parameter space in terms of the moduli becomes exceedingly difficult in the absence of a unique parametrization of the input geometry. On the other hand, defining how close the obtained designs are to the theoretical bounds is also challenging, as little is known about the theoretical limits of anisotropic elastic moduli (no known closed-form expressions) [41].
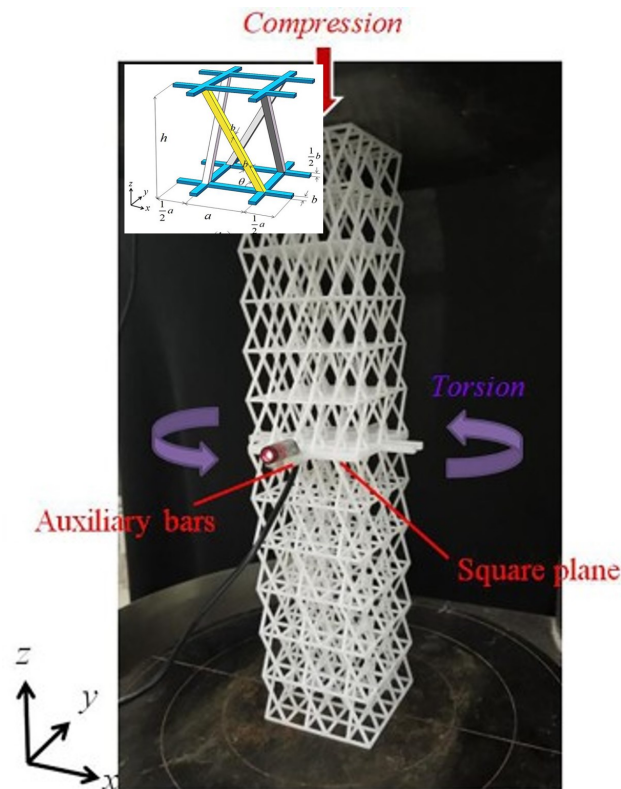
Figure 1.2: Example of a 3D metamaterial undegoing torsion due to compression. The unit cell exhibits less symmetries compared to an octet-truss shown in Fig. 1.1. Adopted from [2].

Experimental validation challenges

In experiments, characterizing these many independent elastic parameters is quite complex. Indeed, the presence of shear-normal coupling makes it hard to measure even one of the six parameters from a single experiment. Prior work suggested different approaches to experimentally measure the elastic parameters for different anisotropy classes [42–47]. However, most of these approaches focus on measuring the stiffness tensor components when the off-diagonal, shear-normal coupling, components are absent. In addition, several of these approaches require multiple experimental

steps. For example, techniques based on the detection of different acoustic wave speeds along different material directions involve multiple tests and assume a certain material symmetry in predicting elastic parameters [48, 49]. To date, there are no experimental methods that can measure the stiffness parameters of fully anisotropic structured materials from a single experiment.

Functionally graded metamaterial design challenges

Functionally graded structures have been shown to exhibit unique mechanical behavior such as avoiding shear-banding [50, 51] and, mimicking bone stiffness [52]. To generate such structures, the parametrization associated with the structure such as truss thickness is often adjusted [53–55] (see Fig. 1.3. Therefore, these approaches are particularly effective in controlling the isotropic Young's Modulus, relative density, and to some extent, the degree of orthotropic elasticity [56, 57]. However, achieving smooth spatial gradients in the anisotropic mechanical properties while ensuring the connectivity of adjacent unit cells is challenging. Further, the unique mechanical behaviors explored by these graded structures, designed with anisotropic unit cells are not well studied.

Figure 1.3: Example of a functionally graded lattice material. The gradients are created by changing the lattice parameters. Adopted from [3].

1.4 Thesis outline

In this thesis, the research challenges discussed previously are addressed. The rest of the thesis is organized as follows. In the following Section 1.5, a case study on the design of mechanical cloaks is presented from the perspective of anisotropic metamaterials.

In Chapter 2, we first present the theory of linear elasticity relevant to this work. Then, we propose a method for generating diverse anisotropic unit cell geometries. We then present the details of the experimental setup used for testing additively manufactured specimens and evaluation of the mechanical properties of the constituent materials. We also discuss the method of converting designs to STL files suitable for additive manufacturing. We finally present, the digital image correlation approach followed in this thesis.

In Chapter 3, we estimate the range of anisotropic stiffness tensors achieved by single-scale two-dimensional structured materials. We compare the property ranges reached by these single-scale architected materials with the extensive design space achieved by hierarchical lamiantes. We identify regions in the property space where hierarchical designs or the use of two anisotropic constituent phases are necessary to cover a wide property space, particularly focusing on off-axis shear-normal coupling parameters. The bounds estimated alongside the unit cell database could serve as a design tool for the design of extremal metamaterials.

In Chapter 4, we present an approach to identify the 6 independent elastic material parameters of plane anisotropic elasticity from a single experiment, using the virtual fields method. This approach allows for identifying shear-normal coupling parameters experimentally, a task that has remained challenging so far. We first demonstrate the effectiveness of our method using numerically generated data from a single tension test. We then experimentally validate the method on additively manufactured specimens, by measuring full-field displacement data and traction forces. We show that our method is effective for materials that include at least 10 repeated unit cells in their structure, to satisfy homogenization conditions. We calculate the uncertainty in the identification estimation of the material parameters using Bayesian linear regression.

In Chapter 5, we present a method for creating functionally graded structures that smoothly transition between unit cells with distinct patterns. When these graded structures are designed with unit cells positioned at distinct corners of the boundary of the property space, they demonstrate unique mechanical behaviors. Specific graded designs are numerically studied to observe behaviors such as selective energy localization, compressive strains under tension, and localized rotations. The designs exhibiting localized rotations under tensile loading are further experimentally validated through tensile tests on additively manufactured specimens. We introduce the concept of supercell designs, which were created by tessellating an entire annular graded structure. Those supercell designs are observed to undergo non-local interactions leading to their length-scale dependence.

In Chapter 6, we study the dispersive behavior of the unit cells using dynamic numerical homogenization. We first show that the fundamental modes of the anisotropic unit cells are hybridized between longitudinal and shear modes. Then, we show the shear waves can be converted to longitudinal waves and vice versa over a broad range of frequencies using functionally graded structures.

In Chapter 7 possible future extensions of the work in this thesis are discussed. In Appendix A, assembly, operation and maintenance of selective laser sintering technology-based 3D printer is discussed.

1.5 Case study: Mechanical cloak design

Mechanical cloaks are materials engineered to control the deformations and the distribution of forces within and around solids. Mechanical cloaks could be used to protect sensitive and delicate objects or to make rigid electronic components more comfortable to wear. In several systems, we observe this need for control of the distribution of forces, stresses, and structural deformations. For example, ants excavate soil without disturbing the structural integrity of their tunnels by removing those grains that are only subjected to lower compressive forces. The art in the game of Jenga involves rearranging blocks in a pile while preserving the pile's stability. Engineers devise redundant and alternate load pathways in structures such as bridges, to efficiently and safely direct forces from their point of application to the bridge's foundation. Using structured materials to tune local mechanical properties in mechanical cloaks, it is possible to conceal objects from external forces and deformations [4, 22].

Mechanical cloaks are the elastic counterparts of optical invisibility cloaks. A simpler example of a mechanical cloak is an acoustic cloak, which only controls pressure waves (or sound). Just like optical cloaks that render objects invisible using the laws of refraction, acoustic cloaks render the sound undetectable to an observer situated inside the cloaked area or prevent reflections of acoustic waves from an object embedded in the cloak. To design acoustic cloaks, engineers optimize the distribution of bulk modulus and density. The governing equations in the case of acoustic cloaks are scalar PDEs. To solve scalar PDEs on complex domains, and in turn to design acoustic cloaks, a common mathematical technique called conformal mapping, is employed.

In mechanical cloaks, deformations are influenced concurrently by both the hydrostatic and the deviatoric stresses. As a result, the governing equations for the mechanical cloaks, given by the equations for the balance of linear and angular momentum, involve both axial and shear stresses as variables. These variables depend on multiple mechanical parameters in the cloaking region. Therefore, conformal mapping cannot be used in mechanical cloaks as the governing equations are not scalar. In one of the first studies of mechanical cloaks, researchers simplified this problem

while cloaking cylindrical objects using a special class of structures that support only hydrostatic stresses. However, a fundamental necessity in shielding arbitrarily shaped cloaking objects is to fill the cloaking region with inhomogeneous, anisotropic mechanical properties. Anisotropic materials respond differently to different directions of loading. Hence, they exhibit a higher degree of independent control over axial and shear modes of deformation making them excellent candidates for the cloak design. By arranging the building blocks with suitable and distinct anisotropic mechanical properties, the cloaking region is generated Fig. 1.4.
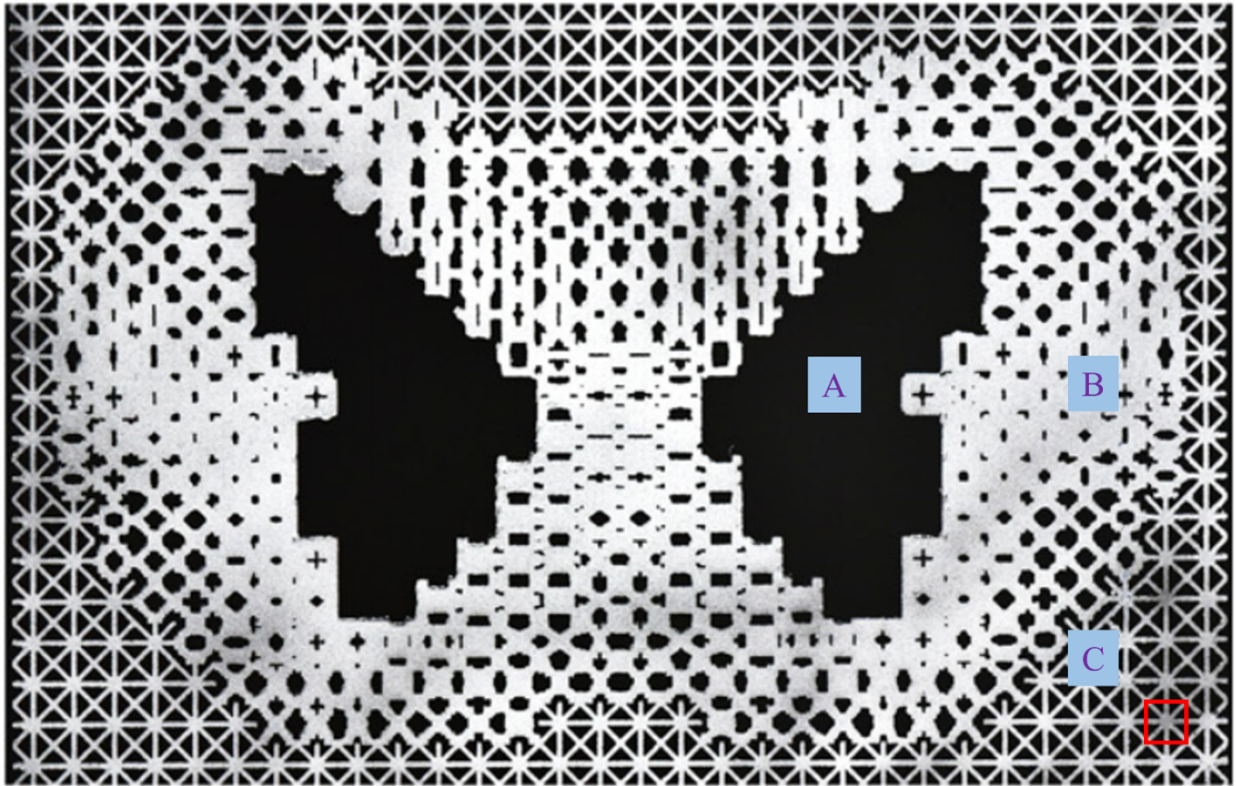
Figure 1.4: A mechanical cloak consists of three distinct regions. A region of the structure that needs to be shielded is named the cloaking object (A) which in this case is a void; the region that assists with shielding is named the cloaking region (B); and the region that surrounds the cloaking region, is named the surrounding region (C). An efficiently designed cloaking region would make the cloaking object unsusceptible to externally applied forces. The design procedure entails modifying the mechanical properties spatially within the cloaking region, in a manner that alters the force distribution around the cloaking object. Consequently, deformations remain unaltered in the surrounding region as if the cloaking object is absent. This means that an external observer would not be able to detect the presence of the cloaking object by looking at the boundary deformations or stresses. Adopted from [4].

For the mechanical cloak design, in our collaborative work [4], we followed a two-step approach to design two-dimensional mechanical cloaks. The first step involves determining the distribution of mechanical stiffness properties in the cloaking region. The second step involves finding the building blocks from a pre-computed database that possess these same mechanical properties. For the first step, we discretize the whole structure into several subdomains (building blocks). Each subdomain is classified into one of the three regions. The mechanical properties in each subdomain within the cloaking region, are determined using a computational algorithm. The algorithm known as topology optimization uses computational tools such as finite element analysis to update mechanical properties iteratively. The algorithm determines these properties while minimizing the distortion in displacements within the surrounding region with and without the cloaking object. In the second step, we look for building blocks in our large pre-computed database that match the corresponding mechanical properties at each subdomain. In the generated designs to cloak the void, the building blocks are generally stiffer in the vicinity of the void than the surrounding medium. Intuitively, to cloak a void, we need to make up for the material that is removed as if it is not participating in carrying any loads. For example, in a plate with a circular hole under tension, stresses concentrate around the hole. Hence, the material in the vicinity of the void ends up carrying more load. From our numerical as well as experimental measurements on these designs, we found excellent cloaking performance. Although the shielding is not perfect it is sufficiently effective.

C h a p t e r   2

THEORY AND METHODS

2.1   Introduction

This chapter introduces the theory of linear elasticity. We then propose a method for generating diverse unit cell geometries explored in this thesis. Then the details of the experimental setup used for testing additively manufactured specimens is discussed. Finally, the digital image correlation procedure suitable for structured materials is discussed.

2.2   Anisotropic linear elasticity

Under the small strain assumption, the constitutive law for a general anisotropic solid, which relates the Cauchy stress tensor $\boldsymbol{\sigma}$ and the infinitesimal strain tensor $\boldsymbol{\varepsilon}$, is given by the generalized Hooke's law [58, 59],

$$\boldsymbol{\sigma} = \boldsymbol{C}\boldsymbol{\varepsilon} \quad \text{or} \quad (\sigma_{ij} = C_{ijkl}\varepsilon_{kl}), \tag{2.1}$$

where $\boldsymbol{C}$ is a fourth-order tensor, known as the elasticity tensor or the stiffness tensor, and Einstein's notation for summation over repeated indices is followed. For a two-dimensional anisotropic solid, under plane strain conditions, Eq. (2.1) can be written using Voigt notation as

$$\begin{bmatrix} \sigma_{11} \\ \sigma_{22} \\ \sigma_{12} \end{bmatrix} = \begin{bmatrix} C_{1111} & C_{1122} & C_{1112} \\ C_{1122} & C_{2222} & C_{2212} \\ C_{1112} & C_{2212} & C_{1212} \end{bmatrix} \begin{bmatrix} \varepsilon_{11} \\ \varepsilon_{22} \\ 2\varepsilon_{12} \end{bmatrix}, \tag{2.2}$$

where C_{1111}, C_{1122}, C_{2222}, C_{1112}, C_{2212}, C_{1212} are the elasticity tensor parameters in a given reference frame, $\varepsilon_{11}, \varepsilon_{22}$ are the axial strains, ε_{12} is the shear strain, σ_{11}, σ_{22} are the axial stresses, and σ_{12} is the shear stress. For readability, we combine the pair of indices as follows: $()_{11} \rightarrow ()_1, ()_{22} \rightarrow ()_2, ()_{12} \rightarrow ()_6$ and write Eq. (2.2) as

$$\begin{bmatrix} \sigma_1 \\ \sigma_2 \\ \sigma_6 \end{bmatrix} = \begin{bmatrix} C_{11} & C_{12} & C_{16} \\ C_{12} & C_{22} & C_{26} \\ C_{16} & C_{26} & C_{66} \end{bmatrix} \begin{bmatrix} \varepsilon_1 \\ \varepsilon_2 \\ 2\varepsilon_6 \end{bmatrix}. \tag{2.3}$$

From thermodynamic constraints, the elasticity tensor has to be positive definite, which implies

$$C_{11} > 0, \quad C_{22} > 0, \quad C_{66} > 0, \tag{2.4a}$$

$$C_{11}C_{22} - C_{12}^2 > 0, \quad C_{11}C_{66} - C_{16}^2 > 0, \quad C_{22}C_{66} - C_{26}^2 > 0. \tag{2.4b}$$

The stiffness parameter C_{11} directly relates the axial stress σ_1 with axial strain ε_1, while C_{16} relates the axial stress σ_1 with shear strain σ_6, and so on. The off-diagonal moduli C_{16}, C_{26} are also known as shear-normal or extension-shear coupling parameters. The stiffness parameter C_{12} represents the extension-to-extension deformation coupling. Shear-normal coupling has been explored in the context of structured materials by [60, 61]. One of the objectives of this work is to determine the maximum and minimum values a single parameter can reach relative to the others, as discussed in the following section. This understanding helps us to evaluate the extent of shear-normal coupling induced by anisotropy. As a result of these anisotropy-induced couplings, the experimental identification of the material parameters becomes non-trivial because a constant state of strain is hard to achieve, even in a standard uniaxial tension test. Therefore, one of the main objectives of this thesis is to identify these six material parameters $C_{11}, C_{12}, C_{22}, C_{16}, C_{26}, C_{66}$ from least number of experimental measurements. Note that the parameters C_{16} and C_{26} will be zero if the material has symmetry planes along the x_1 and x_2 axes.

The general equilibrium equation(s) for an arbitrary anisotropic linear elastic solid is given by

$$C_{ijkl}\frac{\partial^2 u_k}{\partial x_i \partial x_l} = 0. \tag{2.5}$$

Under plane-strain conditions, the displacement is of the form $\boldsymbol{u}(x_1, x_2) = u_1(x_1, x_2)\boldsymbol{e}_1 + u_2(x_1, x_2)\boldsymbol{e}_2$, where $\boldsymbol{e}_1, \boldsymbol{e}_2$ are the unit vectors aligned with the coordinate axes. Then Eq. (2.5) changes as

$$C_{11}\frac{\partial^2 u_1}{\partial x_1^2} + C_{66}\frac{\partial^2 u_1}{\partial x_2^2} + 2C_{16}\frac{\partial^2 u_1}{\partial x_1 \partial x_2} + C_{16}\frac{\partial^2 u_2}{\partial x_1^2} + C_{26}\frac{\partial^2 u_2}{\partial x_2^2} + (C_{12} + C_{66})\frac{\partial^2 u_2}{\partial x_1 \partial x_2} = 0, \tag{2.6a}$$

$$C_{16}\frac{\partial^2 u_1}{\partial x_1^2} + C_{26}\frac{\partial^2 u_1}{\partial x_2^2} + (C_{12} + C_{66})\frac{\partial^2 u_1}{\partial x_1 \partial x_2} + C_{66}\frac{\partial^2 u_2}{\partial x_1^2} + C_{22}\frac{\partial^2 u_2}{\partial x_2^2} + 2C_{26}\frac{\partial^2 u_2}{\partial x_1 \partial x_2} = 0. \tag{2.6b}$$

Thus multiple parameters directly affect the deformation of the solid.

Symmetries of the elasticity tensor

The existence of shear-normal coupling and the maximum number of independent stiffness tensor parameters depend on the symmetries associated with the material microscopic topology [59, 62]. In plane elasticity, stiffness tensors are categorized into four symmetry classes. They are denoted as $O(2)$ for Isotropic, D_4 for Tetragonal, D_2 for Orthotropic, and Z_2 for Digonal (fully anisotropic) with 2, 3, 4, and 6 independent parameters, respectively. This categorization is based on the invariants of the stiffness tensor [63, 64].

Eigen values are another important parameters of the elasticity tensors [23]. They show that it is possible to decompose elasticity using its eigen values and basis matrices, as shown in Eq. (2.7), with each basis representing a mode of deformation:
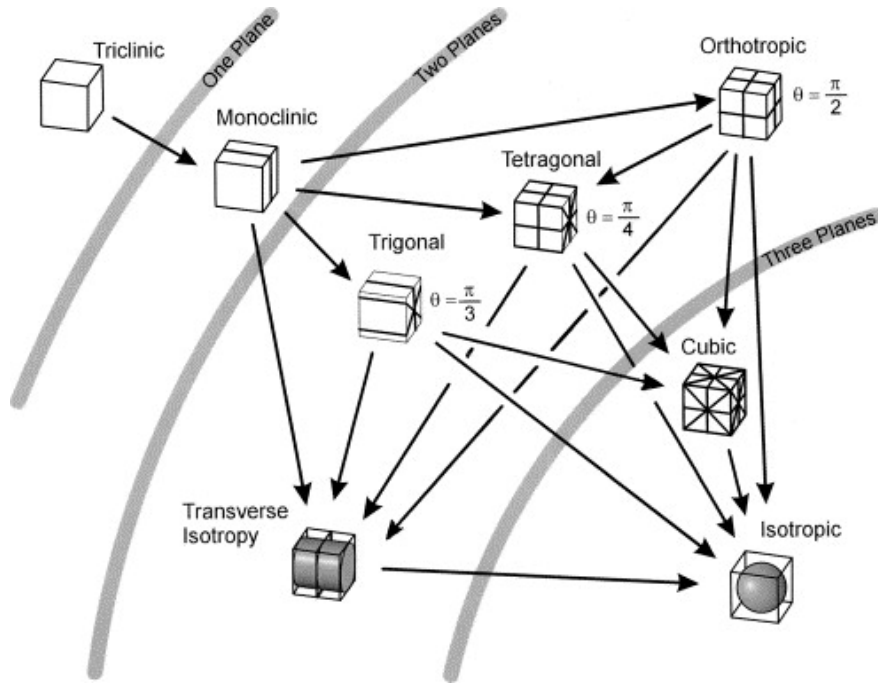
Figure 2.1: Anisotropic materials can be classified into 8 different classes based on the number of mirror plane of symmetries present within the geometry. Adopted from [5].

$$C_{ijkl} = \sum_{a=1}^{6} \lambda_a v_{ij}^{(a)} v_{kl}^{(a)} \quad \text{in which} \quad \sum_{i,j=1}^{6} v_{ij}^{(a)} v_{ij}^{(a)} = 1, \quad \lambda_a > 0. \tag{2.7}$$

Coordinate transformation of the elasticity tensor

Let us assume that the unit cell is rotated by an angle θ counter-clockwise. According to Sadd [65], the components of the elasticity tensor (C'_{pqrs}) in the original coordinate system after the rotation of the unit cell is related to the components of the elasticity tensor (C_{ijkl}) as,

$$C'_{pqrs} = C_{ijkl} Q_{pi} Q_{qj} Q_{rk} Q_{sl}, \tag{2.8}$$

where Q is the transformation matrix given by,

$$Q = \begin{bmatrix} \cos\theta & -\sin\theta & 0 \\ \sin\theta & \cos\theta & 0 \\ 0 & 0 & 1 \end{bmatrix}. \tag{2.9}$$

Expanding Eq. (2.8) for each individual stiffness tensor component we get,

$$C'_{11} = C_{11} \cos^4 \theta - 4C_{16} \cos^3 \theta \sin \theta + 2(C_{12} + 2C_{66}) \cos^2 \theta \sin^2 \theta$$
$$- 4C_{26} \cos \theta \sin^3 \theta + C_{22} \sin^4 \theta \tag{2.10a}$$

$$C'_{12} = C_{12} \cos^4 \theta + 2(C_{16} - C_{26}) \cos^3 \theta \sin \theta + (C_{11} + C_{22} - 4C_{66}) \cos^2 \theta \sin \theta^2$$
$$+ 2(-C_{16} + C_{26}) \cos \theta \sin^3 \theta + C_{12} \sin^4 \theta \tag{2.10b}$$

$$C'_{22} = C_{22} \cos^4 \theta + 4C_{26} \cos^3 \theta \sin \theta + 2(C_{12} + 2C_{66}) \cos^2 \theta \sin^2 \theta$$
$$+ 4C_{16} \cos \theta \sin^3 \theta + C_{11} \sin^4 \theta \tag{2.10c}$$

$$C'_{16} = C_{16} \cos^4 \theta + (C_{11} - C_{12} - 2C_{66}) \cos^3 \theta \sin \theta + 3(-C_{16} + C_{26}) \cos^2 \theta \sin^2 \theta$$
$$+ (C_{12} - C_{22} + 2C_{66}) \cos \theta \sin^3 \theta - C_{26} \sin^4 \theta \tag{2.10d}$$

$$C'_{26} = C_{26} \cos^4 \theta + (C_{12} - C_{22} + 2C_{66}) \cos^3 \theta \sin \theta + 3(C_{16} - C_{26}) \cos^2 \theta \sin^2 \theta$$
$$+ (C_{11} - C_{12} - 2C_{66}) \cos \theta \sin^3 \theta - C_{16} \sin^4 \theta \tag{2.10e}$$

$$C'_{66} = C_{66} \cos^4 \theta + 2(C_{16} - C_{26}) \cos^3 \theta \sin \theta + (C_{11} - 2C_{12} + C_{22} - 2C_{66}) \cos^2 \theta \sin^2 \theta$$
$$+ 2(-C_{16} + C_{26}) \cos \theta \sin^3 \theta + C_{66} \sin^4 \theta. \tag{2.10f}$$

Invariants of the elasticity tensor

Using harmonic decomposition [63], the strain energy density (W) can be decomposed as,

$$2W = \sigma^s_{ij} \varepsilon^s_{ij} + \sigma^d_{ij} \varepsilon^d_{ij}, \tag{2.11a}$$
$$= D_{ijkl} \varepsilon^d_{ij} \varepsilon^d_{kl} + 2\mu \varepsilon^d_{pq} \varepsilon^d_{pq} + a_{pq} \varepsilon^d_{pq} \varepsilon_{rr} + \kappa \varepsilon_{pp} \varepsilon_{qq}, \tag{2.11b}$$

where σ^s_{ij}, σ^d_{ij}, ε^s_{ij}, ε^d_{ij} are the spherical and deviatoric part of the stress and strain tensors respectively. Here Einstein's notation of summation over repeated indices is used. σ^s_{ij}, σ^d_{ij} are defined as

$$\sigma^s_{ij} = \left(\frac{1}{2} a_{pq} \varepsilon^d_{pq} + k \varepsilon_{pp} \right) \delta_{ij}, \tag{2.12a}$$

$$\sigma^d_{ij} = D_{ijkl} \varepsilon^d_{kl} + 2\mu \varepsilon_{ij} + \frac{1}{2} \varepsilon_{pp} a_{ij}, \tag{2.12b}$$

where D_{ijkl}, a_{ij}, λ, μ are the parameters obtained from harmonic decomposition of the elasticity tensor as

$$C_{ijkl} = D_{ijkl} + \frac{1}{6} \left(\delta_{ij} a_{kl} + \delta_{kl} a_{ij} + \delta_{ik} a_{jl} + \delta_{jl} a_{ik} + \delta_{il} a_{jk} + \delta_{jk} a_{il} \right) + \lambda \delta_{ij} \delta_{kl} + \mu \left(\delta_{ik} \delta_{jl} + \delta_{il} \delta_{jk} \right),$$
$$\tag{2.13}$$

where D_{ijkl}, a_{ij}, λ, μ are all linear combinations of the elasticity tensor parameters.

λ is defined as

$$\lambda = \frac{1}{8} \left(3C_{ppqq} - 2C_{pqpq} \right) \quad \text{with} \quad p, q \in [1, 2],$$
$$= \frac{1}{8} \left(3 \left(C_{1111} + C_{1122} + C_{2211} + C_{2222} \right) - 2 \left(C_{1111} + C_{1212} + C_{2121} + C_{2222} \right) \right),$$
$$= \frac{1}{8} \left(C_{11} + C_{22} + 6C_{12} - 4C_{66} \right). \tag{2.14}$$

μ is defined as

$$\mu = \frac{1}{8} \left(2C_{pqpq} - C_{ppqq} \right),$$
$$= \frac{1}{8} \left(2 \left(C_{1111} + C_{1212} + C_{2121} + C_{2222} \right) - \left(C_{1111} + C_{1122} + C_{2211} + C_{2222} \right) \right),$$
$$= \frac{1}{8} \left(C_{11} + C_{22} + 4C_{66} - 2C_{12} \right). \tag{2.15}$$

a_{ij} is defined as

$$a_{ij} = \frac{1}{12} \left(2C_{ipjp} - C_{pqpq}\delta_{ij} \right),$$
$$a_{11} = - a_{22} = \frac{1}{12} \left(2 \left(C_{1111} + C_{1212} \right) - \left(C_{1111} + C_{1212} + C_{2121} + C_{2222} \right) \right) = \frac{1}{12} \left(C_{11} - C_{22} \right),$$
$$a_{12} = a_{21} = \frac{1}{12} \left(2 \left(C_{1121} + C_{1222} \right) \right) = \frac{1}{12} \left(2 \left(C_{16} + C_{26} \right) \right) = \frac{1}{6} \left(C_{16} + C_{26} \right). \tag{2.16}$$

D_{ijkl} is defined as

$$D_{1111} = \frac{1}{8} \left(C_{11} + C_{22} - 2C_{12} - 4C_{66} \right),$$
$$D_{1112} = \frac{1}{2} \left(C_{16} - C_{26} \right),$$
$$D_{1111} = - D_{2211} = -D_{1221} = -D_{2121} = -D_{1212} = -D_{2112} = -D_{1122} = D_{2222}, \tag{2.17}$$
$$D_{1211} = D_{2111} = D_{1121} = -D_{2221} = D_{1112} = -D_{2212} = -D_{1222} = -D_{2122}. \tag{2.18}$$

Based on this decomposition, four invariants, that do not depend on the choice of the coordinate system of the material, I_1, J_1, I_2, J_2 are defined as follows.

I_1 is a measure of the sphericity of the material and is defined as

$$I_1 = \kappa = \lambda + \mu,$$
$$= \frac{1}{4} \left(C_{11} + C_{22} + 2C_{12} \right). \tag{2.19}$$

J_1 is a measure of the isotropic part of the deviatoricity of the material and is defined as

$$J_1 = \mu = \frac{1}{8}\left(C_{11} + C_{22} + 4C_{66} - 2C_{12}\right). \tag{2.20}$$

I_2 is the square of a norm that measures the amount of coupling energy in the material and is defined as

$$
\begin{aligned}
I_2 &= \sqrt{a_{ij}a_{ij}}, \\
&= \sqrt{2(a_{11}^2 + a_{12}^2)}, \\
&= \frac{1}{6\sqrt{2}}\sqrt{(C_{11} - C_{22})^2 + 4(C_{16} + C_{26})^2}.
\end{aligned}
\tag{2.21}
$$

J_2 measures the squared norm of the anisotropic part of the deviatoricity of the material and is defined as

$$
\begin{aligned}
J_2 &= \sqrt{D_{ijkl}D_{ijkl}}, \\
&= \frac{1}{2\sqrt{2}}\sqrt{(C_{11} + C_{22} - 2C_{12} - 4C_{66})^2 + 16(C_{16} - C_{26})^2}.
\end{aligned}
\tag{2.22}
$$

In the case of isotropic material, the invariants I_2, J_2 would be zero. Also note that, the shear-normal coupling parameters are not involved in I_1, J_1. Several observations on the trends in the property plots described in Section 3.4 can be understood from the invariant perspective.

Homogenization

Each unit cell's effective material properties are then computed using a numerical homogenization scheme [66, 67]. The homogenization scheme is based on length scale separation and follows a two-scale asymptotic expansion of stress equilibrium equation. The resulting effective properties are equivalent in the average energy stored in the unit cell for all possible loading conditions. In computing the effective properties, we fix the pixel resolution at 100. For the gray phase, we use a stiffer material DM8530 ($E = 1$ GPa, $\nu = 0.3$) and for black phase, we use a softer material Tango Black ($E = 0.7$ MPa, $\nu = 0.49$), representative of materials from commercial multi-material Connex 3D printer. The material properties are experimentally determined following the ASTM D638-14 standard test method. It should be noted that in the limit, the Young's modulus of the soft phase goes to zero, does not completely describe a hole or a void. In the case of void, both bulk and shear moduli are zero. However for a really soft phase, the bulk modulus does not go to zero. For computational purposes, we limit our study to the case of two phases with contrasting moduli, but not a stiff-phase with voids.

2.3 Unit cell database generation

To design unit cells, we use a pixelated representation for the unit cell geometry parametrization. Exploring all possible combinations of two phases in this pixelated representation is computationally NP-hard[1]. Therefore, to sample periodic diverse anisotropic unit cells efficiently with lower degrees of symmetry, we follow an approach inspired by Cahn's method of generating Gaussian random fields [52, 68, 69]. Additionally, this method is inspired by the observation that the power spectral density of microstructures in metallic systems tends to be sparse and has peaks highly concentrated at lower spatial frequencies, [70, 71], explained in detail in Fig. 2.4. We first define a periodic function $f(x_1, x_2)$, as a linear combination of cosine functions:

$$f(x_1, x_2) = \sum_{m,n} A_{mn} \cos\left(2\pi(mx_1 + nx_2)\right), \quad \forall(x_1, x_2) \in [-0.5, 0.5], \quad \forall m, n \in \mathbb{Z}, \qquad (2.23)$$

where m, n are spatial frequencies, and A_{mn} are the corresponding cosine function weights. The function is then thresholded at a value ξ, to generate a binary image which represents a unit cell, as shown in Fig. 2.2A-B.

a) Periodic function   b) Unit cell   c) Metamaterial
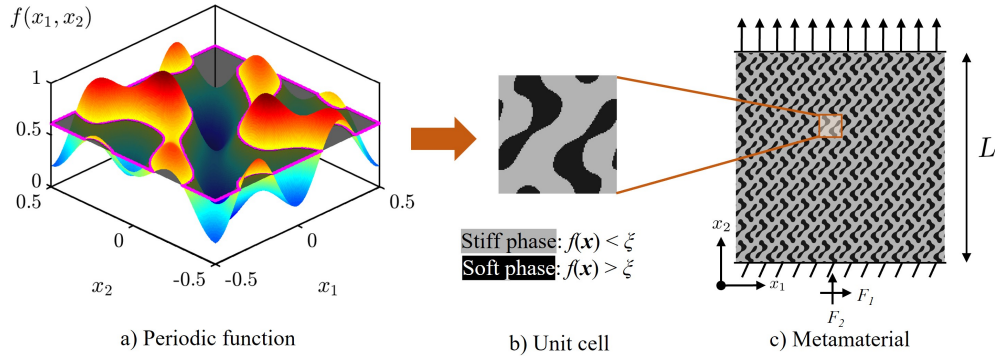
Figure 2.2: Design of an anisotropic unit cell geometry by thresholding a periodic function. (A) An example periodic function $f(x_1, x_2)$. (B) A two-phase unit cell geometry consisting of a stiffer (gray) and a softer phase (black). (C) A two-dimensional anisotropic metamaterial created by tessellating the unit cell geometry (shown in the inset) ten times along both x_1- and x_2- axes.

There are several notable observations for this approach. Firstly, the periodicity in the unit cells is ensured by directly selecting cosine functions. Interestingly, choosing between sine and cosine as the fundamental periodic function does not affect the distribution of the resulting properties. By controlling the symmetries in the weights, we can control the symmetries in the unit cell. For instance, if $A_{mn} = A_{nm}$, the result is diagonally symmetric unit cells. Adjusting the pixel density allows us to generate unit cells with arbitrary resolutions as need-based.

---

[1]For example, a 100×100 periodic pixelated representation requires the computation of mechanical properties of $2^{99 \times 99} = 2^{9801}$ unit cells.

By increasing the threshold value of the function Eq. (2.23), the fill fraction of the stiff phase increases monotonically. Each function exhibits a different rate of monotonic increase in the fill fraction, as illustrated in the top inset of Fig. 2.3B. The number of spatial modes is a hyperparameter $2\zeta+1$, with $\zeta = \max(m, n)$. In Fig. 2.3C, the variation of typical feature sizes is shown when the number of spatial modes is varied. Increasing the number of spatial modes leads to smaller feature sizes and increased randomness, resulting in unit cells that tend to be less anisotropic. The shape of the unit cell is also an important factor for achieving anisotropic properties and is a design choice that is often overlooked. By modifying the directions of periodicity in the proposed periodic function definition Eq. (2.23), we can also generate non-square unit cells as shown in Fig. 2.3D.

In a 2D periodic system, the unit cells can be rectangular, square, parallelogram-shaped, or irregularly hexagonal. Using the concepts of Bravais lattices and Brillouin zone, it is sufficient to consider an arbitrary parallelogram-shaped unit cell defined by the side lengths a, b and the angle between the edges $90° − \theta$, to describe all possible unit cell shapes completely [62]. The values for parallelogram $a = 1, b = 1, \theta = 30°$ would give an equivalent regular hexagonal unit cell. Therefore, to generate non-square unit cell data, we considered several non-square oblique unit cells when the angle parameter is varied such that $−45° < \theta < 45°$, while the ratio of side length is varied such that $0.3 \leq \frac{a}{b} \leq 3$.

Overall, this method allows us to systematically explore a large property space and identify structures that exhibit the desired anisotropic elasticity tensors and suitable for estimating theoretical bounds on the anisotropic moduli, as discussed in Section 4.5. This approach also enables interpolation between different unit cell shapes, leading to the generation of functionally graded structures, as discussed further in Section 5.2.

We further provide a justification on the selection of the cosines functions as basis functions for unit cell generation. Two unit cells are included for this discussion, the first one is an arbitrary one with no distinctive patterns and almost noisy. Second one is a unit cell obtained from the method described in Section 2.3. The Fourier spectrum of both the unit cells is obtained after Gaussian filtering and is shown in Fig. 2.4. Note that the zero-frequency component, which represents the image's mean value and has the highest magnitude, is removed from the plots to better illustrate the distribution of the other frequencies. For the almost noisy unit cell, the (real) spectrum consisted of peaks from a wide range of spatial frequencies. For the second unit cell, the spectrum is concentrated at the lower spatial frequencies. Therefore we chose the described representation to generate unit cells studied in this paper.
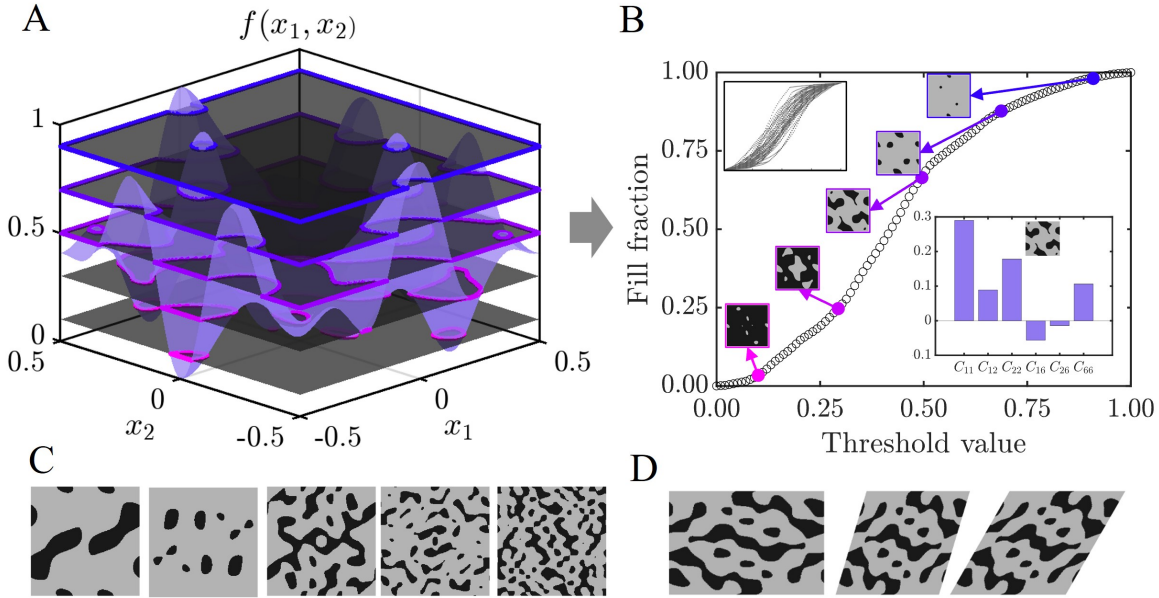
Figure 2.3: Various anisotropic unit cells can be sampled by thresholding periodic functions composed of several cosine spatial modes. (A) An example periodic function, (B) Variation of unit cell patterns with the fill fraction of stiff phase as the threshold value is changed from 0 to 1 for a particular periodic function, elastic properties of a unit cell normalized with the Young's modulus of the stiff phase (bottom-inset), variation of the threshold–fill fraction curve for different realizations of the periodic function (top-inset). (C) As the number of spatial modes is increased, finer patterns arise in the designs and unit cells tend to be less anisotropic, (D) To generate non-square unit cells, the directions along which the function is periodic can be varied. Rectangular, parallelepiped, and oblique shaped unit cells are shown for a fixed unit cell pattern.

2.4 Experimental data acquisition

Fabrication: We fabricate the specimens using a commercial multi-material polyjet technology-based 3D printer, the Stratasys Objet500 Connex. The specimens measure $75 \times 75 \times 5$ mm, not including the portion inserted into the grips. For the stiff phase, we use Stratasys' proprietary material DM8530, and for the soft phase, TangoBlack. The specimen fabrication is detailed in Fig. 2.5. The material properties are experimentally determined following the ASTM D638-14 standard test method: DM8530 has a Young's modulus (E) of 1000 ± 90 MPa and a Poisson's ratio (v) of 0.35, while TangoBlack has a Young's modulus (E) of 0.7 MPa and a Poisson's ratio (v) of 0.49 (See Fig. 2.6).

Tension testing: We subject the additively manufactured specimens to displacement-controlled tension tests using a universal testing machine, Instron E3000 (as shown in Fig. 2.7 and Fig. 2.8). We apply a vertical displacement of 1.5 mm at the top boundary at a rate of 0.5 mm/min resulting in a global axial strain of $\tilde{\varepsilon}_{22} = 0.02$ and a global strain rate of 1.1×10^{-4} s^{-1}. We use the same strain
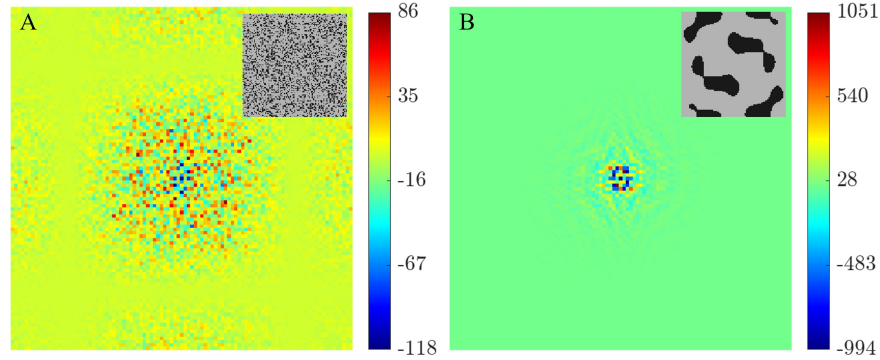
Figure 2.4: Fourier spectrum comparison of two different type of unit cells. A) Inset shows a unit cell obtained as a random binary image with its corresponding real part of the Fourier spectrum. B) Inset shows a unit cell obtained from the method described in Section 2.3 with it's corresponding real part of the fourier spectrum. Both the unit cells are chosen such that they have same fill fraction of the stiff phase.

rate while measuring the constitutive material properties of the individual phases. We repeated the experiments on three different specimens for the same design. All the specimens showed little variation in the observed global behavior.

Custom-designed aluminum grips, serrated to firmly hold specimens and prevent lateral slipping, were fabricated. The effect of slip at the grips was further investigated using various surface roughness conditions, as discussed in Fig. 2.9. Initially, the grips had a smooth surface finish. The tolerances in the screws holding the sample were close to 0.5 mm (4.5 mm holes with M4 screws). Due to these tolerances and the smooth surface finish, the anisotropic specimen slipped laterally, leading to discrepancies between experiments and simulations in the observed load and full-field displacement data. Several combinations of surface roughness on the specimen were tested, including roughening the specimen that goes into the grips and reducing the hole diameter. Despite using 4 mm holes, the specimen still slipped. The 3D printed material, being softer than the screws, allowed the screws to enlarge the holes upon loading. Metal inserts were then used in the holes, pushed into the specimen with a hot solder gun. The difference in results between (A) and (C) was minimal when using the serrated grips shown in (E). Finally, 100 grit sandpaper was glued onto the sample, but this method provided the least successful results as the sandpaper contributed to machine compliance and eventually leading to a decrease in the observed loads.

Image acquisition: We use DIC, an image-based optical technique, to measure the full-field displacements [72, 73]. We capture images at a frequency of 1 Hz using a Nikon D750 camera equipped with a Nikon AF-S NIKKOR 24-120mm f/4G ED VR zoom lens. We use manual mode at an exposure rate of 1/640 sec, an ISO setting of 1250, and an aperture setting of F8. We use
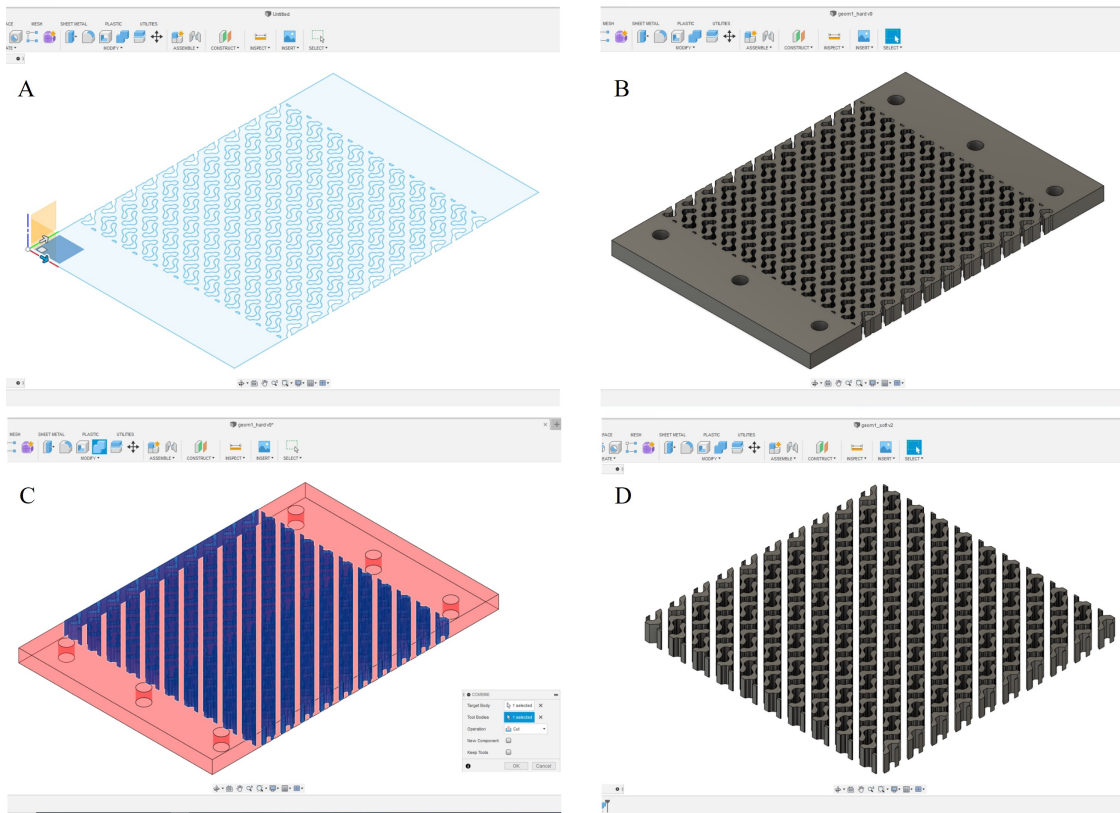
Figure 2.5: Anisotropic metamaterial sample design and fabrication for digital-image correlation (DIC) experiments. The first step involves converting a drawing into STLs for stiff and soft phases separately. The sequence of steps are as follows. (A) Import drawing as 'mm' scale. (B) Extrude 3D model of hard part. (C) Boolean operation ('Cut' in Fusion). (D) 3D model of soft part. Then the two STLs are used in conjunction in Stratasys Object 500 printer's software to fabricate the specimen as shown Fig. 2.7. (Credit: Jihoon Ahn)

the *global DIC* approach, and perform DIC using piece-wise linear shape functions defined on a triangular mesh with an edge length of ≈ 0.35 mm, to compute the displacements (as in Agnelli et al. [47]).

Simulations: We use synthetic data generated using the FEM to verify our methods and aid our analysis before performing the experiments.
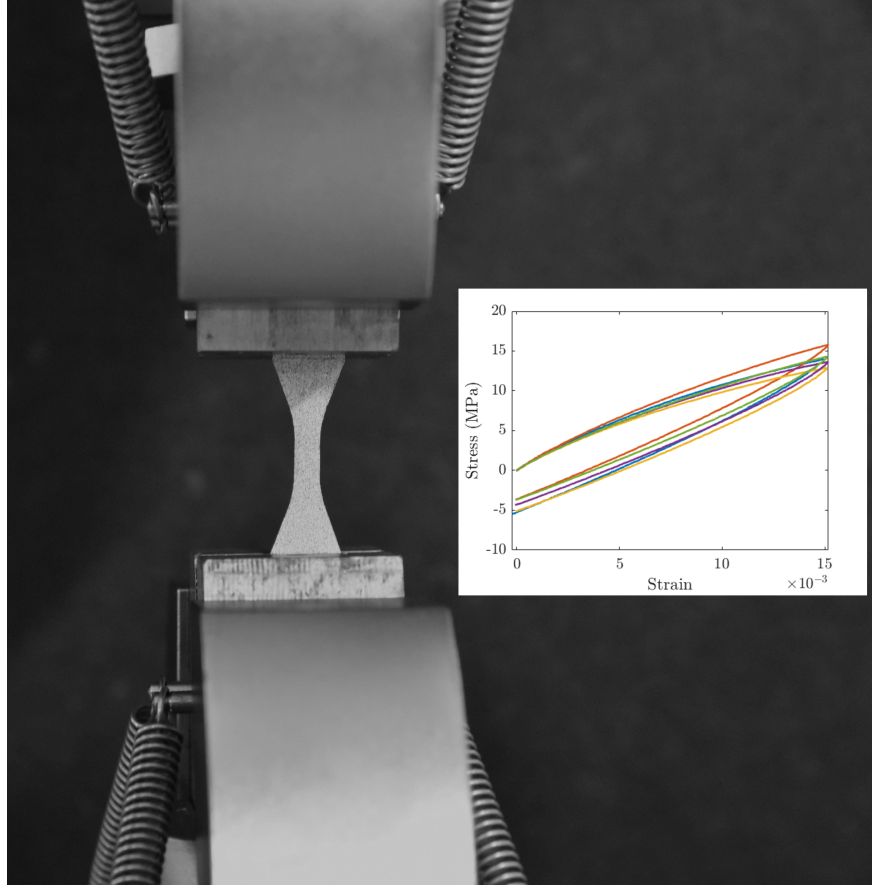
Figure 2.6: ASTM D638-14 type V specimen used for the evaluation of the material properties of the constitutive materials. The Poisson's ratio is measured from the average lateral and axial strains, evaluated in the non-varying region of the cross-section of the specimen. The stress-strain data obtained load-displacement data is used to infer Young's Modulus. The hysteresis in the data after unloading is ignored and only the loading part slope is used to estimate the Young's modulus. Each color refers to different samples tested.

2.5   Digital image correlation

Given a reference image f and and a deformed image g, the correlation algorithm aims at minimizing the sum of squared differences over the considered domain Ω

$$\mathcal{T} = \int_{\Omega} \left(g(\boldsymbol{x} + \boldsymbol{u}(\boldsymbol{x})) - f(\boldsymbol{x})\right)^2 d\boldsymbol{x}, \tag{2.24}$$

where $\boldsymbol{x}$ is the position in the reference image and $\boldsymbol{u}(\boldsymbol{x})$ is the displacement field which is interpolated as

$$\boldsymbol{u}(\boldsymbol{x}) = \sum u_n \boldsymbol{\phi}_n(\boldsymbol{x}), \tag{2.25}$$

where $\boldsymbol{\phi}_n$ are a set of shape functions and u_n the associated degrees of freedom. There are two approaches to determine the unknowns u_n, *local DIC* and *global DIC* [73]. In the *local* approach,

the region of interest (Ω) is divided into several sub-images known as subsets and the mean displacement of each subset is computed independently while minimizing the objective Eq. (2.24).
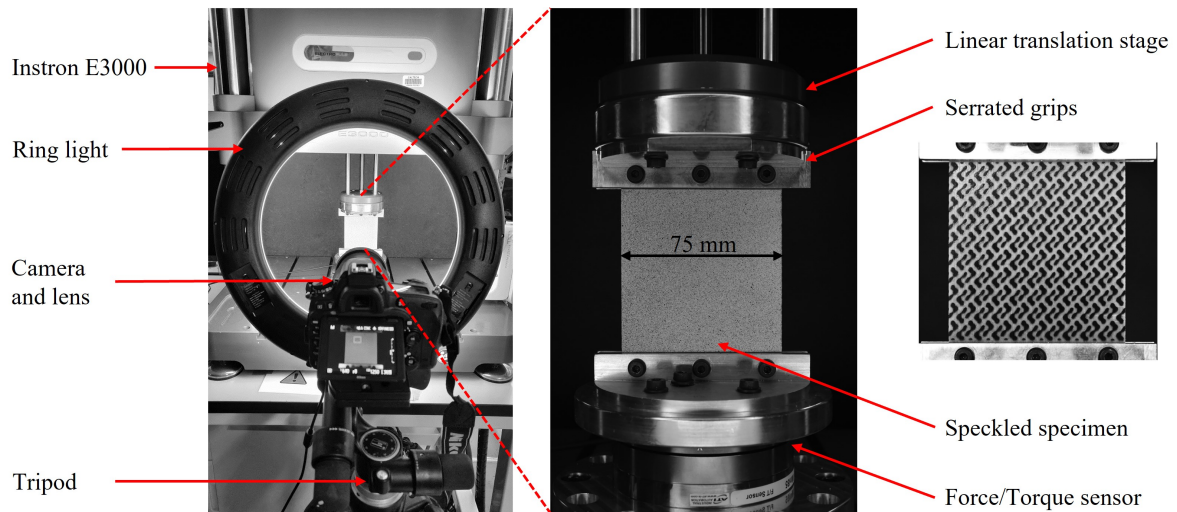
Figure 2.7: Experimental setup for displacement-controlled uniaxial testing of an anisotropic metamaterial.
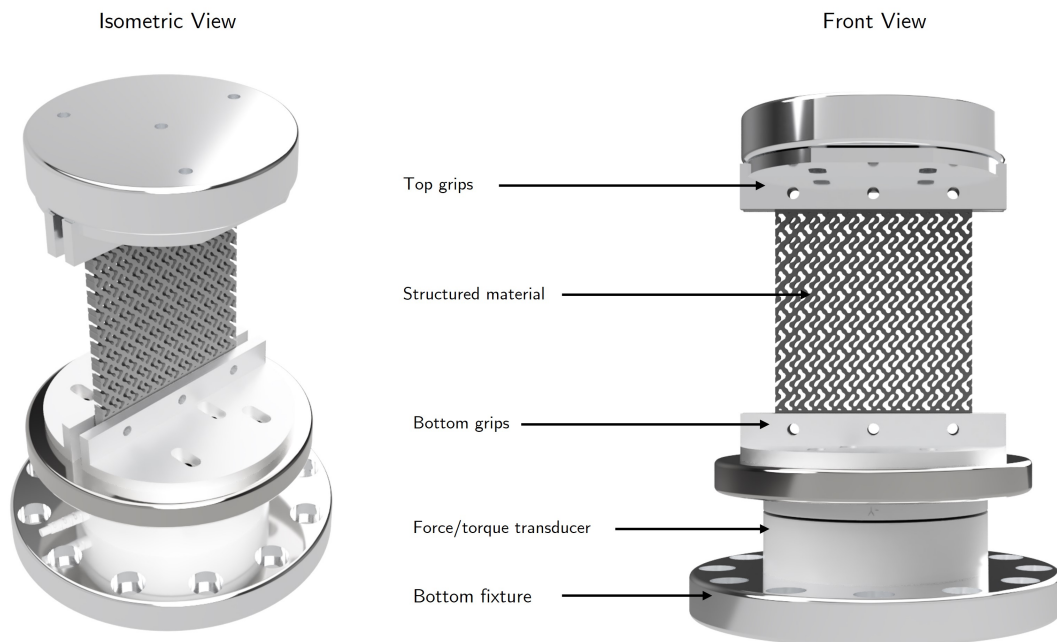
Figure 2.8: Digital rendering of the designed experimental setup. The grips move laterally in-plane using the straight guided slots. This setup allows for clamping specimens of varied thicknesses.
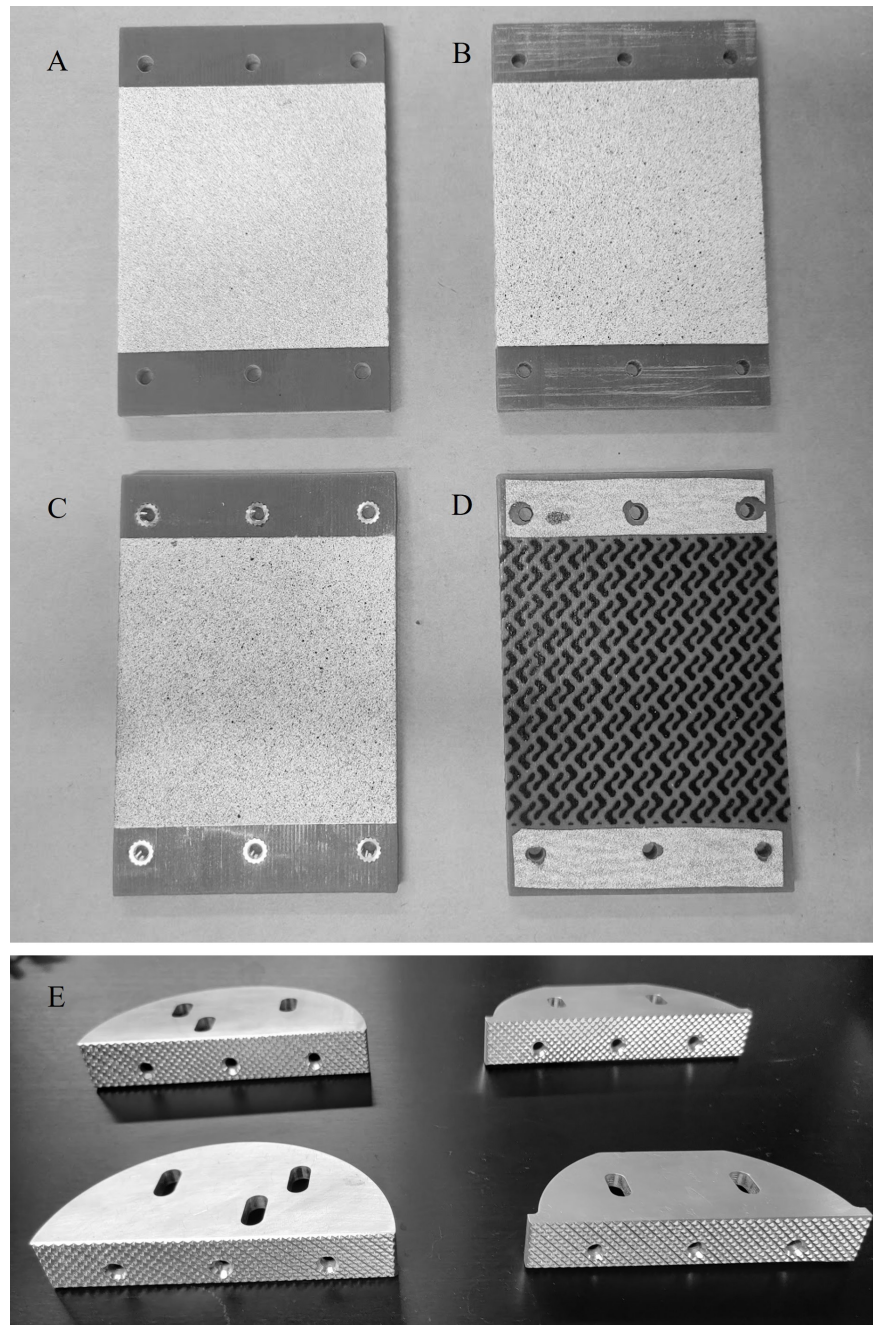
Figure 2.9: To ensure accurate measurement of both shear and axial forces, it is crucial that there is no slip at the grips. The impact of grip slip in the custom-designed setup shown in Fig. 2.7 is investigated using various designs. (A) Original specimen with 4.5 mm hole diameter, (B) Specimen with 4 mm holes with gripping region roughened using a sand paper, (C) Specimen with 4 mm hole with metal inserts, (D) Specimen with 4 mm hole with a sand paper attached to the gripping region. (E) Serrated grips provided consistent and the best results.

In the *global* approach, shape functions defined through a finite element mesh over the whole region of interest are used [74]. The *global* approach assumes continuity of displacements over the entire region of interest which is well suited when the structure is heterogeneous. Moreover, the *global* approach provides the displacement information at the boundaries, which is hard to obtain using the *local* approach. The displacement data at the boundaries are an important input for the full-field measurement based parameter identification techniques. Hence, we follow the *global* approach to perform the correlation in this thesis.

We perform DIC using piece-wise linear shape functions defined on a triangular mesh to compute the displacements (as in Agnelli et al. [47]). We choose an edge length of 18 pixels (~ 0.44 mm) to construct the triangular mesh. We observe a noise floor of the order of 0.04 mm in the displacement data which is obtained from correlation performed on static images. In the future, experimental errors may be further reduced using the global DIC technique with quadratic interpolation [75]. The data provided by the DIC correspond to the nodes that might not always align with the unit cell corners. To obtain the displacements of the unit cell corners, we further average the displacement data from the nodes that fall within a 1 mm radius of a unit cell corner. The whole process is detailed in Fig. 2.10, Fig. 2.11, and Fig. 2.12. The signed distance function is especially useful when trying to construct mesh in the ROI when there are a lot of holes. This is a problem that traditional subset-based *local* approaches find hard to perform DIC. In this case, the grayscale intensity at the interface can be hard to distinguish if it is a boundary or a hole, and special care must be taken.

It is important to note that embedding constitutive materials with contrasting moduli in a planar metamaterial plate (as shown in Fig. 2.7) does not restrict deformations to being strictly planar. We visually observed that the soft phase exhibits a non-zero out-of-plane deformation, which introduces some noise in the DIC measurements. However, for our method discussed in Chapter 4, we ensured that the unit cell corners, where displacements are extracted for parameter identification, are occupied by a strict phase.
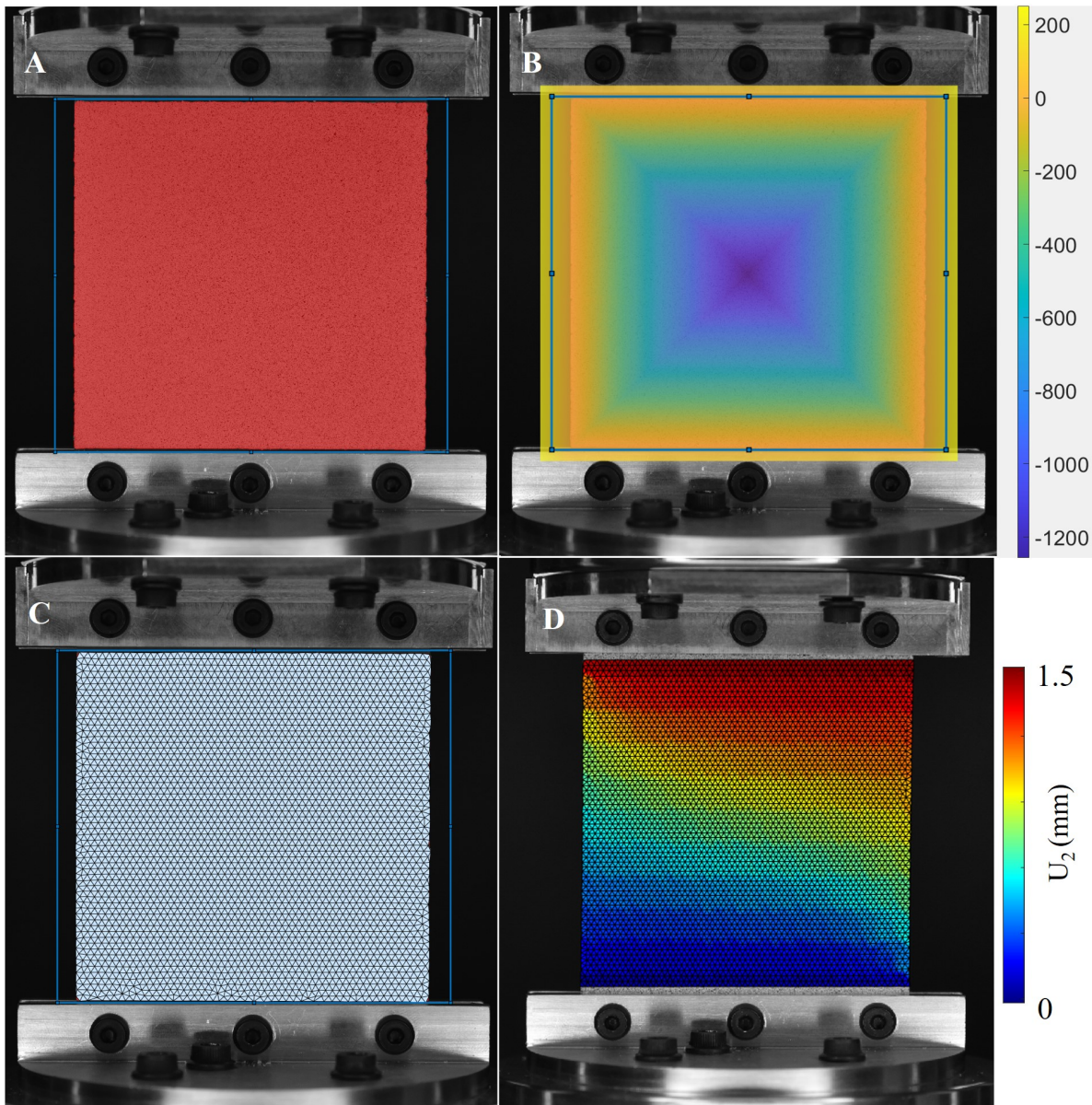
Figure 2.10: Sequence of steps while performing DIC using *global* approach. (A) The region of interest is defined selected as those pixels with a certain gray scale intensity within the selected region of interest. (B) A signed distance function is constructed in MATLAB which extends beyond the region of interest. The value of the function is positive outside the ROI. (C) Triangular mesh constructed using `distmesh` function in MATLAB. The mesh density or side length is a hyperparameter, which is chosen to be about 18 pixels. (D) Computed displacements (U_2) at the nodes of the mesh are linearly interpolated to get the full-field displacement field.
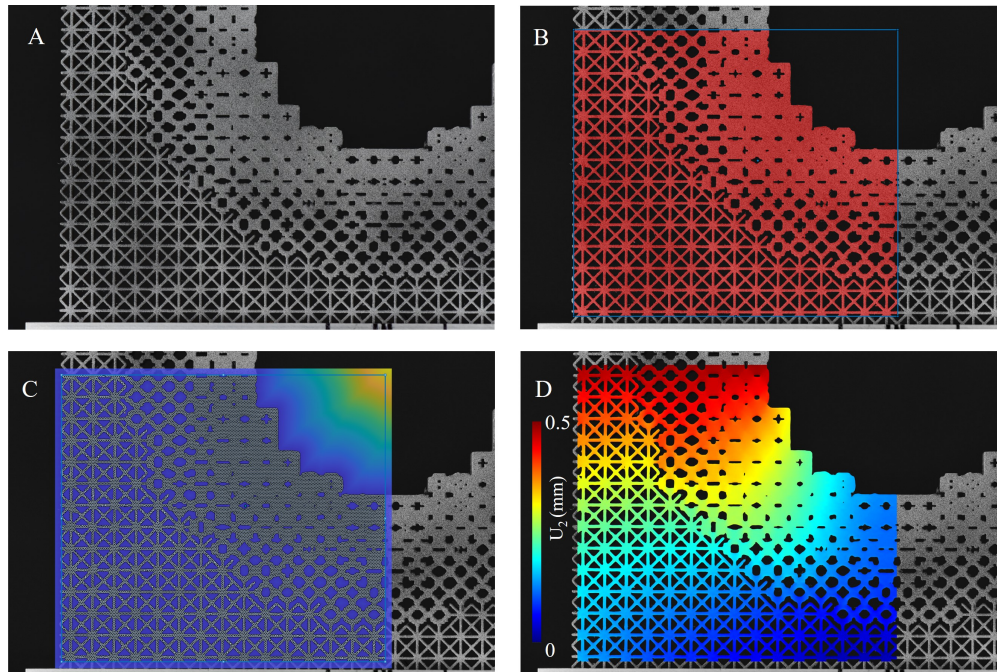
Figure 2.11: Sequence of steps while performing DIC using *global* approach in a structure with a lot of holes. (A) The speckled specimen under consideration for DIC is acquired using a Nikon D750 Camera equipped with a Nikkor 200 mm f/4D IF-ED lens. Such a setup prevents out-of-plane walls from being captured in the image. (B) The region of interest is defined selected as those pixels with a certain gray scale intensity within the selected region of interest. (C) Triangular mesh constructed using `distmesh` function in MATLAB with the help of signed distance function that distinguishes boundaries clearly. The mesh density or side length is a hyperparameter, which is chosen to be about 18 pixels. (D) Computed displacements (U_2) at the nodes of the mesh are linearly interpolated to get the full-field displacement field.
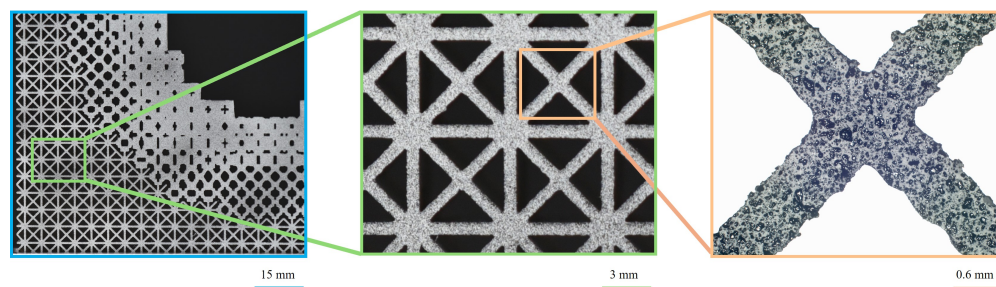
Figure 2.12: The 3D-printed structures were spray-painted white using regular off-the-shelf white paint and dried for about 30 minutes. For DIC, speckles should be finer than the features. In order to achieve finer black speckles, an airbrush was used. Airbrush was kept at a distance of about 3 cm from the surface of printed structures and sprayed at an angle of about 45° until sufficient speckle density is obtained.

Chapter 3

ESTIMATING THE BOUNDS ON ANISOTROPIC ELASTIC MODULI IN TWO-DIMENSIONAL STRUCTURED MATERIALS

Jagannadh Boddapati and Chiara Daraio. Planar structured materials with extreme elastic anisotropy. *Under Review*, July 2024.

3.1 Introduction

Designing metamaterials for anisotropy, despite their ability to attain unique properties, is a challenging task. Besides the fact that fewer or no symmetries in the unit cell design lead to a higher degree of anisotropic properties, the factors that contribute to strong anisotropic behavior with coupled deformations remain largely unexplored. Inverse techniques, such as topology optimization, are frequently used to obtain unit cells that possess desirable elasticity tensor [76, 77]. However, such inverse design techniques may not always be the best approach, as it is not known a priori whether the prescribed elasticity tensor is compatible with the provided geometric parameterization. An alternative design approach involves predefined parameterization for the unit cell. This parameterization is then used to compute pre-computed databases, enabling the derivation of useful structure-property relationships [78–83]. These data-driven methods generate databases that function as quick reference tables, such as for identifying extremal structures at the boundary of the property space, and can serve as initial guesses for topology optimization [84]. They also provide robust datasets for machine learning-based design algorithms [85, 86]. For example, using the latent space provided by variational autoencoders (VAEs), Wang et al. [87] demonstrated how to obtain complex topological and mechanical interpolations in various unit cells. Similarly, Mao et al. [88] used generative adversarial networks (GANs) to discover new unit cells beyond the training data. By leveraging the gradients provided by artificial neural network models, it is now possible to perform inverse designs customized to specific anisotropic elasticity tensors [27, 52, 89] and further to tailor nonlinear mechanical behavior [90–92]. While these unique approaches can identify unit cells with diverse elasticity tensors beyond the isotropic class, the range of achievable properties is primarily constrained by the selected input design representation. Additionally, most of these approaches are restricted to orthotropic elasticity, where coupled deformations are absent. There is limited knowledge about the range of elasticity tensors, especially concerning the extent to which shear-normal deformations can be coupled in two-dimensional single-scale structured materials.

On one hand, achieving a complete characterization of the parameter space in terms of the moduli becomes exceedingly difficult in the absence of a unique parametrization of the input geometry.

On the other hand, defining how close the obtained designs are to the theoretical bounds is also challenging, as little is known about the theoretical limits of anisotropic elastic moduli (no known closed-form expressions) [41]. This range of all possible effective tensors is mathematically known as *G-closure*. In classical studies on isotropic composites, [93, 94] present a variational approach to determine the upper and lower bounds on the effective bulk and shear moduli (κ^* and μ^*) by decomposing the elastic energy into hydrostatic and deviatoric parts. Hence, the bulk and shear moduli directly represent the energy that can be stored in the composites under hydrostatic and deviatoric loading respectively. However, individual parameters in the fully anisotropic case do not hold such straightforward interpretations. Even in the isotropic case, there are areas in the property space of μ^* defined by theoretical bounds where composites are yet to be discovered [41]. Willis [95], Milton and Kohn [96], Cherkaev and Gibiansky [97], Allaire and Kohn [98] extended the theory of Hashin-Shtrikman bounds to orthotropic elasticity tensors, by introducing "trace-bounds". These trace bounds, categorized as 'bulk modulus type' and 'shear moduli type', are derived by bounding the trace of the inverse stiffness tensor (compliance tensor) projected onto specific tensor subspaces. These calculations establish bounds on a certain combination of elastic moduli. However, extending this method to fully anisotropic media with shear-normal coupling is non-trivial. This is because the energy cannot be decomposed into simple tensor components but involves a combination of them for any type of loading.

To bridge this gap, Milton and Camar-Eddine [99] expanded upon the theories proposed by [95, 98] on isotropic composites to explore bounds on arbitrary stress-strain pairs in the anisotropic composites. The key finding from this work is that sequentially layered laminates are shown to achieve these bounds on stress-strain pairs. By examining the sum of energy and complementary energies, they show that integrating a rank-deficient pentamode material within hierarchical laminates enables the attainment of extremality in the stress-strain space. Pentamode materials were first introduced by Milton and Cherkaev [23], suggesting that using pentamode materials as fundamental building blocks allows for the achievement of arbitrary effective anisotropic properties. Generally, elasticity tensors of extremal materials exhibit rank deficiency [100, 101], a characteristic shared by pentamode materials and hierarchical laminates. Additionally, hierarchical laminates also emerge as energy-minimizing optimal structures in various microstructure evolution problems [102–105], as they are shown to achieve constant stress or strain in one of the phases and leading to the optimization of the translation bounds [106].

While hierarchical structures and other rank-deficient materials could serve as a design guide in realizing extreme elastic anisotropy, physically realizing such structures demands advanced fabrication techniques that are still in development. There is limited knowledge about the elasticity tensors achievable with single-scale fabrication techniques. In this paper, we address this gap

by sampling a diverse database of anisotropic unit cells created by combining periodic cosine functions of varied spatial frequencies, as discussed in Section 2.3. The database properties are then compared with the properties of hierarchical laminates in for the first time (to the best of our knowledge) which are considered as theoretical bounds. This comparison helps identify the regions in the property space where hierarchical design is necessary to achieve extreme elastic anisotropy.

3.2 Theory of bounds on anisotropic elasticity tensors

For isotropic composites, Hashin and Shtrikman [93, 94] introduced a variational approach to determine the upper and lower bounds on the effective bulk and shear moduli (κ^* and μ^*) by decomposing the elastic energy into hydrostatic and deviatoric parts. However, the elastic energy cannot be decomposed to get variational bounds on the independent moduli in the anisotropic case. Recently Milton and Camar-Eddine [99], Milton et al. [107] addressed this problem in terms of the stress and strain energy pairs and establishing bounds on the sum of the elastic and the complementary energies. Let the four energy functions $W_f^k, k = 0, 1, \ldots, 3$, that characterize the set GU_f of possible elastic tensors $\mathbf{C}_*$ be defined by

$$W_f^0\left(\sigma_1^0, \sigma_2^0, \sigma_3^0\right) = \min_{C_* \in GU_f} \sum_{j=1}^{3} \sigma_j^0 : C_*^{-1} \sigma_j^0, \tag{3.1a}$$

$$W_f^1\left(\sigma_1^0, \sigma_2^0, \varepsilon_1^0\right) = \min_{C_* \in GU_f} \left[\varepsilon_1^0 : C_* \varepsilon_1^0 + \sum_{j=1}^{2} \sigma_j^0 : C_*^{-1} \sigma_j^0 \right], \tag{3.1b}$$

$$W_f^2\left(\sigma_1^0, \varepsilon_1^0, \varepsilon_2^0\right) = \min_{C_* \in GU_f} \left[\left(\sum_{i=1}^{2} \varepsilon_i^0 : C_* \varepsilon_i^0 \right) + \sigma_1^0 : C_*^{-1} \sigma_1^0 \right], \tag{3.1c}$$

$$W_f^3\left(\varepsilon_1^0, \varepsilon_2^0, \varepsilon_3^0\right) = \min_{C_* \in GU_f} \sum_{i=1}^{3} \varepsilon_i^0 : C_* \varepsilon_i^0. \tag{3.1d}$$

Each energy function $W_f^k, k = 0, 1, \ldots, 3$, here represents the sum of three elastic energies, each obtained from an experiment where the composite, with effective tensor $\mathbf{C}^*$, is either subject to an applied stress σ_i^0 or an applied strain ε_i^0. A total of three stresses σ_i^0 and ε_i^0 are applied simultaneously on the composite. The optimization of these energies to find C^* for the applied stresses and strains is non-trivial. However, applying the key conclusions from [95, 98, 108], Milton and Camar-Eddine [99], Milton et al. [107] discuss how sequentially layered laminates (or hierarchical laminates) minimize the sum of energies and complementary energies. In other words, G-closure can be seen as the G-closure of hierarchical laminates which is explained in Fig. 3.1. In two-dimensions, it is sufficient to consider laminates up to rank-3, if the constituent phases are isotropic. It is also worth noting that hierarchical laminates, with isotropic type effective elasticity tensor, simultaneously achieve Hashin-Shtrikman bulk and shear bounds [66].

Construction of hierarchical laminates

Multiple-rank laminate materials are hierarchical materials created through an iterative lamination process at increasingly larger length scales. A rank-one laminate consists of two isotropic phases, which can be viewed as rank-zero laminates. A rank-(m) laminate is formed by layering a rank-$(m-1)$ laminate with a laminate of rank-$(m-1)$ or lower, as shown in Fig. 3.1. In two dimensions, it is sufficient to consider laminates up to rank-3 to estimate theoretical bounds, especially when the constituent materials are isotropic, as the 2D elasticity tensor has only three eigenvalues. Rank-1 laminates typically have one very high non-zero eigenvalue and two near-zero eigenvalues, while rank-2 laminates have two very high non-zero eigenvalues and one near-zero eigenvalue. To compute the effective properties of a higher rank-m laminate, the constituent phases are replaced from isotropic to the relevant anisotropic phases of rank-$(m-1)$ laminates (See Figs. 3.7 to 3.9). A rank-1 laminate is strictly defined by two parameters, the fill fraction of the stiff phase and the angle of orientation of the lamination. A rank-2 laminate is defined by four extra parameters the fill fraction of the stiff phase and the angle of orientation of each of the phases of the previous rank-1 laminate. Similarly, a rank-3 laminate is defined by eight extra parameters. Suppose, there are 11 different fill fractions and 18 different laminate orientations. This results in a total of $11 \times 18 = 198$ elasticity tensors for rank-1 laminates. For rank-2 laminates, the total number of possible elasticity tensors is $(11 \times 18)^3 = 7762392$. For rank-3 laminates, the number increases to $(11 \times 18)^7$. First, the effective properties of all the rank-1 laminates are obtained by using two isotropic constituent phases for homogenization. To compute the effective properties of higher rank-m laminates, the constituent phases are replaced from isotropic to the relevant anisotropic phases of lower rank (see Figs. 3.7 to 3.9). To reduce the number of computations for the rank-3 laminates database, a subset of randomly chosen rank-2 elasticity tensors (about 1%) are used.
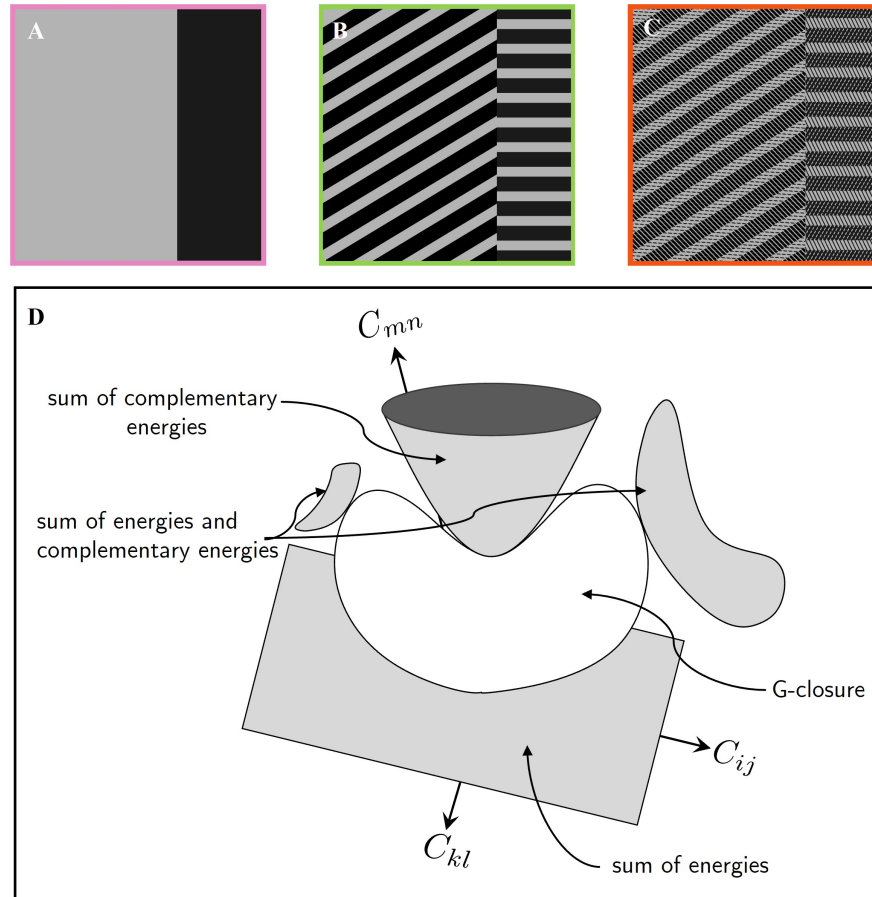
Figure 3.1: Hierachical laminates: (A,B,C) Construction of hierarchical laminates of rank-1, rank-2 and rank-3 respectively. For rank-2 laminates, the stiff and soft phases of rank-1 are further laminated in an arbitrarily chosen direction, not necessarily identical to the lamination direction of the rank-1 laminate. Similarly for rank-3 laminates, each rank-1 lamination in rank-2 laminate is laminated again in arbitrary directions. The fill fraction and relative orientation in each sequence of hierarchy are fixed to show the distinction of hierarchy. (D) G-closures are defined by the minimum values of sums of energies and complementary energies. The coordinates represent components of the elasticity tensor. The convexity of the G-closure ensures that the surfaces of energies and complementary energies touch every point tangentially on its boundary (adapted from Figure 30.1 in [6]). Further, it has been shown that the composites that lie on the boundary of this G-closure are usually hierarchical laminates.

3.3 Stiffness matrix derivation for rank-2 and rank-3 laminate homogenization

Initial discussion on the homogenization involving two isotropic phases is adopted from Andreassen and Andreasen [67] and is included here only for completeness. Later, we describe the modifications necessary to account for the anisotropy of the individual phases.

According to the theory of homogenization [67], the macroscopic elasticity tensor C_{ijkl}^H of a periodic composite can be computed by considering the first-order terms in the asymptotic expansion of the displacement field as

$$C_{ijkl}^H = \frac{1}{|V|} \int_V C_{pqrs} \left(\varepsilon_{pq}^{0(ij)} - \varepsilon_{pq}^{(ij)} \right) \left(\varepsilon_{rs}^{0(kl)} - \varepsilon_{rs}^{(kl)} \right) dV, \tag{3.2}$$

where $|V|$ denotes the volume of the unit cell, C_{pqrs} is the locally varying stiffness tensor, $\varepsilon_{pq}^{0(ij)}$ are prescribed macroscopic strain fields (in 2D there are three; e.g. unit strain in the horizontal direction (11), unit strain in the vertical direction (22), and unit shear strain (12 or 21)), while the locally varying strain fields $\varepsilon_{pq}^{(ij)}$ are defined as

$$\varepsilon_{pq}^{(ij)} = \varepsilon_{pq} \left(\chi^{ij} \right) = \frac{1}{2} \left(\chi_{p,q}^{ij} + \chi_{q,p}^{ij} \right), \tag{3.3}$$

based on the displacement fields χ^{kl} found by solving the elasticity equations with a prescribed macroscopic strain

$$\int_V C_{ijpq} \varepsilon_{ij}(v) \varepsilon_{pq} \left(\chi^{kl} \right) dV = \int_V C_{ijpq} \varepsilon_{ij}(v) \varepsilon_{pq}^{0(kl)} dV \quad \forall v \in V, \tag{3.4}$$

where v is a virtual displacement.

The elasticity equation from Eq. (3.4) can be discretized using the finite element method. The left hand side, i.e., the stiffness matrix, yields:

$$\mathbf{K} = \sum_{e=1}^N \int_{V_e} \mathbf{B}_e^T \mathbf{C}_e \mathbf{B}_e \, dV_e. \tag{3.5}$$

The discretization of the right hand side of Eq. (3.4) is the loads $\mathbf{f}$ which correspond to macroscopic volumetric straining

$$\mathbf{f}^i = \sum_e \int_{V_e} \mathbf{B}_e^T \mathbf{C}_e \varepsilon^i \, dV_e. \tag{3.6}$$

In computing the effective properties of rank-2 and rank-3 laminates, each of the constituent phases used for homogenization are anisotropic. Therefore, the stiffness matrix described in Eq. (3.4), should be modified to account for the anisotropy of the individual phases.

This is done by changing the definition of the stiffness matrix for a completely anisotropic Q4 finite element, defined as $\mathbf{K}'$

$$\mathbf{K}' = C_{11} \times K_{11} + C_{12} \times K_{12} + C_{22} \times K_{22} + C_{16} \times K_{16} + C_{26} \times K_{26} + C_{66} \times K_{66}, \qquad (3.7)$$

where C_{ij} are the anisotropic moduli of the material occupying the Q4 element.

Here $K_{11}, K_{12}, K_{22}, K_{16}, K_{26}, K_{66}$ are obtained upon integration in Eq. (3.5), assuming plane-strain condition as

$$K_{11} = \frac{1}{6} \begin{pmatrix} 2 & 0 & -2 & 0 & -1 & 0 & 1 & 0 \\ 0 & 0 & 0 & 0 & 0 & 0 & 0 & 0 \\ -2 & 0 & 2 & 0 & 1 & 0 & -1 & 0 \\ 0 & 0 & 0 & 0 & 0 & 0 & 0 & 0 \\ -1 & 0 & 1 & 0 & 2 & 0 & -2 & 0 \\ 0 & 0 & 0 & 0 & 0 & 0 & 0 & 0 \\ 1 & 0 & -1 & 0 & -2 & 0 & 2 & 0 \\ 0 & 0 & 0 & 0 & 0 & 0 & 0 & 0 \end{pmatrix}, \qquad (3.8)$$

$$K_{12} = \frac{1}{12} \begin{pmatrix} 0 & 3 & 0 & 3 & 0 & -3 & 0 & -3 \\ 3 & 0 & -3 & 0 & -3 & 0 & 3 & 0 \\ 0 & -3 & 0 & -3 & 0 & 3 & 0 & 3 \\ 3 & 0 & -3 & 0 & -3 & 0 & 3 & 0 \\ 0 & -3 & 0 & -3 & 0 & 3 & 0 & 3 \\ -3 & 0 & 3 & 0 & 3 & 0 & -3 & 0 \\ 0 & 3 & 0 & 3 & 0 & -3 & 0 & -3 \\ -3 & 0 & 3 & 0 & 3 & 0 & -3 & 0 \end{pmatrix}, \qquad (3.9)$$

$$K_{22} = \frac{1}{6} \begin{pmatrix} 0 & 0 & 0 & 0 & 0 & 0 & 0 & 0 \\ 0 & 2 & 0 & 1 & 0 & -1 & 0 & -2 \\ 0 & 0 & 0 & 0 & 0 & 0 & 0 & 0 \\ 0 & 1 & 0 & 2 & 0 & -2 & 0 & -1 \\ 0 & 0 & 0 & 0 & 0 & 0 & 0 & 0 \\ 0 & -1 & 0 & -2 & 0 & 2 & 0 & 1 \\ 0 & 0 & 0 & 0 & 0 & 0 & 0 & 0 \\ 0 & -2 & 0 & -1 & 0 & 1 & 0 & 2 \end{pmatrix} \qquad (3.10)$$

$$K_{16} = \frac{1}{6} \begin{pmatrix} 3 & 2 & 0 & -2 & -3 & -1 & 0 & 1 \\ 2 & 0 & -2 & 0 & -1 & 0 & 1 & 0 \\ 0 & -2 & -3 & 2 & 0 & 1 & 3 & -1 \\ -2 & 0 & 2 & 0 & 1 & 0 & -1 & 0 \\ -3 & -1 & 0 & 1 & 3 & 2 & 0 & -2 \\ -1 & 0 & 1 & 0 & 2 & 0 & -2 & 0 \\ 0 & 1 & 3 & -1 & 0 & -2 & -3 & 2 \\ 1 & 0 & -1 & 0 & -2 & 0 & 2 & 0 \end{pmatrix} \tag{3.11}$$

$$K_{26} = \frac{1}{6} \begin{pmatrix} 0 & 2 & 0 & 1 & 0 & -1 & 0 & -2 \\ 2 & 3 & 1 & 0 & -1 & -3 & -2 & 0 \\ 0 & 1 & 0 & 2 & 0 & -2 & 0 & -1 \\ 1 & 0 & 2 & -3 & -2 & 0 & -1 & 3 \\ 0 & -1 & 0 & -2 & 0 & 2 & 0 & 1 \\ -1 & -3 & -2 & 0 & 2 & 3 & 1 & 0 \\ 0 & -2 & 0 & -1 & 0 & 1 & 0 & 2 \\ -2 & 0 & -1 & 3 & 1 & 0 & 2 & -3 \end{pmatrix}, \tag{3.12}$$

$$K_{66} = \frac{1}{12} \begin{pmatrix} 4 & 3 & 2 & -3 & -2 & -3 & -4 & 3 \\ 3 & 4 & 3 & -4 & -3 & -2 & -3 & 2 \\ 2 & 3 & 4 & -3 & -4 & -3 & -2 & 3 \\ -3 & -4 & -3 & 4 & 3 & 2 & 3 & -2 \\ -2 & -3 & -4 & 3 & 4 & 3 & 2 & -3 \\ -3 & -2 & -3 & 2 & 3 & 4 & 3 & -4 \\ -4 & -3 & -2 & 3 & 2 & 3 & 4 & -3 \\ 3 & 2 & 3 & -2 & -3 & -4 & -3 & 4 \end{pmatrix}. \tag{3.13}$$

3.4 Data visualizations

Our goal is to identify the range of effective anisotropic elasticity tensors that can be achieved from periodic single-scale unit-cells composed of two isotropic phases. Further to build a database, the coefficients A_{mn} are sampled randomly to generate 2000 different functions and the threshold is varied for 100 increments resulting in a database size of 200000 unit cells.

Volume fraction plots

In Fig. 3.2, the data of material properties C_{11}, C_{12}, C_{16} is plotted as a function of the fill fraction of the stiff phase. All the parameters are normalized with Young's Modulus of the stiff phase. Note that C_{22}, C_{66} have similar property distribution as that of C_{11} while C_{26} property distribution is similar to C_{16} and hence these parameters are not plotted for brevity. As there are no closed-form

expressions for the theoretical bounds on anisotropic moduli, the range of properties achieved by hierarchical laminates upto rank-3 is used as a substitute and indicated in the same plots. Please refer to Section 3.2 for a discussion on theoretical bounds and Section 3.2 and Fig. 3.1 for the construction and computation of the effective properties of the hierarchical laminates. First, we observe that in all property plots, rank-2 laminates (shown in green) significantly expand the property range compared to rank-1 laminates (shown in magenta). However, the transition from rank-2 to rank-3 laminates (shown in orange) shows minimal improvement across all moduli except for C_{12}. For C_{12}, the negative region is only accessible with rank-3 laminates, and this range shows minimal dependence on the fill fraction beyond 25%. Both rank-2 and rank-3 laminates reduce the strong dependence on achieving higher values for specific moduli, allowing stiffer anisotropic properties beyond linear scaling with a low fraction of the stiff phase. Additionally, hierarchical laminates demonstrate that using anisotropic constituent phases can significantly enhance the range of achievable properties in single-scale two-phase composites.
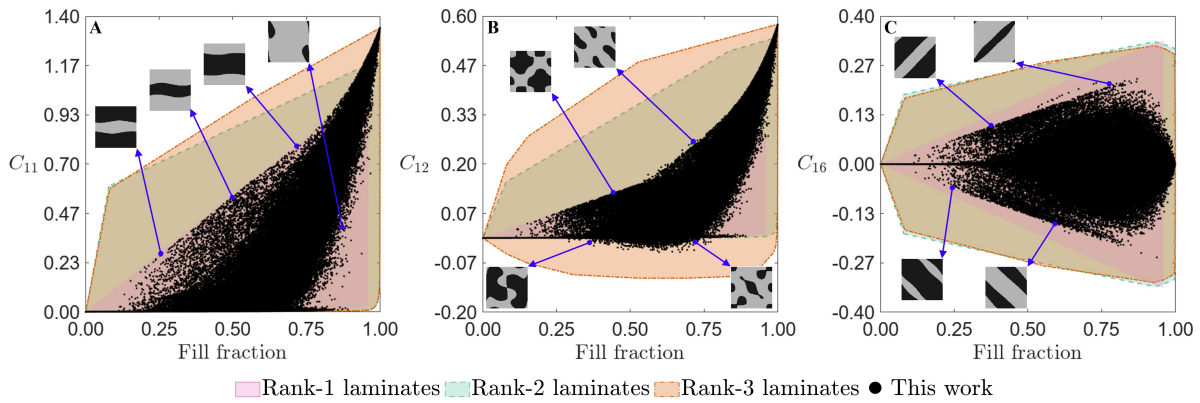
Figure 3.2: Plots of fill fraction of stiff phase vs. (A) C_{11}, (B) C_{12}, (C) C_{16} from this database. All the plots are normalized with the Young's modulus of the stiff material. Properties of hierarchical laminates are used as theoretical bounds. Rank-1 laminates are indicated with magenta color, rank-2 laminates are indicated with green color and rank-3 laminates are indicated with orange color. Representative unit cells at the boundary are pointed out using arrows. The unit cells away from the bounds contain non-trivial patterns and some of them are displayed in the subsequent figures.

Our database consisted of unit cells achieving the bounds predicted by rank-1 laminates, specifically in the fill fraction ranging between 30%–80%. To understand the effect of spatial frequencies, the same plots are plotted in different colors with data constructed from adding a specific number of spatial frequencies (Fig. 3.3). It is observed that adding higher spatial modes does not necessarily increase the reach in the property space. In fact, adding higher spatial modes is detrimental to producing anisotropic structures beyond spatial modes of order 3. While square unit cells were sufficient to explore the extremes of the diagonal moduli, the range of the off-diagonal moduli is

enhanced with the use of non-square unit cells (Fig. 3.4). For C_{11}, the structures at the upper bound are laminate-like structures aligned along the x_1 direction, while those at the lower bound are laminates aligned along the x_2. For C_{12}, the unit cells at the upper and lower bounds are non-laminate-like. In the negative C_{12}, the discovered unit cells do not approach the bounds of rank-3 laminates and feature chiral patterns and/or orthogonally aligned thin features. For C_{16}, the upper bound unit cells are skew laminates tilted towards right, while those at the lower (negative) bound are the same skew laminates, but flipped.
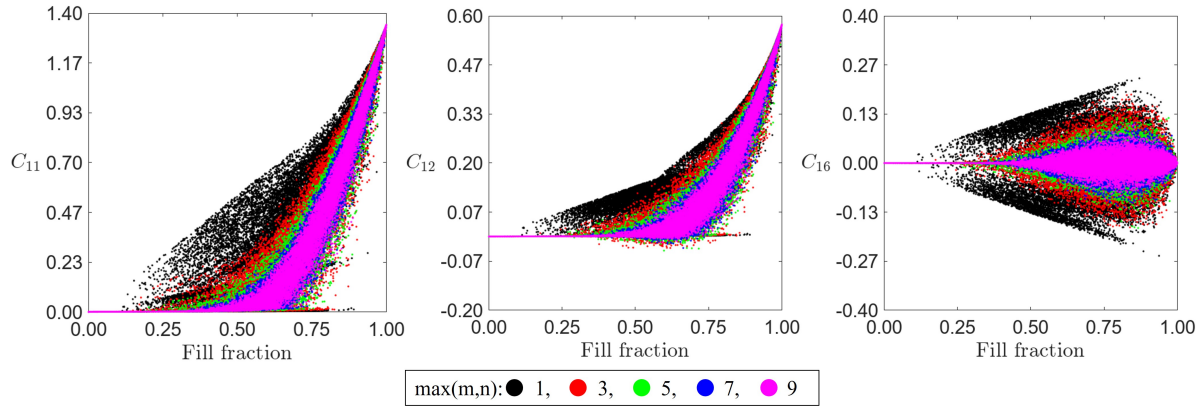
Figure 3.3: Plots of fill fraction of stiff phase vs C_{11}, C_{12}, C_{16} from this database as the maximum number of spatial modes is varied. All the plots are normalized with the Young's modulus of the stiff material. Adding higher spatial modes does not increase the span in the material properties.
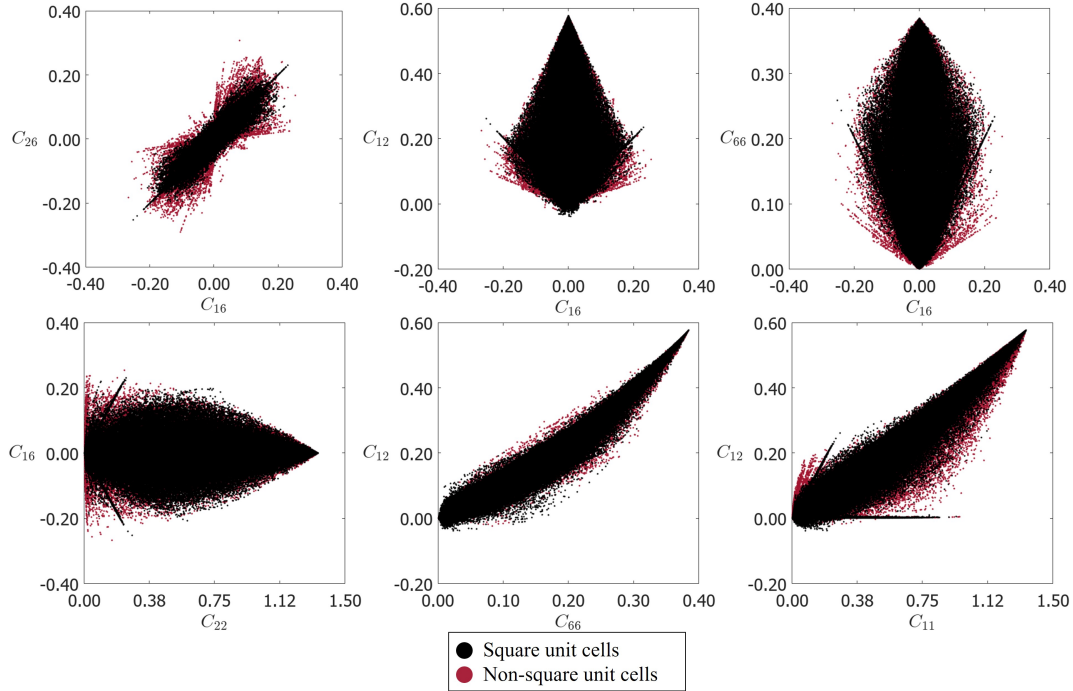
Figure 3.4: Comparison of the properties from square and non-square unit cells. Non-square unit cells contain patterns that are periodic along non-orthogonal directions. The span in the off-diagonal properties is enhanced by non-square unit cells, especially C_{16}, C_{26}. Off-diagonal moduli C_{16}, C_{26} have high dependence on the unit cell shape and symmetries.

Hierarchical architectures play a significant role in structural integrity and functionality across systems of various length scales (e.g., spider silk) [109]. This hierarchy is often present in non-rectangular coordinate systems. For example, wire ropes used in structural engineering contain helical strands arranged in a hierarchical manner, enhancing efficient load transfer and their strength by distributing tensile forces uniformly throughout the cross-section, regardless of the bending direction [110]. In biological systems, spinal discs, which are annular cylinders surrounding the spine in the vertebrae, provide shock absorption, support, and flexibility to the spine. Their load-bearing protein, collagen, is distributed in a multi-layered laminar fashion [111]. Similarly, the tympanic membrane of the human ear, which is responsible for efficient sound transmission and protecting the delicate structures within the ear, is conical in shape and features collagen structured in a trilaminar fashion with radial and circumferential patterns [112]. These observations along with findings from our work further emphasize the importance of incorporating hierarchical designs to enhance the design capabilities.

Pair property plots

Often, multiple components of the elasticity tensor contribute to the overall mechanical behavior. Therefore, we also examine the pair property plots. For a total of 6 material parameters, there are a total of $\binom{6}{2}$ = 15 distinct pair property plots. However, due to the symmetry nature of the property plots, it is sufficient to consider only a subset of the plots. For example, the property plot of C_{11} vs C_{16} would be the same as C_{22} vs C_{26}. As the goal of this paper is to identify anisotropic structure-property relations, specifically shear-normal coupling, the property plots associated with the off-diagonal parameters of the elasticity tensor are discussed in detail. Therefore, the property plots corresponding to C_{16} vs. C_{26}, C_{16} vs. C_{12}, C_{11} vs. C_{22}, C_{66} . C_{12} are shown in Fig. 3.5. Please refer to Fig. 3.6 for the rest of the pair-property plots. In the same plots, as discussed earlier, the range of properties achieved by hierarchical laminates are used as a substitute for theoretical bounds (which are plotted separately in Figs. 3.7 to 3.9 to indicate their distinction).

In the property plot of C_{16} vs. C_{26} shown in Fig. 3.5A, we observe that there is a strong correlation along the line inclined at 45°. This means for many of the unit cells, both C_{16} and C_{26} have the same sign. Hierarchical laminates uncorrelated this behavior and achieved unit cells with opposing signs for C_{16} and C_{26}. The unit cells identified on the boundary of this property space resemble rank-1 laminates. However extremal strict low rank-1are not allowed in the ansatz for database construction. As discussed in Forte and Vianello [63], $C_{16} + C_{26}$ and $C_{16} - C_{26}$ are components of the invariants of the elasticity tensor under coordinate transformation. Each of these sums signifies a different contribution to the stored elastic energy (see Eqs. (2.21) and (2.22) in Section 2.2). In the property plots of C_{66} vs. C_{12} and C_{11} vs. C_{12} shown in Fig. 3.5E-F, there are generally very few data points with a negative value of C_{12}, especially at high values of C_{66}. Again, the negative region for C_{12} is only accessible with rank-3 laminates. The combination $\kappa = \frac{1}{4}(C_{11} + C_{22} + 2C_{12})$, known as the bulk modulus, is an invariant. This imposes a restriction on the negative bound of C_{12} to ensure that κ remains positive. The parameter $C_{66} - C_{12}$ is invariant under coordinate transformation. Therefore, C_{66} vs. C_{12} plot for rank-1 laminates is strictly a single linear line. C_{66} vs. C_{12} plot for rank-2 and rank-3 laminates is composed of several such lines with different slopes, which is clearly observed in Fig. 3.8.

In Fig. 3.10 and Fig. 3.11, the data of the eigen values ($\lambda_1, \lambda_2, \lambda_3$ in descending order) of all the elasticity tensors computed are plotted. For rank-1 laminates, λ_2, λ_3 are very close to zero, while for rank-3 laminates, only λ_3 is very close to zero. Rank-3 laminates exhibited a broad spectrum of eigenvalues, with notably high eigenvalues observed at low fill fractions. In the fill fraction ranging between 30% - 80%, the eigen value data from the unit cell database In Fig. 3.12, pair-property plots of the invariants discussed in Chapter 2 are plotted. The invariant data for just rank-2 laminates is plotted in Fig. 3.13. Rank-1 laminate data for all the plots (invariant data and eigen value data) is

observed to lie on a single curve. There are regions in the plots associated with J_2 that are accessible only with rank-2 and rank-3 laminates. J_2 is a measure of the squared norm of the anisotropic part of the deviatoricity of the material. Therefore, invariants could serve as more effective metrics for designing and quantifying anisotropy.

3.5 Conclusion

In this chapter, we estimate the range of anisotropic elasticity tensors by creating a database of two-dimensional unit cells consisting of two isotropic phases with contrasting moduli. We compare the property ranges achieved by these single-scale architected materials with the extensive design space achieved by hierarchical materials, which reach bounds predicted by theoretical calculations for these parameters. We identify regions in the property space where hierarchical designs or the use of two anisotropic constituents are necessary to cover a wide property space, particularly focusing on off-axis parameters. The bounds provided alongside the unit cells serve as a design tool for the design of extremal metamaterials. In the next chapter, we discuss the experimental evaluation of the mechanical parameters tested on four different specimens.
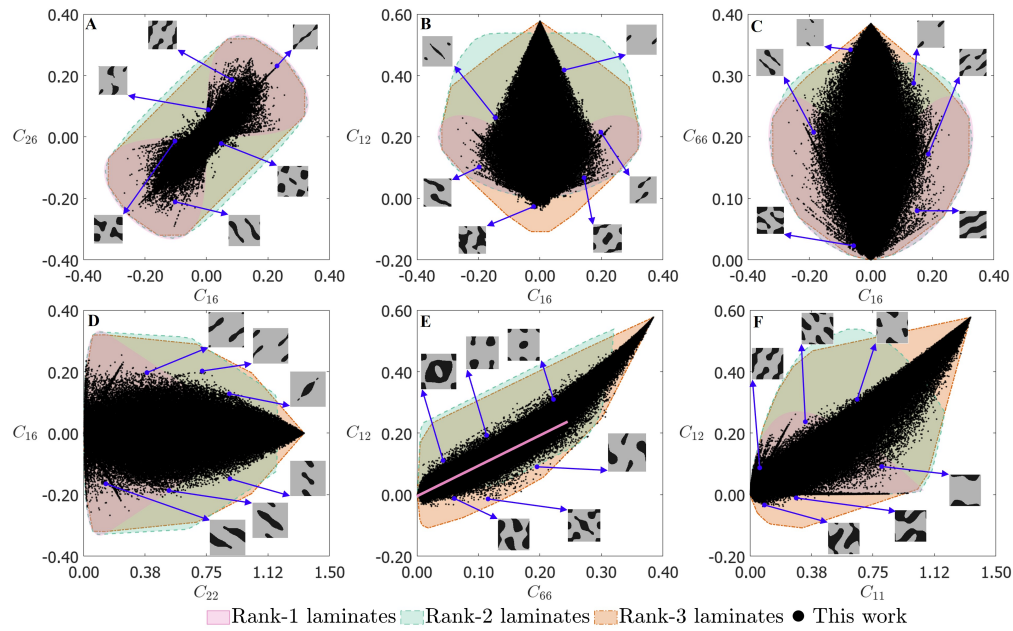
Figure 3.5: Plots of (A) C_{16} vs. C_{26}, (B) C_{16} vs. C_{12}, (C) C_{16} vs. C_{66}, (D) C_{22} vs. C_{16} (E) C_{66} vs. C_{12} and (F) C_{11} vs. C_{12} from this database. All the plots are normalized with the Young's modulus of the stiff phase shown in gray color. Rank-1 laminates are indicated with magenta color, rank-2 laminates are indicated with green color and rank-3 laminates are indicated with orange color. Representative unit cells at the boundary are pointed out using arrows.
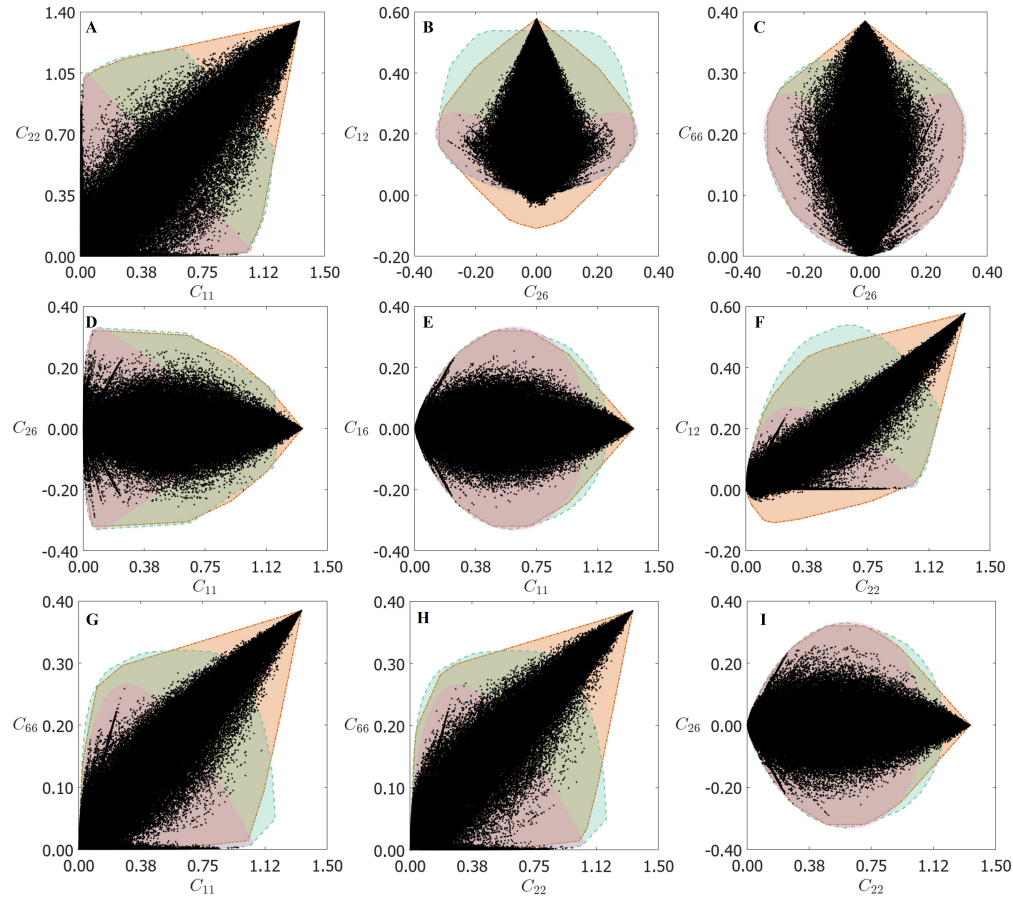
Figure 3.6: Plots of (A) C_{11} vs. C_{22}, (B) C_{26} vs. C_{12}, (C) C_{26} vs. C_{66}, (D) C_{11} vs. C_{26}, (E) C_{11} vs. C_{16}, (F) C_{22} vs. C_{12}, (G) C_{11} vs. C_{66}, (H) C_{22} vs. C_{66} and (I) C_{22} vs. C_{26} from this database. All the plots are normalized with the Young's modulus of the stiff material shown in gray color in the unit cells displayed. Rank-1 laminates are indicated with magenta color, rank-2 laminates are indicated with green color and rank-3 laminates are indicated with orange color.
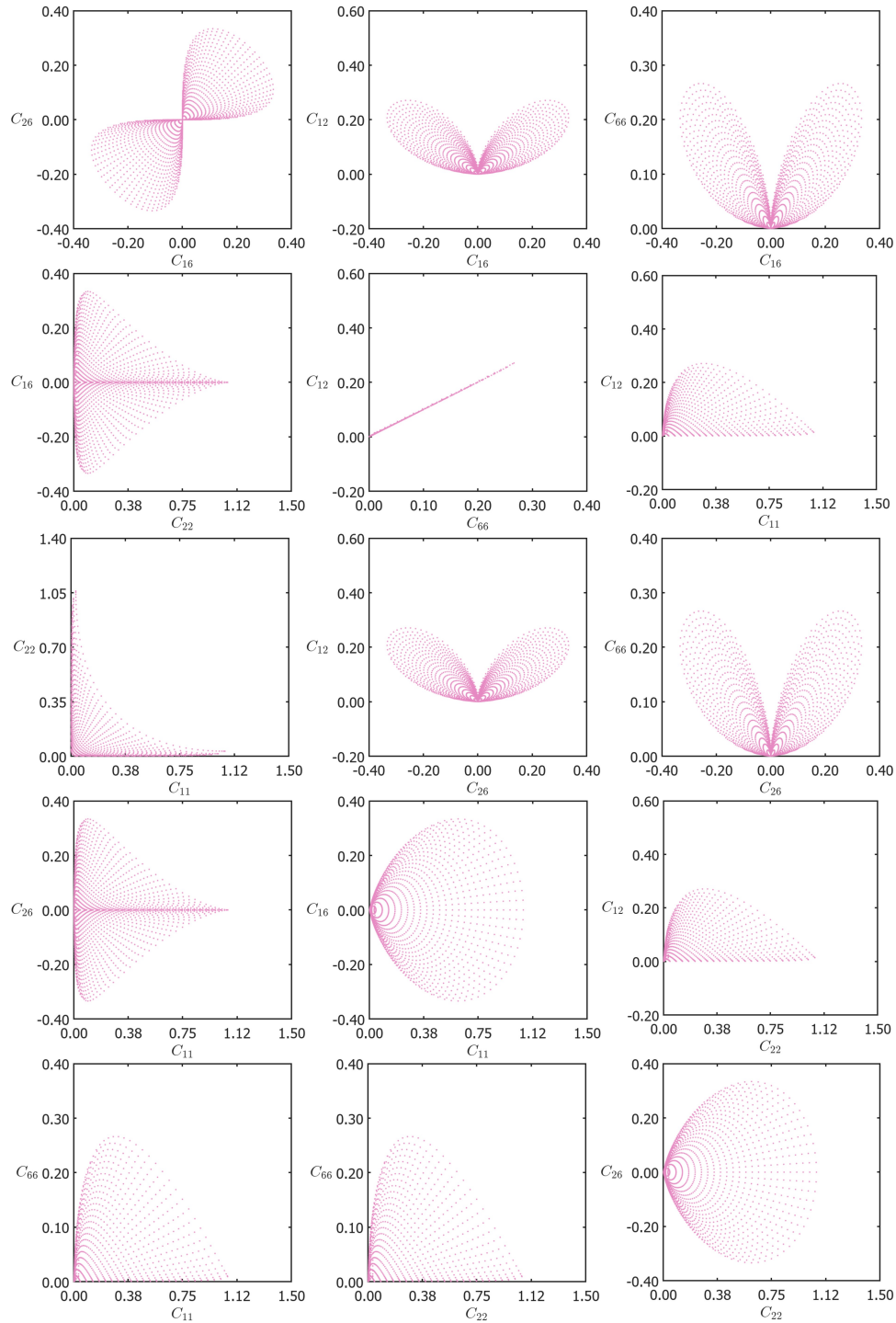
Figure 3.7: Pair property plots for rank-1 laminates. First, the properties of the laminates whose normal direction is aligned with x_1 direction are computed, as the fill fraction of stiff phase is incremented in intervals of 0.04 upto 0.96. Then, a co-ordinate transformation is applied on these tensors to obtain the properties of the laminates whose normal is not aligned with the co-ordinate axes.
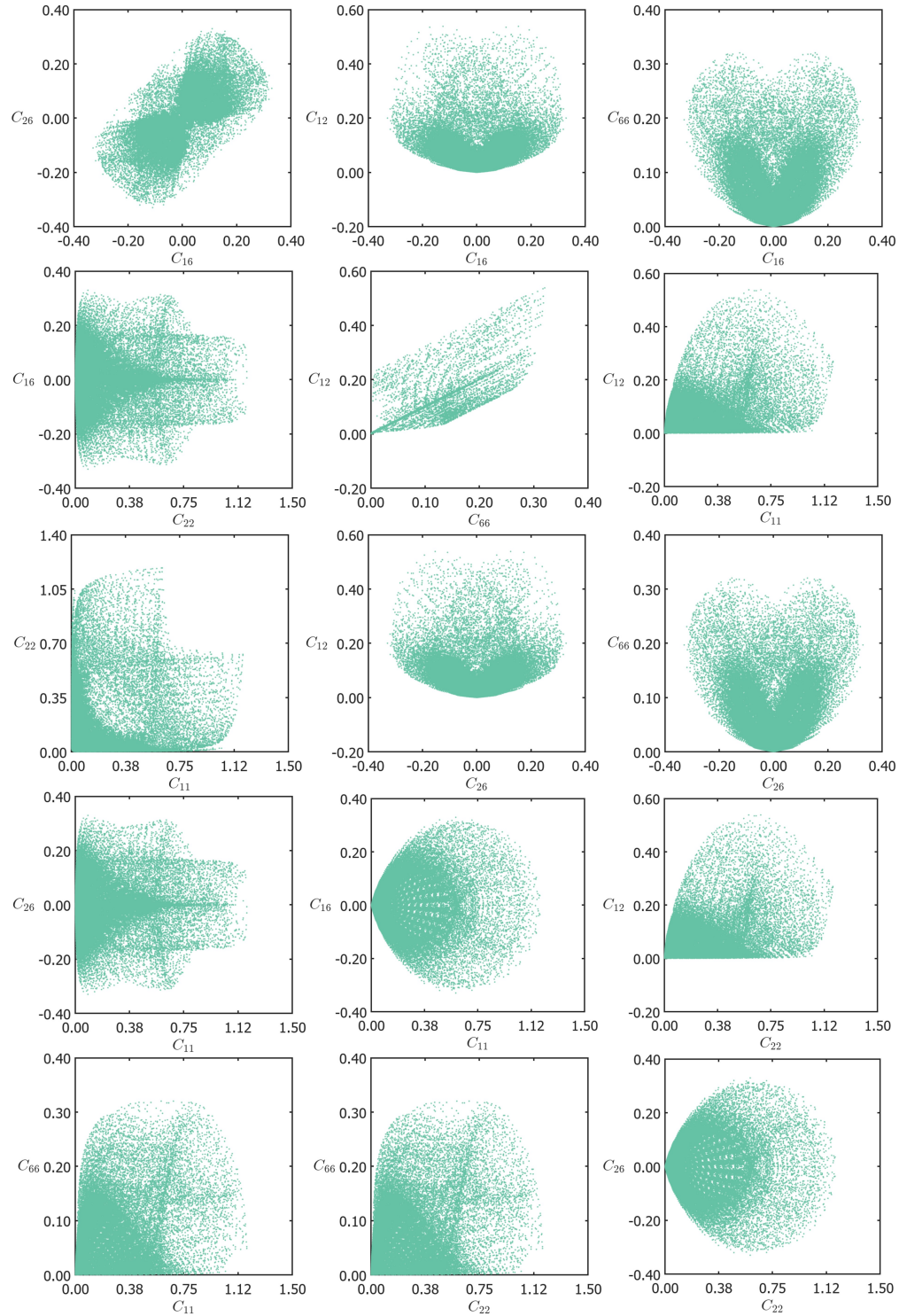
Figure 3.8: Pair property plots for rank-2 laminates including co-ordinate transformations. Note that the reach in the properties is increased from rank-1 laminates to rank-2 laminates. This can be clearly observed in the plots of C_{16} vs C_{26}, C_{11} vs C_{22}, C_{66} vs C_{12}.
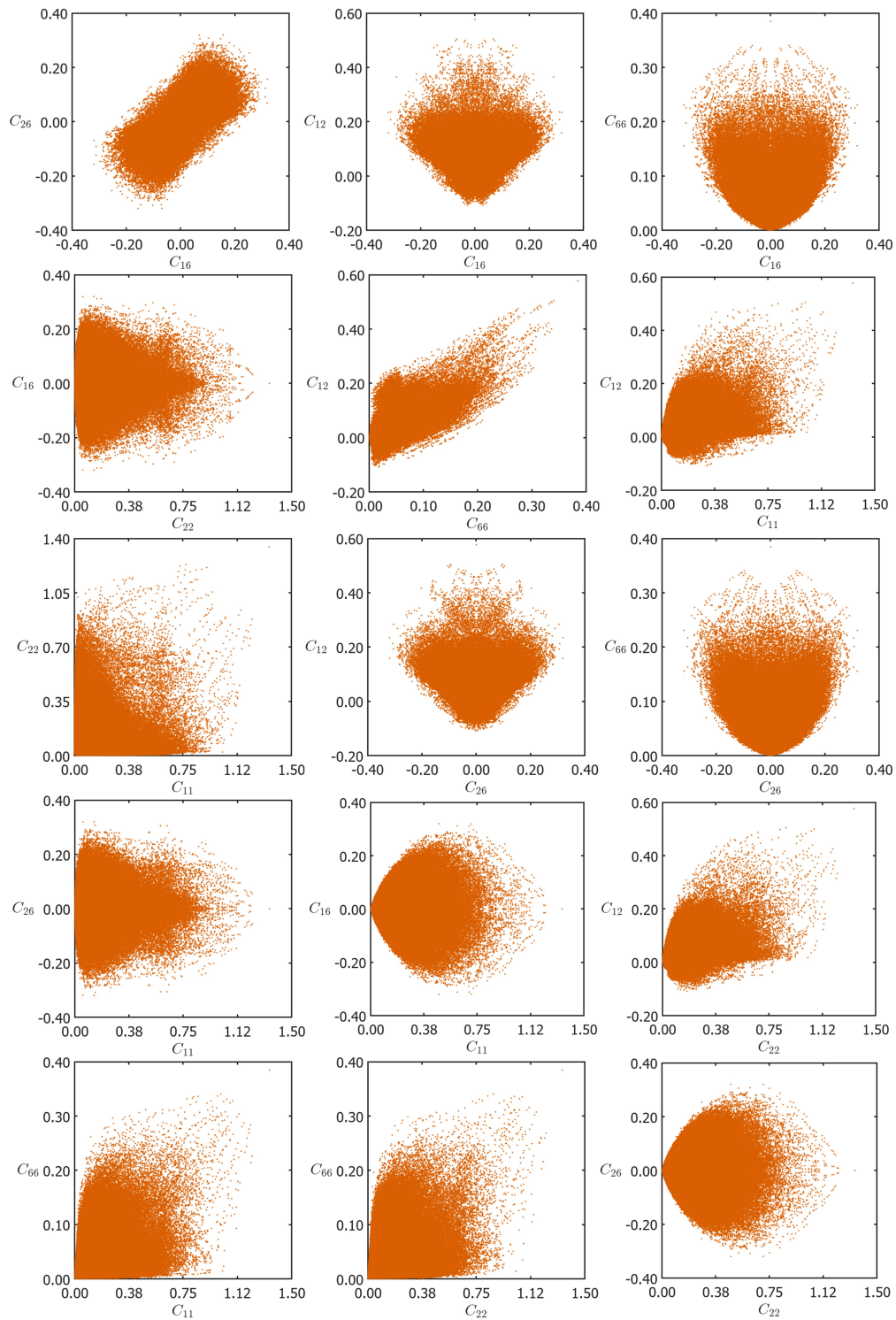
Figure 3.9: Pair property plots for rank-3 laminates including co-ordinate transformations.
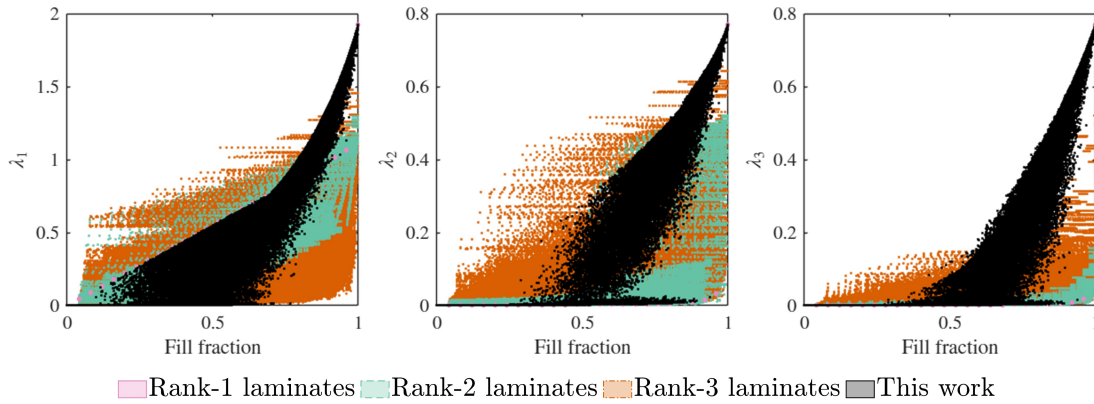
Figure 3.10: Eigen value vs. fill fraction plots. All the stiffness tensors are normalized with the Young's modulus of the stiff phase. Rank-1 laminates are indicated with magenta color, rank-2 laminates are indicated with green color and rank-3 laminates are indicated with orange color.
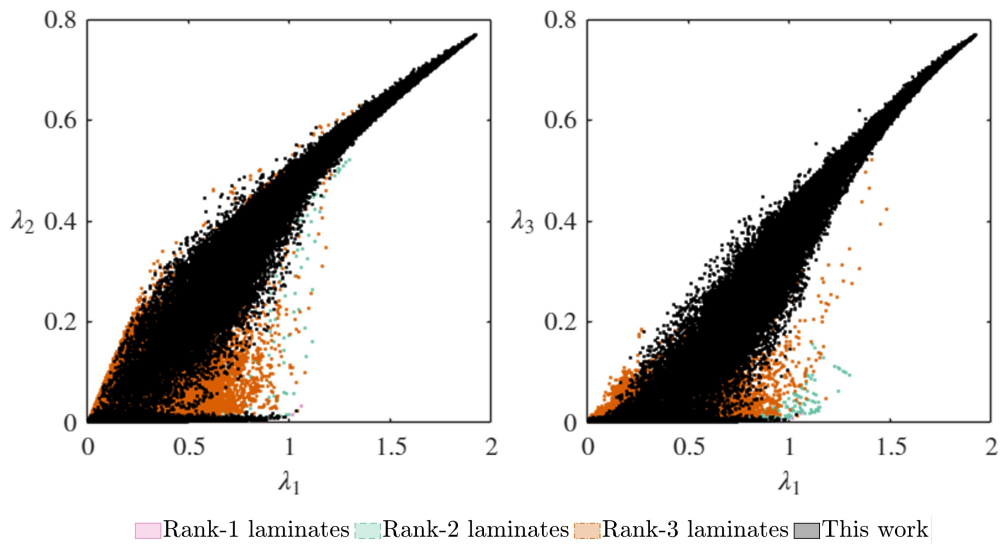
Figure 3.11: Pair property plots for the eigen value data. All the stiffness tensors are normalized with the Young's modulus of the stiff phase. Rank-1 laminates are indicated with magenta color, rank-2 laminates are indicated with green color and rank-3 laminates are indicated with orange color.
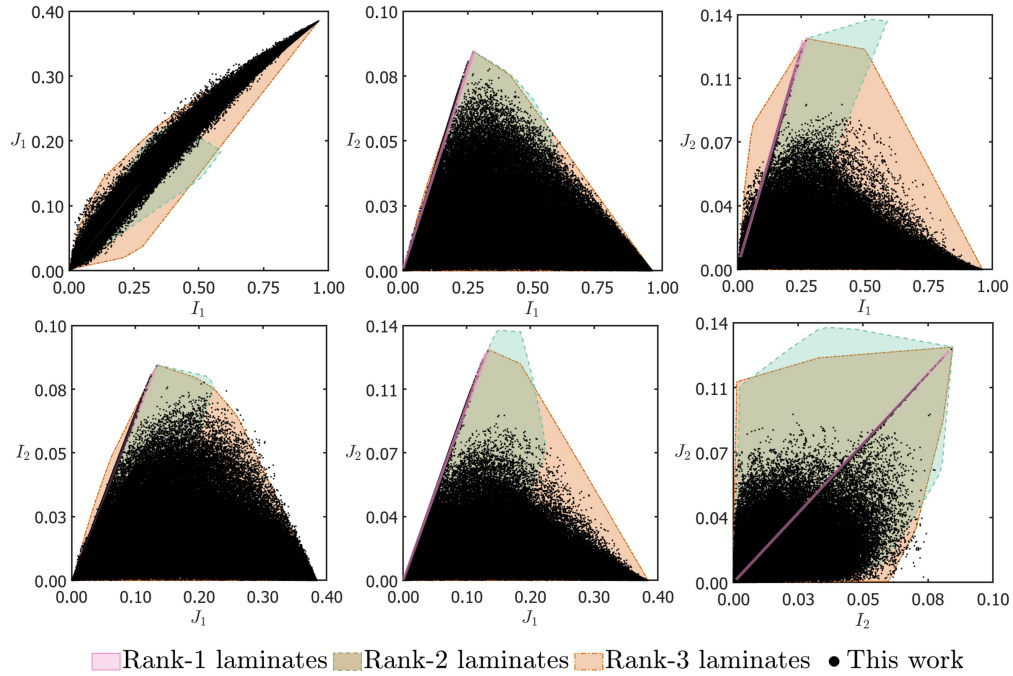
Figure 3.12: Pair property plots for the invariant data. All the stiffness tensors are normalized with the Young's modulus of the stiff phase. Rank-1 laminates are indicated with magenta color, rank-2 laminates are indicated with green color and rank-3 laminates are indicated with orange color.

Figure 3.13: Pair property plots for the invariant data of just rank-2 laminates. All the stiffness tensors are normalized with the Young's modulus of the stiff phase.

Chapter 4

SINGLE-TEST EVALUATION OF DIRECTIONAL ELASTIC PROPERTIES OF STRUCTURED MATERIALS

4.1 Introduction

In this chapter, our objective is to identify these six material parameters $C_{11}, C_{12}, C_{22}, C_{16}, C_{26}, C_{66}$ from experimental measurements with least number of experiments. Traditional material parameter identification methods rely on single-load experimental setups with homogeneous (constant) strain distributions within the tested specimen, which allow the derivation of closed-form stress-strain relations. However, the amount of data that can be acquired through a one dimensional tension test, for example, is limited (e.g., one stress-strain data pair for each measurement). When characterizing complex materials, multiple experimental setups with different loading conditions are needed. Full-field identification methods allow extracting additional information from single-load experiments. Measuring the full displacement field, e.g., through Digital Image Correlation (DIC), of arbitrarily shaped specimens under loading maximizes the amount of data generated from a single experimental test. Such data can then be used to characterize the material by applying inverse identification methods such as, among others, Finite Element Model Updating, the Equilibrium Gap Method or the Virtual Fields Method (VFM), see [113–115] for a review.

These methods have in common that they are used to calibrate the parameters of an a priori chosen material model, i.e., the mathematical functions and operations that describe the material response need to be fixed by means of the intuition or modeling experience of the user. However, the selection of inappropriate a priori assumptions about the model and its underlying mathematical structure can introduce errors. Recent research used full-field data to train machine-learning-models, whose versatile ansatz spaces promise to mitigate modeling errors. Flaschel et al. [116], for example, proposed the method EUCLID (Efficient Unsupervised Constitutive Law Identification and Discovery) that uses sparse regression [117] informed by full-field displacement data and net reaction force data, to automatically select interpretable material models from a potentially large predefined set of candidate material models. EUCLID has been applied to hyperelasticity [116], elastoplasticity [118], viscoelasticity [119], and generalized standard materials [120], see [121] for an overview. Further, EUCLID was formulated in a Bayesian setting by [122] to simultaneously

perform model selection and quantification of uncertainty in the material parameters. In contrast to selecting interpretable material models through sparse regression, full-field data may also be used to train black-box material model surrogates like neural networks, as shown by [123–125] for small strain elasticity and by Thakolkaran et al. [126] for hyperelasticity. In the present work, it is assumed that the material response does not leave the realm of elasticity at infinitesimal strains. Thus, the material model can be assumed to be known a priori, and its parameters are calibrated with the VFM.

The VFM, originally proposed by [127] (see also [128, 129]), employs the balance of linear momentum in its weak form, to identify unknown material parameters. The VFM method assumes that the kinematic fields in the specimen, as well as the reaction forces at the boundaries, are known from experiments. As such, material parameters remain the only unknowns in the balance equations and can be calculated using standard linear or nonlinear solvers. In essence, the VFM describes the inverse problem to the classical Finite Element Method (FEM). The method has been applied in various cases, such as small-strain elasticity, elasto-plasticity [130], and hyperelasticity [131], among others.

The accuracy of the VFM in identifying unknown material parameters and its sensitivity to noise is highly dependent on the choice of the functions for which the weak linear momentum balance is tested, also known as the virtual displacement fields. A distinction can be made between *global* virtual fields that are defined over the whole specimen domain, such as polynomials, and *local* virtual fields with compact support, such as in the Bubnov-Galerkin discretization with piecewise polynomial shape functions. As the choice of the virtual fields is arbitrary and user-dependent, several attempts have been made to automate and optimize it [132–134].

In this article, full-field measurement based identification, and in particular the VFM, is explored in the context of anisotropic structured materials and compared to traditional identification methods. We focus in particular on the identification of shear-normal coupling parameters, notoriously complex to extract from conventional experiments.

4.2 Virtual fields method for anisotropic metamaterials

Many parameter identification methods rely on conducting multiple experiments, which are time consuming, complex and require specialized equipment. To circumvent these drawbacks, we explore a material characterization method based on the VFM that solely relies on full-field displacements and net reaction force measurements from a single experimental test. In this section, after discussing the assumptions underlying the adoption of the VFM for metamaterials, we outline all the components of the proposed method.

Basic assumptions

The VFM [127–129] exploits the weak formulation of linear momentum balance, i.e., the principle of virtual work, as a constraint on the material parameter space. Since the full displacement field over the specimen and the net reaction forces at the specimen boundaries are known, testing the weak formulation for a suitable set of test functions (also known as virtual fields) results in a system of equations that can be solved for the unknown material parameters. By choosing the test functions as not constant in space, the linear momentum balance is tested in different regions of the considered specimen domain. As such, the VFM takes advantage of the local strain data, as opposed to global methods for parameter identification.

In the following, the VFM is used to characterize the mechanical behavior of metamaterials. However, it should be noted that, due to the non-homogeneous nature of the metamaterials, the application of identification methods based on full-field measurements is not trivial. Full-field measurement techniques such as DIC measure the kinematic fields locally, i.e., at several points on the considered specimen surface. The studied metamaterials are not expected to behave at these local points as their homogenized counterparts, especially when the number of repeating unit cells is low in comparison to the size of the specimen. To give an example, in Section 4.5 the deformation of a heterogeneous metamaterial specimen will be compared to that of an equally-dimensioned homogeneous body, whose stiffness is set to the homogenized stiffness of the metamaterial. Under the same loading conditions, the two specimens exhibit different local displacements, which is likely caused by local size effects and the different boundary conditions that are assumed during the loading of the macroscopic structure and the homogenization of the microscopic unit cell. It is observed that deviations between the kinematic fields are predominant at the boundary and in particular at the corners of the domain. This agrees with theoretical studies on heterogeneous metamaterials, which suggest the usage of non-local theories (e.g., higher-order strain-gradient based) as proposed by Mindlin and Eshel [135], to model size effects and wedge forces appearing at corners of non-homogeneous bodies [136–138]. Within this work, such theories are avoided for the sake of simplicity and to keep a reasonably low number of material parameters. Hence, the assumption is made that the global material behavior of the metamaterials can be characterized based on local kinematic measurements within a local constitutive theory. As we will see later, this assumption will introduce errors in the identification procedure, which are, however, below a practically relevant level. During the development of the VFM, we found that the locally measured kinematic data must be treated with care, especially at the boundary and the corners of the specimen. We will later introduce specifically designed virtual fields that reduce the influence of data acquired at the specimen boundary and corners (see Section 4.2 for details).[1]

---

[1]We note at this point that reducing the influence of data acquired at the specimen boundary and corners may be beneficial not only when studying heterogeneous materials. Even for homogeneous specimens, the acquisition of

Required data

To identify the unknown parameters, the VFM needs diverse local strain data, i.e., strain fields that are not homogeneous. Therefore, data that serve as input for the VFM are usually generated by testing complex specimen geometries under complex loading conditions [139, 140]. However, for the structured materials considered in this study, generating complex specimen geometries (e.g., a plate with holes or notches) and studying their behavior under complex loading conditions is not trivial. Local features like holes or notches may lead to stress concentrations or singularities and hence more complex geometries may be prone to behave locally inelastic or even fail. Further, we will show later that the VFM performs best if we do not feed the method with data at the boundary of the specimen. Introducing more features like holes or notches to the geometry would increase the boundary and thus reduce the amount of data suitable to be used by the VFM.

For our purposes we will show that, due to the anisotropy of the material, a clamped square plate under uniaxial tension produces a sufficiently heterogeneous strain field. We hence consider a displacement-controlled uniaxial tension experiment of a square-shaped specimen that consists of $n_c \times n_c$ repeating square unit cells of the considered metamaterial (Fig. 2.2). At the fixed boundary of the specimen, a load cell measures the net reaction force. Further, the full-field deformation of the specimen is tracked through DIC, which measures the local displacements of the solid material. After preprocessing the data, the VFM takes as input the displacement measurements at the $(n_c + 1) \times (n_c + 1)$ unit cell corners and the net reaction forces. A quadrilateral finite element mesh is generated such that each of the $n_c \times n_c$ elements corresponds to one unit cell and the element nodes correspond to the unit cell corners with experimentally known displacement values. The continuous displacement field $\boldsymbol{u}(\boldsymbol{x})$ is hence approximated by

$$\boldsymbol{u}(\boldsymbol{x}) = \sum_{a=1}^{n_n} N^a(\boldsymbol{x})\boldsymbol{u}^a, \tag{4.1}$$

where $n_n = (n_c + 1)^2$ denotes the number of nodes in the finite element mesh and $\boldsymbol{u}^a$ are the known nodal displacements, while $N^a(\boldsymbol{x})$ are the standard ansatz functions of bilinear quadrilateral finite elements. The infinitesimal strain field is then obtained as the symmetric gradient of the displacement field, i.e., $\boldsymbol{\varepsilon}(\boldsymbol{x}) = \frac{1}{2}\left(\nabla\boldsymbol{u}(\boldsymbol{x}) + (\nabla\boldsymbol{u}(\boldsymbol{x}))^T\right)$.

---

kinematic data at the specimen boundary via DIC is known to be difficult.

Weak formulation of linear momentum balance

We denote the specimen domain and its boundary as Ω and $\partial\Omega$, respectively, and the surface traction force acting on $\partial\Omega$ as t. Assuming no inertia and body forces, the weak form of linear momentum balance reads

$$\int_\Omega \boldsymbol{\sigma}(\boldsymbol{x}) : \nabla \boldsymbol{v}(\boldsymbol{x}) \, \mathrm{d}A - \int_{\partial\Omega} \boldsymbol{t} \cdot \boldsymbol{v}(\boldsymbol{x}) \, \mathrm{d}s = 0, \tag{4.2}$$

which has to hold true for all admissible, i.e., sufficiently regular, test functions $\boldsymbol{v}(\boldsymbol{x})$. Note that we are not introducing the classical distinction between Dirichlet and Neumann portions of the boundary; accordingly, we are not requiring admissible test functions to vanish anywhere.

Discretization

The weak form of linear momentum balance has to hold true for any chosen set of admissible test functions. Here, we adopt the standard (Bubnov-Galerkin) approach and express the test functions as a linear combination of the same shape functions $N^a(\boldsymbol{x})$ used to interpolate the displacement data

$$\boldsymbol{v}(\boldsymbol{x}) = \sum_{a=1}^{n_n} N^a(\boldsymbol{x}) \boldsymbol{v}^a. \tag{4.3}$$

Inserting the test function ansatz into the weak form of linear momentum balance results in

$$\sum_{a=1}^{n_n} \boldsymbol{v}^a \cdot \left[\underbrace{\int_\Omega \boldsymbol{\sigma} \nabla N^a(\boldsymbol{x}) \, \mathrm{d}A}_{\boldsymbol{F}_{\text{int}}^a} - \underbrace{\int_{\partial\Omega} \boldsymbol{t} N^a(\boldsymbol{x}) \, \mathrm{d}S}_{\boldsymbol{F}_{\text{ext}}^a} \right] = 0, \tag{4.4}$$

where the first and second integral are the nodal internal forces $\boldsymbol{F}_{\text{int}}^a$ and nodal external forces $\boldsymbol{F}_{\text{ext}}^a$, respectively. By employing the constitutive relation Eq. (2.3), the nodal internal forces may be written as

$$\begin{aligned}
\boldsymbol{F}_{\text{int}}^a &= \int_\Omega \boldsymbol{\sigma} \nabla N^a \, \mathrm{d}A, \\
&= \int_\Omega \begin{bmatrix} \sigma_1 N_{,x}^a + \sigma_6 N_{,y}^a \\ \sigma_6 N_{,x}^a + \sigma_2 N_{,y}^a \end{bmatrix} \mathrm{d}A, \\
&= \int_\Omega \begin{bmatrix} C_{11}\varepsilon_1 N_{,x}^a + C_{12}\varepsilon_2 N_{,x}^a + 2C_{16}\varepsilon_6 N_{,x}^a + C_{16}\varepsilon_1 N_{,y}^a + C_{26}\varepsilon_2 N_{,y}^a + 2C_{66}\varepsilon_6 N_{,y}^a \\ C_{16}\varepsilon_1 N_{,x}^a + C_{26}\varepsilon_2 N_{,x}^a + 2C_{66}\varepsilon_6 N_{,x}^a + C_{12}\varepsilon_1 N_{,y}^a + C_{22}\varepsilon_2 N_{,y}^a + 2C_{26}\varepsilon_6 N_{,y}^a \end{bmatrix} \mathrm{d}A, \\
&= \int_\Omega \begin{bmatrix} \varepsilon_1 N_{,x}^a & \varepsilon_2 N_{,x}^a & 0 & 2\varepsilon_6 N_{,x}^a + \varepsilon_1 N_{,y}^a & \varepsilon_2 N_{,y}^a & 2\varepsilon_6 N_{,y}^a \\ 0 & \varepsilon_1 N_{,y}^a & \varepsilon_2 N_{,y}^a & \varepsilon_1 N_{,x}^a & \varepsilon_2 N_{,x}^a + 2\varepsilon_6 N_{,y}^a & 2\varepsilon_6 N_{,x}^a \end{bmatrix} \mathrm{d}A \, \boldsymbol{C}_{\text{vec}}, \tag{4.5}
\end{aligned}$$

where the elasticity tensor parameters $\boldsymbol{C}_{\text{vec}} = [C_{11} \; C_{12} \; C_{22} \; C_{16} \; C_{26} \; C_{66}]^T$ are assumed to be constant in space.

Choice of test functions

Choosing a test function in the form of (4.3) and evaluating (4.4) results in two linear equations with the material parameters as unknowns. As the weak linear momentum balance has to hold true for any test function this provides an infinite supply of linear equations. Hence, the problem at hand is overdetermined and different choices of test functions will yield different solutions for the unknown material parameters.

As discussed in Section 4.2, the deformation of a heterogeneous specimen and that of its homogenized counterpart under the same loading conditions are locally different, a phenomenon that is best observed at the boundary and at the corners of the specimen where local effects are especially pronounced. In the following, this special characteristic of the problem at hand motivates a special choice of the test functions that avoids evaluations of the linear momentum balance in the boundary regions of the specimen.

First, we define test functions that are constant at the nodes corresponding to one finite element, i.e., one unit cell, and zero at all other nodes. To this end, we define $C = \{1, \ldots, n_c^2\}$ as the set of all unit cells and $\mathcal{D}^c$ as the set of all nodes corresponding to the unit cell $c \in C$, and define a set of test functions as

$$\mathcal{V} = \left\{ \boldsymbol{v}(\boldsymbol{x}) = \frac{1}{n_{nc}} \sum_{a \in \mathcal{D}^c} N^a(\boldsymbol{x}) \boldsymbol{e}_i \mid c \in C, \ i \in \{1, 2\} \right\}, \tag{4.6}$$

where $\boldsymbol{e}_i$ are the unit vectors in the corresponding x- and y-direction. Note that the test functions are normalized by dividing by the number of nodes corresponding to the unit cell n_{nc} (equal to 4 in our case).

Using the test functions in $\mathcal{V}$ to test weak linear momentum balance would cause two problems. First, at elements adjacent to the loaded and to the restrained portions of the boundary, the external force contributions $\boldsymbol{F}^a_{\text{ext}}$ in (4.4) are unknown, leading to equations that could not be solved for the unknown material parameters. And second, we want to avoid using data at the specimen boundary due to the reasons discussed earlier. Therefore, we modify (4.6) such that

$$\mathcal{V}^{\text{int}} = \left\{ \boldsymbol{v}(\boldsymbol{x}) = \frac{1}{n_{nc}} \sum_{a \in \mathcal{D}^c} N^a(\boldsymbol{x}) \boldsymbol{e}_i \mid c \in C^{\text{int}}, \ i \in \{1, 2\} \right\}, \tag{4.7}$$

where $C^{\text{int}} \subset C$ denotes a reduced set of unit cells that does not include unit cells close to the boundary. We found that ignoring two rows of unit cells at the top and bottom boundary as well as two columns of unit cells at the left and right boundary are a good compromise, and we kept this choice constant throughout all tests. As the fields in $\mathcal{V}^{\text{int}}$ depend on $\boldsymbol{e}_i$, each field is zero in either x- or y-direction. The non-zero component of an exemplary virtual field in $\mathcal{V}^{\text{int}}$ is shown in Fig. 4.1 (left).

Evaluating Eq. (4.4) for this set of functions leads to

$$\frac{1}{n_{nc}} \sum_{a \in \mathcal{D}^c} \boldsymbol{F}_{\text{int}}^a = \boldsymbol{0}, \quad \forall c \in C^{\text{int}}. \tag{4.8}$$

Hence, this choice of virtual fields can be interpreted physically as enforcing that the sum of internal forces over one unit cell should vanish.
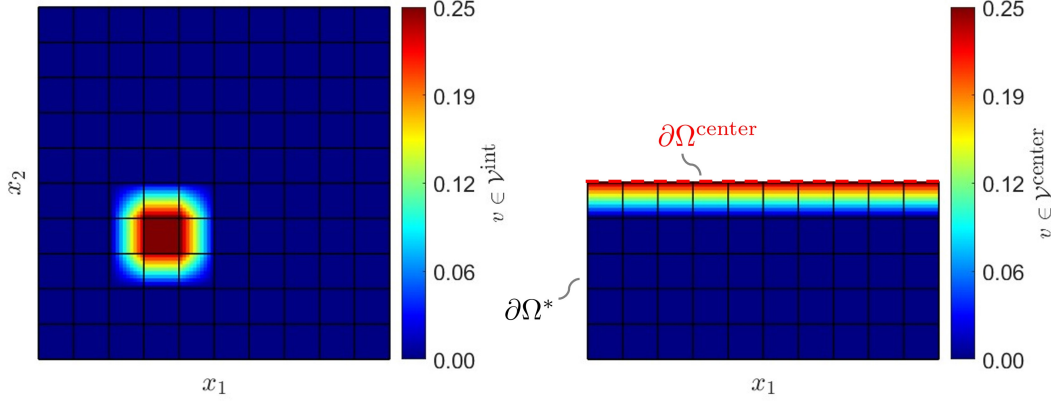
Figure 4.1: Non-zero component of a virtual field in $\mathcal{V}^{\text{int}}$ (left) and non-zero component of a virtual field in $\mathcal{V}^{\text{center}}$ (right).

Equations (4.8) are not sufficient to identify the unknown material parameters, as the trivial solution $\boldsymbol{C}_{\text{vec}} = \boldsymbol{0}$ fulfills (4.8). To obtain a well-posed problem, the measured reaction forces need to be incorporated. At the same time, we want to avoid using displacement data at the specimen boundary. Therefore, we consider the free-body diagram of the lower half of the domain as depicted in Fig. 4.1 (right). Denoting the half-body domain as $\Omega^* = \{\boldsymbol{x} \mid 0 \leq x_1 \leq L, \ 0 \leq x_2 \leq \frac{L}{2}\}$ and its boundary as $\partial\Omega^*$, the weak form of linear momentum balance for this domain reads

$$\int_{\Omega^*} \boldsymbol{\sigma}(\boldsymbol{x}) : \nabla \boldsymbol{v}(\boldsymbol{x}) \, \mathrm{d}A - \int_{\partial\Omega^*} \boldsymbol{t} \cdot \boldsymbol{v}(\boldsymbol{x}) \, \mathrm{d}s = 0. \tag{4.9}$$

Inserting the test function ansatz leads to

$$\sum_{a=1}^{n_n} \boldsymbol{v}^a \cdot \left[\underbrace{\int_{\Omega^*} \boldsymbol{\sigma} \nabla N^a(\boldsymbol{x}) \, \mathrm{d}A}_{\boldsymbol{F}_{\text{int}}^{*a}} - \underbrace{\int_{\partial\Omega^*} \boldsymbol{t} N^a(\boldsymbol{x}) \, \mathrm{d}S}_{\boldsymbol{F}_{\text{ext}}^{*a}} \right] = 0. \tag{4.10}$$

We define $\mathcal{D}^{\text{center}} = \{a \mid y^a = \frac{L}{2}\}$ as the set of nodes in the center of the specimen. If the tessellated geometry consists of an odd number of unit cells in each spatial direction, i.e., there are no nodes at

$y^a = \frac{L}{2}$, we consider instead $\mathcal{D}^{\text{center}} = \{a \mid y^a = \frac{L}{2} + \frac{L}{2n_c}\}$. We choose a set of virtual fields $\mathcal{V}^{\text{center}}$ that are constant along $\mathcal{D}^{\text{center}}$ and zero at all other nodes

$$\mathcal{V}^{\text{center}} = \left\{ \boldsymbol{v}(\boldsymbol{x}) = \frac{1}{n_{nc}} \sum_{a \in \mathcal{D}^{\text{center}}} N^a(\boldsymbol{x}) \boldsymbol{e}_i \mid i \in \{1, 2\} \right\}. \tag{4.11}$$

Evaluating (4.10) for these particularly chosen test functions results in

$$\sum_{a \in \mathcal{D}^{\text{center}}} \boldsymbol{F}_{\text{int}}^{*a} = \int_{\partial\Omega^{\text{center}}} \boldsymbol{t} \, \mathrm{d}S = \boldsymbol{R}, \tag{4.12}$$

where $\partial\Omega^{\text{center}}$ is the top boundary of Ω^*. Note that due to the specific choice of the test functions, the surface integral simplifies in such a way that it equals the global reaction force $\boldsymbol{R}$, meaning that the sum of the internal forces at $\partial\Omega^{\text{center}}$ must equal the net reaction force.

Deterministic parameter identification

After choosing the virtual fields and considering (4.5), the linear equations in (4.8) can be assembled in a system of equations

$$\boldsymbol{A}^{\text{int}} \boldsymbol{C}_{\text{vec}} = \boldsymbol{0}, \tag{4.13}$$

and the linear equations in (4.12) can be rewritten as

$$\boldsymbol{A}^{\text{center}} \boldsymbol{C}_{\text{vec}} = \boldsymbol{R}, \tag{4.14}$$

where $\boldsymbol{A}^{\text{int}}$ and $\boldsymbol{A}^{\text{center}}$ are in general non-symmetric matrices. The system formed by the linear equations (4.13) and (4.14) is overdetermined, i.e., it consists of more equations than unknown parameters. Assuming that the equations in the overdetermined system are not linearly dependent (which is a valid assumption as every equation is perturbed by noise when considering experimental data), there is no unique solution that satisfies all equations. Instead, we obtain an approximate solution of the overdetermined system by minimizing the sum of squared residuals

$$\boldsymbol{C}_{\text{vec}}^{\text{opt}} = \arg\min_{\boldsymbol{C}_{\text{vec}}} \left(\|\boldsymbol{A}^{\text{int}} \boldsymbol{C}_{\text{vec}}\|^2 + \lambda_r \|\boldsymbol{A}^{\text{center}} \boldsymbol{C}_{\text{vec}} - \boldsymbol{R}\|^2 \right), \tag{4.15}$$

where $\|\cdot\|$ is the Euclidean norm and $\lambda_r > 0$ is a weighting parameter that scales the different contributions to the minimization problem. As there are less equations in the system (4.14) than in (4.13), the weighting parameter should be chosen sufficiently larger than one ($\lambda_r >> 1$). Following previous works [116, 118, 120], we choose $\lambda_r = 100$ and keep it constant throughout this work. Based on our experience, the choice of λ_r is not crucial for the success of the method (see also [119, 122, 126]). The necessary condition for a minimum is

$$\bar{\boldsymbol{A}} \boldsymbol{C}_{\text{vec}}^{\text{opt}} = \bar{\boldsymbol{R}}, \qquad \text{with} \qquad \bar{\boldsymbol{A}} = \left(\boldsymbol{A}^{\text{int}}\right)^T \boldsymbol{A}^{\text{int}} + \lambda_r \left(\boldsymbol{A}^{\text{center}}\right)^T \boldsymbol{A}^{\text{center}}, \quad \bar{\boldsymbol{R}} = \lambda_r \left(\boldsymbol{A}^{\text{center}}\right)^T \boldsymbol{R}, \quad (4.16)$$

which leads to a determined system of equations that can be solved for $C_{\text{vec}}^{\text{opt}}$. The minimization problem in Eq. (4.15) can alternatively be written as

$$C_{\text{vec}}^{\text{opt}} = \arg \min_{C_{\text{vec}}} \|AC_{\text{vec}} - B\|^2, \tag{4.17}$$

where we have defined

$$A = \begin{bmatrix} A^{\text{int}} \\ \sqrt{\lambda_r} A^{\text{center}} \end{bmatrix}, \qquad B = \begin{bmatrix} 0 \\ \sqrt{\lambda_r} R \end{bmatrix}. \tag{4.18}$$

The necessary condition for a minimum then reads

$$A^T A C_{\text{vec}}^{\text{opt}} = A^T B. \tag{4.19}$$

Bayesian inference

Besides the previously introduced deterministic approach, we further study the problem from a stochastic perspective. To this end, we construct a Bayesian linear regression model, for which we assume no intercept and a diffuse prior, as implemented in the Matlab$^{\circledR}$ built-in function *bayeslm*.

We denote the number of rows in A as n_{eq} and we define A_i with $i \in \{1, \ldots, n_{eq}\}$ as the ith row of A. For each equation in the overdetermined system of equations $AC_{\text{vec}} = B$, we assume the likelihood of obtaining B_i as a Gaussian likelihood with mean $A_i \cdot C_{\text{vec}}$ and standard deviation $\sigma > 0$, i.e.,

$$p(B_i|A_i, C_{\text{vec}}, \sigma^2) = \frac{1}{\sqrt{2\pi\sigma^2}} \exp\left[-\frac{(B_i - A_i \cdot C_{\text{vec}})^2}{2\sigma^2}\right], \tag{4.20}$$

where C_{vec} and σ^2 are treated as random variables. Assuming further that the likelihoods are conditionally independent, we define the joint likelihood as

$$p(B|A, C_{\text{vec}}, \sigma^2) = \prod_{i=1}^{n_{eq}} p_i(B_i|A_i, C_{\text{vec}}, \sigma^2). \tag{4.21}$$

Assuming here a diffuse prior for the joint prior distribution of C_{vec} and σ^2, i.e.,

$$p(C_{\text{vec}}, \sigma^2) \propto \frac{1}{\sigma^2}, \tag{4.22}$$

the marginal posterior distributions of C_{vec} and σ^2 are analytically tractable and implemented in the Matlab$^{\circledR}$ function *bayeslm*.

4.3 Parameter identification based on multiple tests

In this section, we explore a method of parameter identification that involves multiple tests (as in the conventional approach) in the context of anisotropic metamaterials.

Parameter identification with multiple tests without unit cell rotation

We subject the metamaterial to three different tests namely *Test A*, *Test B*, and *Test C* as shown in Fig. 4.2. *Test A* and *Test C* are tension tests along x_2 and x_1 axis respectively, and *Test B* is a simple shear test. We assume that the average strains $\tilde{\varepsilon}_{ij}^{A,B,C}$ are known experimentally from full-field measurements. In addition, the reaction forces at the fixed end are known experimentally from load sensor measurements. We will show that the material parameters can be identified from the average strains and the net reaction forces from these three tests.

From Gauss' divergence theorem, the average stresses $\tilde{\sigma}$ are related to the tractions t at the fixed end as

$$t_i = \tilde{\sigma}_{ij}n_j, \tag{4.23}$$

where n is the unit outward normal. For *Test A*, the unit outward normal n at the fixed end is $[0, -1]^T$. Using Eqs. (2.3) and (4.23), and assuming homogenized effective continuum behavior for the structured solid, we get

$$F_1^A/\mathcal{A} = \tilde{\sigma}_6^A = C_{16}\tilde{\varepsilon}_{11}^A + C_{26}\tilde{\varepsilon}_2^A + C_{66}\left(2\tilde{\varepsilon}_6^A\right), \tag{4.24a}$$

$$F_2^A/\mathcal{A} = \tilde{\sigma}_2^A = C_{12}\tilde{\varepsilon}_1^A + C_{22}\tilde{\varepsilon}_2^A + C_{26}\left(2\tilde{\varepsilon}_6^A\right), \tag{4.24b}$$

where $\tilde{\sigma}_{12}^A, \tilde{\sigma}_{22}^A$ are the average stress components, F_1^A, F_2^A are the reaction force components at the fixed end from *Test A* and $\mathcal{A}$ is the cross sectional area of the fixed end.

Similarly, from *Test B* and *Test C*, we get

$$F_1^B/\mathcal{A} = \tilde{\sigma}_6^B = C_{16}\tilde{\varepsilon}_1^B + C_{26}\tilde{\varepsilon}_2^B + C_{66}\left(2\tilde{\varepsilon}_6^B\right), \tag{4.25a}$$

$$F_2^B/\mathcal{A} = \tilde{\sigma}_2^B = C_{12}\tilde{\varepsilon}_1^B + C_{22}\tilde{\varepsilon}_2^B + C_{26}\left(2\tilde{\varepsilon}_6^B\right), \tag{4.25b}$$

$$F_1^C/\mathcal{A} = \tilde{\sigma}_1^C = C_{11}\tilde{\varepsilon}_1^C + C_{12}\tilde{\varepsilon}_2^C + C_{16}\left(2\tilde{\varepsilon}_6^C\right), \tag{4.25c}$$

$$F_2^C/\mathcal{A} = \tilde{\sigma}_6^C = C_{16}\tilde{\varepsilon}_1^C + C_{26}\tilde{\varepsilon}_2^C + C_{66}\left(2\tilde{\varepsilon}_6^C\right). \tag{4.25d}$$

Rearranging Eqs. (4.24a), (4.24b) and (4.25a) to (4.25d) into a matrix form, we obtain a system of linear equations,

$$\begin{bmatrix} 0 & 0 & 2\tilde{\varepsilon}_6^A & \tilde{\varepsilon}_1^A & \tilde{\varepsilon}_2^A & 0 \\ 0 & \tilde{\varepsilon}_2^A & 0 & 0 & 2\tilde{\varepsilon}_6^A & \tilde{\varepsilon}_1^A \\ 0 & 0 & 2\tilde{\varepsilon}_6^B & \tilde{\varepsilon}_1^B & \tilde{\varepsilon}_2^B & 0 \\ 0 & \tilde{\varepsilon}_2^B & 0 & 0 & 2\tilde{\varepsilon}_6^B & \tilde{\varepsilon}_1^B \\ \tilde{\varepsilon}_1^C & 0 & 0 & 2\tilde{\varepsilon}_6^C & 0 & \tilde{\varepsilon}_2^C \\ 0 & 0 & 2\tilde{\varepsilon}_6^C & \tilde{\varepsilon}_1^C & \tilde{\varepsilon}_2 & 0 \end{bmatrix} \begin{bmatrix} C_{11} \\ C_{22} \\ C_{66} \\ C_{16} \\ C_{26} \\ C_{12} \end{bmatrix} = \frac{1}{\mathcal{A}} \begin{bmatrix} F_1^A \\ F_2^A \\ F_1^B \\ F_2^B \\ F_1^C \\ F_2^C \end{bmatrix}. \tag{4.26}$$

For readability, Eq. (4.26) is written as

$$\mathcal{A}\tilde{\boldsymbol{\varepsilon}}\boldsymbol{C}_{\text{vec}} = \boldsymbol{F}_{\text{vec}}, \tag{4.27}$$

where $\tilde{\boldsymbol{\varepsilon}}$ is a non-symmetric square matrix of size 6 containing average strain components from all of the tests and $\boldsymbol{F}_{\text{vec}}$ is a vector containing net reaction force components from all of the tests. Then the material parameters $\boldsymbol{C}_{\text{vec}}^{\text{opt}}$ can be obtained as a solution to the least squares minimization problem,

$$\boldsymbol{C}_{\text{vec}}^{\text{opt}} = \arg\min_{\boldsymbol{C}_{\text{vec}}} \|\mathcal{A}\tilde{\boldsymbol{\varepsilon}}\boldsymbol{C}_{\text{vec}} - \boldsymbol{F}_{\text{vec}}\|^2. \tag{4.28}$$

It should be noted that we use this method for material parameter identification, only using the numerical data. We did not experimentally validate this method, since shear testing is non-trivial and requires dedicated setups, such as a hexapod machine [141].
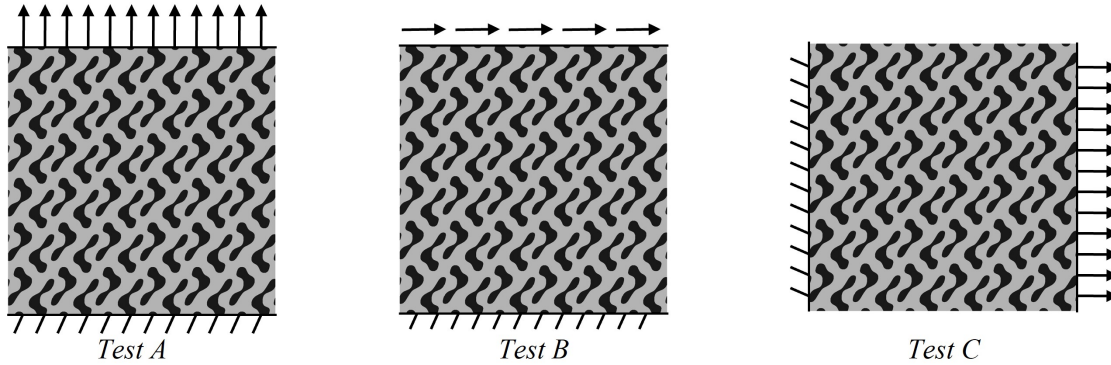
Figure 4.2: Parameter identification of an anisotropic metamaterial by performing three different tests.

Parameter identification with rotation of frame of reference

To avoid applying shear displacement and limit the testing to a single boundary condition type (like tension), we try to rotate the unit cell instead. For this we reorient the unit cell topology along a new coordinate system. This transforms the stiffness tensor components into different coordinate frame of reference while keeping the testing setup constant.

We subject the structures constructed by tessellating unit cells oriented at different angles as shown in Fig. 4.3. We tested $\{0°, 45°, 135°\}$, and $\{0°, 45°, 90°\}$ combinations of unit cell rotation angles. We pick the first set as it yielded better results.

Using, Eq. (2.8), the components of the stiffness tensor when the unit cell is rotated by 90° are given by,

$$C^{90°} = \begin{bmatrix} C_{22} & C_{12} & -C_{26} \\ C_{12} & C_{11} & -C_{16} \\ -C_{26} & -C_{16} & C_{66} \end{bmatrix}. \tag{4.29}$$

The components of the stiffness tensor when the unit cell is rotated by 45° are given by,

$$C^{45°} = \begin{bmatrix} \frac{C_{11}}{4} + \frac{C_{12}}{2} + C_{16} + \frac{C_{22}}{4} + C_{26} + C_{66} & \frac{C_{11}}{4} + \frac{C_{12}}{2} + \frac{C_{22}}{4} - C_{66} & \frac{C_{22}}{4} - \frac{C_{16}}{2} - \frac{C_{11}}{4} + \frac{C_{26}}{2} \\ \frac{C_{11}}{4} + \frac{C_{12}}{2} + \frac{C_{22}}{4} - C_{66} & \frac{C_{11}}{4} + \frac{C_{12}}{2} - C_{16} + \frac{C_{22}}{4} - C_{26} + C_{66} & \frac{C_{16}}{2} - \frac{C_{11}}{4} + \frac{C_{22}}{4} - \frac{C_{26}}{2} \\ \frac{C_{22}}{4} - \frac{C_{16}}{2} - \frac{C_{11}}{4} + \frac{C_{26}}{2} & \frac{C_{16}}{2} - \frac{C_{11}}{4} + \frac{C_{22}}{4} - \frac{C_{26}}{2} & \frac{C_{11}}{4} - \frac{C_{12}}{2} + \frac{C_{22}}{4} \end{bmatrix}. \tag{4.30}$$

Similarly, the components of the stiffness tensor when the unit cell is rotated by 135° are given by

$$C^{135°} = \begin{bmatrix} \frac{C_{11}}{4} + \frac{C_{12}}{2} - C_{16} + \frac{C_{22}}{4} - C_{26} + C_{66} & \frac{C_{11}}{4} + \frac{C_{12}}{2} + \frac{C_{22}}{4} - C_{66} & \frac{C_{11}}{4} - \frac{C_{16}}{2} - \frac{C_{22}}{4} + \frac{C_{26}}{2} \\ \frac{C_{11}}{4} + \frac{C_{12}}{2} + \frac{C_{22}}{4} - C_{66} & \frac{C_{11}}{4} + \frac{C_{12}}{2} + C_{16} + \frac{C_{22}}{4} + C_{26} + C_{66} & \frac{C_{11}}{4} + \frac{C_{16}}{2} - \frac{C_{22}}{4} - \frac{C_{26}}{2} \\ \frac{C_{11}}{4} - \frac{C_{16}}{2} - \frac{C_{22}}{4} + \frac{C_{26}}{2} & \frac{C_{11}}{4} + \frac{C_{16}}{2} - \frac{C_{22}}{4} - \frac{C_{26}}{2} & \frac{C_{11}}{4} - \frac{C_{12}}{2} + \frac{C_{22}}{4} \end{bmatrix}. \tag{4.31}$$

We construct a system of linear equations by equating average strains with the effective tensors from these different orientations as,

$$\begin{bmatrix} 0 & 0 & 2\tilde{\varepsilon}_{12}^A & \tilde{\varepsilon}_{11}^A & \tilde{\varepsilon}_{22}^A & 0 \\ 0 & \tilde{\varepsilon}_{22}^A & 0 & 0 & 2\tilde{\varepsilon}_{12}^A & \tilde{\varepsilon}_{11}^A \\ \frac{\tilde{\varepsilon}_{11}^B + \tilde{\varepsilon}_{22}^B + 2\tilde{\varepsilon}_{12}^B}{4} & \frac{-\tilde{\varepsilon}_{11}^B - \tilde{\varepsilon}_{22}^B + 2\tilde{\varepsilon}_{12}^B}{4} & 0 & \frac{-2\tilde{\varepsilon}_{11}^B + 2\tilde{\varepsilon}_{22}^B}{4} & \frac{2\tilde{\varepsilon}_{11}^B - 2\tilde{\varepsilon}_{22}^B}{4} & -\tilde{\varepsilon}_{12}^B \\ \frac{\tilde{\varepsilon}_{11}^B + \tilde{\varepsilon}_{22}^B + 2\tilde{\varepsilon}_{12}^B}{4} & \frac{\tilde{\varepsilon}_{11}^B + \tilde{\varepsilon}_{22}^B - 2\tilde{\varepsilon}_{12}^B}{4} & -\tilde{\varepsilon}_{11}^B + \tilde{\varepsilon}_{22}^B & \frac{2\tilde{\varepsilon}_{22}^B + 2\tilde{\varepsilon}_{12}^B}{4} & \frac{2\tilde{\varepsilon}_{22}^B - 2\tilde{\varepsilon}_{12}^B}{4} & \frac{2\tilde{\varepsilon}_{11}^B + 2\tilde{\varepsilon}_{22}^B}{4} \\ 0 & 0 & 2\tilde{\varepsilon}_{12}^C & -\tilde{\varepsilon}_{22}^C & \tilde{\varepsilon}_{11}^C & 0 \\ \tilde{\varepsilon}_{22}^C & 0 & 0 & -2\tilde{\varepsilon}_{12}^C & 0 & \tilde{\varepsilon}_{11}^C \end{bmatrix} \begin{bmatrix} C_{11} \\ C_{22} \\ C_{66} \\ C_{16} \\ C_{26} \\ C_{12} \end{bmatrix} = \frac{1}{L} \begin{bmatrix} F_1^A \\ F_2^A \\ F_1^B \\ F_2^B \\ F_1^C \\ F_2^C \end{bmatrix}. \tag{4.32}$$

It is important to note that, while theoretically all angles are possible, not all rotation angles guarantee periodicity when we perform rotations of unit cells on a finite-sized structure instead of a continuum sample, see Fig. 4.4. The system of linear equations Eq. (4.32) are solved to obtain the material parameters.

Although a complicated shear test is avoided in this method, three different testing specimens need to be manufactured. Hence we do not consider both of these methods that involve multiple tests for the experimental validation.

Test A
$0°$

Test B
$45°$

Test C
$90°$
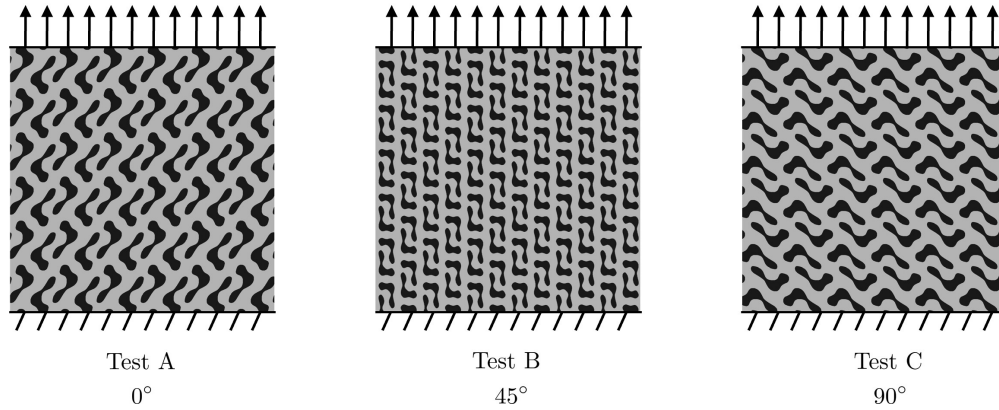
Figure 4.3: Material parameter identification by subjecting the structured solid to three different tension tests by changing the orientation of the unit cell.
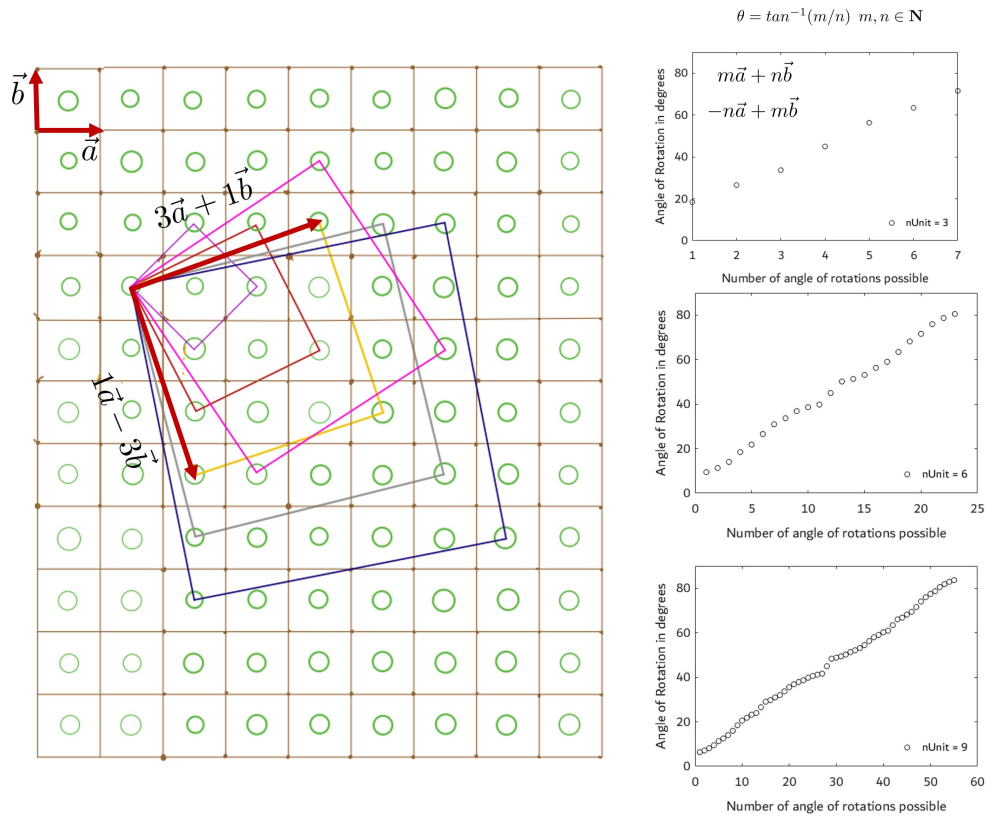
Figure 4.4: Possible rotation angles that ensure periodicity change as the number of unit cells in the tessellation increase. Highlighted squares in the left figure show some of the orientations in which periodicity is ensured.

4.4 Choice of unit cell geometries for experimental validation

We pick four unit cells with distinct/diverse effective stiffness tensor parameters (all with six non-zero stiffness parameters). Table 4.1 shows the unit cells along with their symmetry class and homogenized stiffness tensor. Geometry #1 has C_{22} as the largest stiffness parameter with C_{16} almost comparable to C_{12} and $C_{26} > C_{16}$. While geometry #2 has C_{11} as the largest stiffness parameter with $C_{16} > C_{26}$, geometry #3 has negative values for all of the off-diagonal parameters. Geometry #4 has four independent stiffness parameters with C_{66} as one of the largest values among other stiffness parameters, along with $C_{11} = C_{22}$ and $C_{16} = C_{26}$. The fill fraction of the stiff phase for all the unit cells lies between 60 and 70 %. Further, 10×10 tessellation of all the four geometries are shown in Fig. 4.5. It can be observed that all the structures are periodic and the stiff-phase is connected all throughout suitable for single material additive manufacturing.

Unit Cell Geometry	Name	Homogenized Stiffness Tensor (C^{H}) [MPa]	Elastic Symmetry Class
	Geometry #1	$\begin{bmatrix} 131.62 & 61.98 & 63.58 \\ 61.98 & 198.38 & 83.87 \\ 63.58 & 83.87 & 95.30 \end{bmatrix}$	Z_2
	Geometry #2	$\begin{bmatrix} 127.14 & 59.50 & 73.42 \\ 59.50 & 105.83 & 55.16 \\ 73.42 & 55.16 & 110.15 \end{bmatrix}$	Z_2
	Geometry #3	$\begin{bmatrix} 44.70 & -9.42 & -12.52 \\ -9.42 & 107.19 & -20.71 \\ -12.52 & -20.71 & 105.35 \end{bmatrix}$	Z_2
	Geometry #4	$\begin{bmatrix} 65.74 & 40.36 & 18.95 \\ 40.36 & 65.74 & 18.95 \\ 18.95 & 18.95 & 86.47 \end{bmatrix}$	D_2

Table 4.1: Unit cell geometries considered in this study along with their mechanical and symmetry properties.

Further, in Fig. 4.6, the role of mesh density (or the number of pixels) in affecting the effective properties is studied from a mesh convergence perspective. As mentioned in Section 2.3, the pixel density of the function is altered to generate unit cells with increasing pixel density from 100 to 300 with an increment of 20. The results show that parameters increase as the pixel density is increased, however, the change is not substantial ($\approx$ 1 MPa) in all the parameters. Similar trends hold true for the rest of the three geometries.
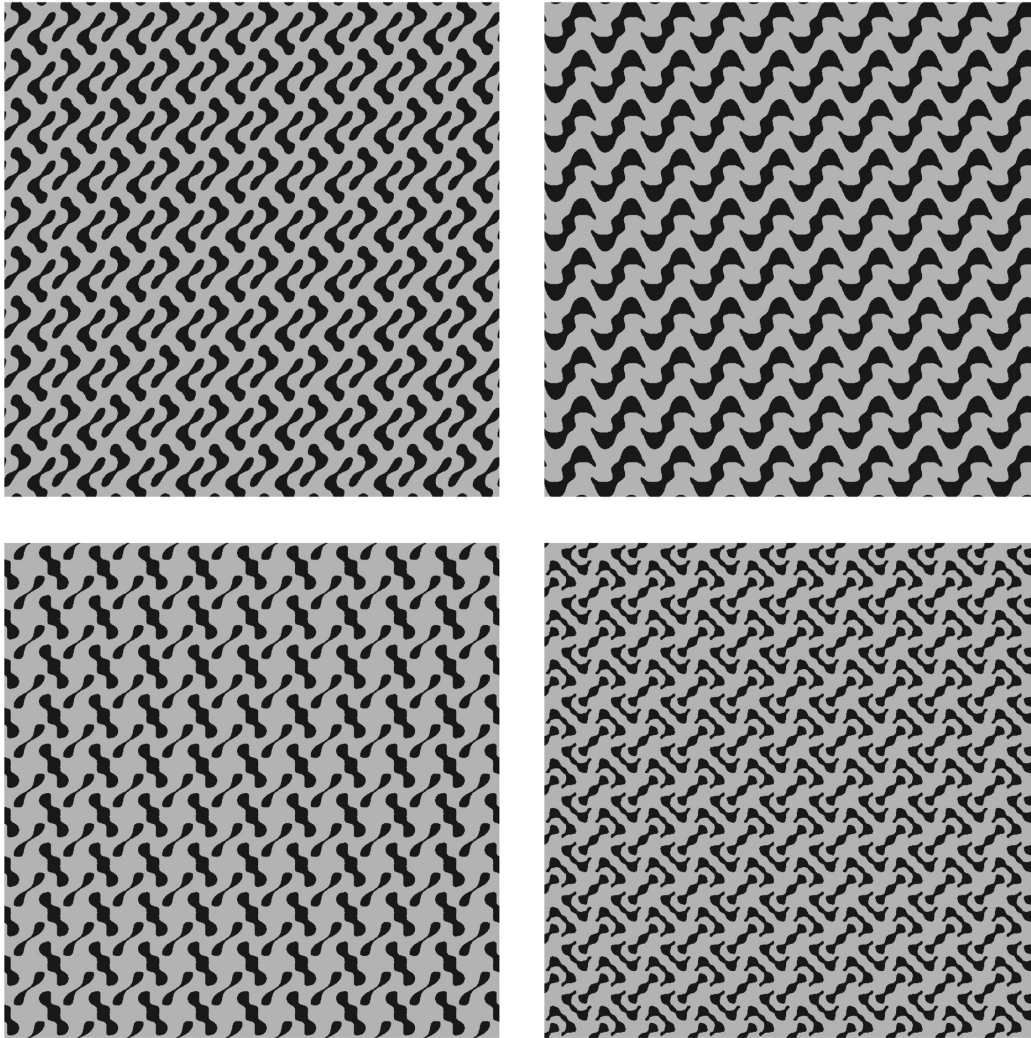
Figure 4.5: 10×10 tessellation of all the four geometries considered in for experimental validation of the effective properties estimated by homogenization theory.

4.5   Results and discussion

In this section, we discuss the data generation from both numerical simulations and experiments. Afterward, we apply the proposed deterministic parameter identification method based on VFM and multiple test to the data and discuss the results. Finally, at the end of the section, we apply the Bayesian method to the data in the context of VFM.
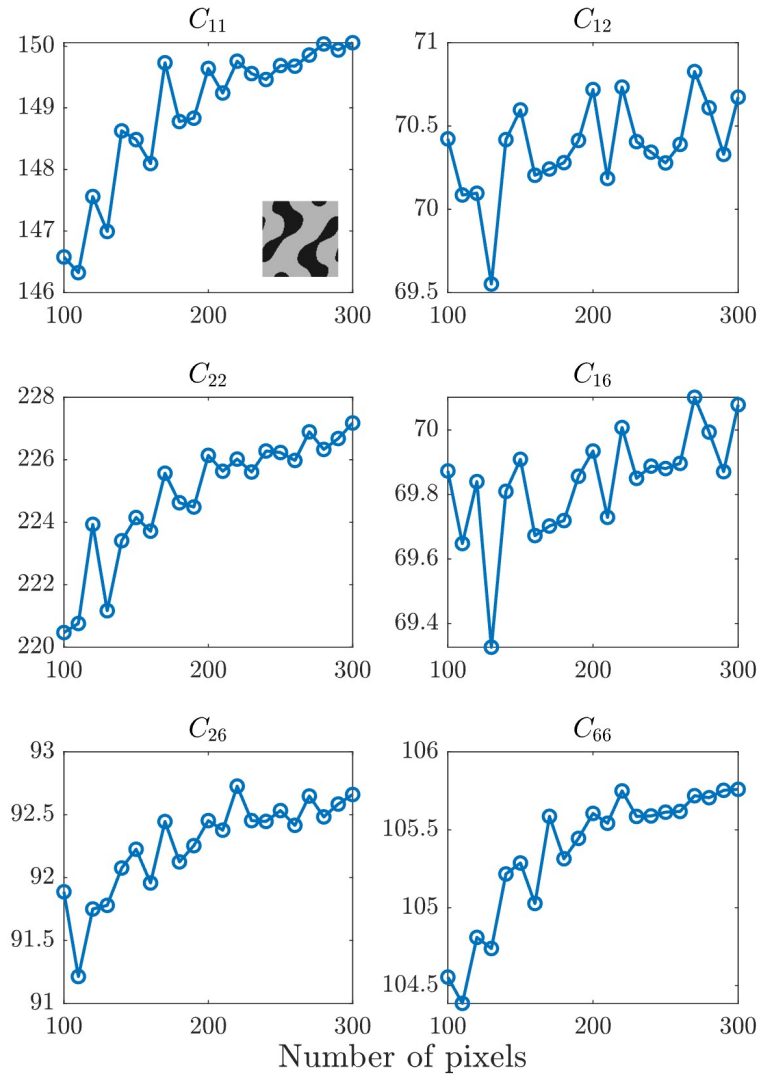
Figure 4.6: Effect of number of pixels on the effective properties of the geometry #1. Pixel density played a minimal role in the effective properties beyond the chosen pixel density of 100.

Generation of full-field displacement data

In the following, we investigate the synthetically generated displacement data for a heterogeneous structure in comparison to the computed displacement field of a homogeneous body, whose stiffness is equal to the homogenized stiffness of the heterogeneous structure. To simulate the displacement of a homogeneous body, we assume a 10×10 bilinear quadrilateral finite element mesh. The displacement of the heterogeneous body is computed on a much finer mesh with 1000×1000 elements. To allow for a comparison with the displacement field of the homogeneous body, the

computed displacements at the unit cell corners of the heterogeneous body (i.e., the data of interest for the VFM) are extracted and interpolated with a bilinear polynomial for each unit cell. It can be seen in Fig. 4.7 that there is a good qualitative agreement between the two displacement fields for geometry #1 (see Fig. 4.14, Fig. 4.15, and Fig. 4.16 for the other geometries). However, there are quantitative differences due to local effects in the heterogeneous structure, which appear to be dominant at the boundary and corners of the specimen.
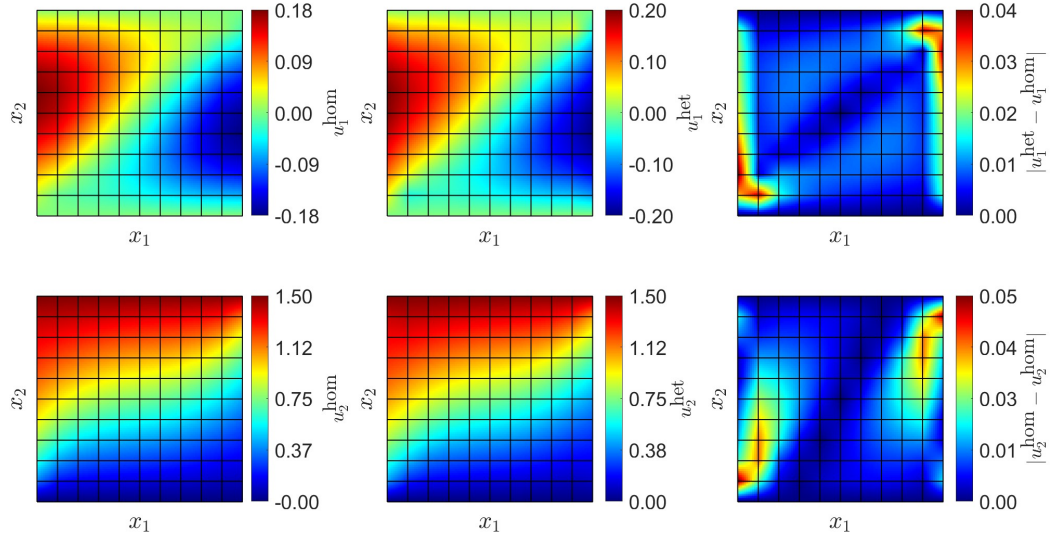
Figure 4.7: Comparison between the displacement fields obtained from finite element simulations of a homogeneous specimen (left) and a heterogeneous structure made of geometry #1 (center). For the homogeneous specimen a finite element simulation using 10×10 bilinear quadrilateral elements was executed. The heterogeneous specimen was simulated using 1000×1000 bilinear quadrilateral elements. Afterwards, the displacement data at the unit cell corners were extracted and interpolated with a bilinear polynomial for each unit cell, to allow for a comparison with the homogeneous specimen. The difference between the fields is shown on the right.

Comparison between experimental and synthetic data

In Fig. 4.8, we compare the full-field displacement and strain fields between the numerical and experimental data on the heterogeneous structure for geometry #1. (See Figs. 4.17 to 4.19 for the other geometries). We observe very good agreement between the numerical and experimental data, especially for the variables u_2, ε_{22}. However, the experimentally measured u_1 appears to be slightly higher than the numerical data, by about 0.1 mm, for all the geometries. Also the two ε_{11} fields are in good qualitative agreement, but experimental strains are larger. As expected, most of the strain is localized in the softer phase, although the applied global strain ($\tilde{\varepsilon}_{22}$) is 0.02. This causes

the deformations in the soft phase deformations to enter the nonlinear regime, which is a deviation from our linear elasticity assumption. This discrepancy introduces a source of error in the final experimentally measured parameters.
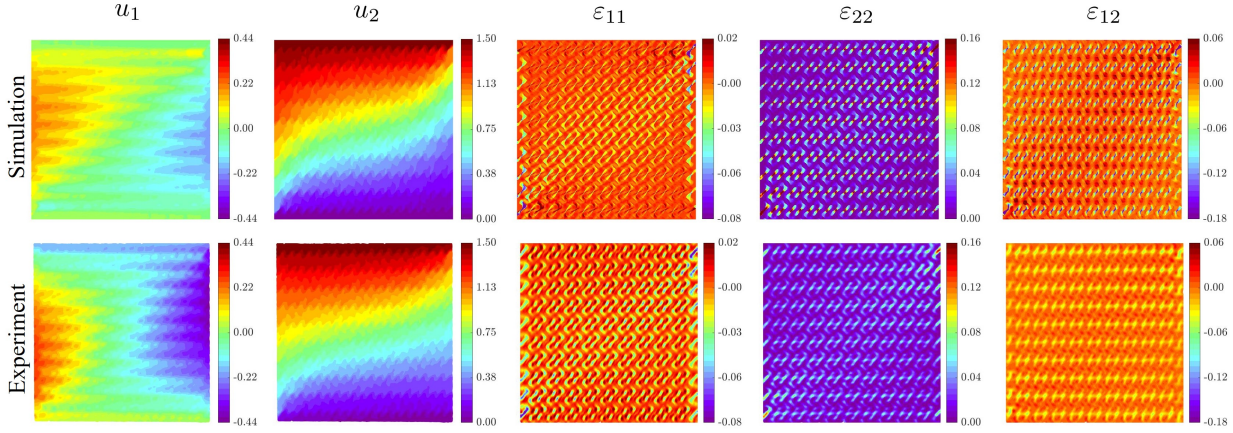
Figure 4.8: Comparison between numerical (top) and experimentally measured (bottom) full-field displacement and strain field data for the 10 unit cell tessellation of geometry #1 subjected to displacement-controlled uniaxial tension test.

Further, a comparison of the displacement fields after postprocessing the synthetic and experimental data, i.e., after extracting and interpolating the displacements at the unit cell corners for all the geometries are shown in Fig. 4.20, Fig. 4.21, Fig. 4.22, and Fig. 4.23. All displacements are in good agreement. An exception is observed for geometry #3 (see Fig. 4.18 and Fig. 4.22), for which the experimentally measured horizontal displacement u_1 does not compare well to the corresponding finite element results. The unit cell architecture of geometry #3 leads to highly nonlinear mechanical behavior (see Fig. 4.13), which is not captured well in the simulations.

Parameter identification based on synthetic data

Since the homogenization theory assumes length scale separation and periodic boundary conditions in identifying the effective material parameters, it is important to understand the continuum behavior of the heterogeneous structures as the number of unit cells changes. For this, we apply the VFM described in Section 4.2 on the synthetic data to identify material parameters as the number of unit cells in each direction are varied simultaneously. Further, we also use synthetic data to identify parameters using multiple tests (as in the conventional approach). A discussion on this conventional approach is provided in 4.3. The relative error is defined as

$$\text{LSE}_{\|\cdot\|_2} = \frac{\left\|\boldsymbol{C}_{\text{vec}}^{\text{H}} - \boldsymbol{C}_{\text{vec}}^{\text{M}}\right\|_2}{\left\|\boldsymbol{C}_{\text{vec}}^{\text{H}}\right\|_2} \quad \text{with } \boldsymbol{C}_{\text{vec}} \in \mathbb{R}^6, \tag{4.33}$$

where $\boldsymbol{C}_{\text{vec}}^{\text{H}}$ is the vectorized homogenized stiffness tensor obtained from computational homogenization and $\boldsymbol{C}_{\text{vec}}^{\text{M}}$ is the vectorized stiffness tensor identified using the VFM and the conventional methods.

We compare the relative error in parameter identification when performing multiple tests (as in the conventional approach) and when using the VFM (Fig. 4.9). Since we exclude two rows and columns of boundary unit cells in the proposed VFM, the number of unit cells available to form the system of equations is guaranteed only when there are at least 7 unit cells in each direction and the results are shown starting with this number. For geometry #1, as the number of unit cells increases, the error calculated for the conventional method based on multiple tests decreases monotonically from 13.4% at 5 unit cell tessellation to 2.3% at 25 unit cell tessellation. Similarly, the error for the VFM decreases monotonically from 13.1% at 7 unit cell tessellation to 2.4% at 25 unit cell tessellation. This shows that the parameters identified using our VFM are as good as those obtained by performing multiple tests, as long as there are at least ten repeated unit cells in the domain of interest. We found this general conclusion to hold for most of the considered geometries. The only exception is geometry #3, for which the error remains at 7.0% (for multiple tests) and 11.8% (for the VFM) even beyond 10 unit cell tessellation. The comparatively large relative error, however, does not mean that all material parameters are inaccurately identified. By taking a closer look at the individual components of the stiffness tensor, it is observed that many of the parameters are identified with satisfactory accuracy. We show in Figs. 4.24 and 4.25 in the Supplementary Information the convergence behavior of all individual parameters for geometry #1 and geometry #3 as the number of unit cells for tessellation is varied, where we excluded the other geometries for brevity. While for geometry #1 all parameters are satisfactorily identified, in the case of geometry #3 a major portion of the error lies in just two of the parameters, i.e., C_{12} for multiple tests and C_{16} and C_{66} for the VFM. Parameters C_{12} and C_{16} are quite small relative to the rest of the parameters and hence, they are hard to accurately estimate in comparison to the others. It can further be observed in Figs. 4.24 and 4.25 that for some of the parameters, the method of multiple tests outperforms the VFM, but for other parameters the VFM is superior. These results indicate that the parameters for geometry #3 are difficult to identify independently of the choice of the parameter identification method.

As the number of unit cells increases, the ratio of the number of unit cells along the boundary to the number of unit cells in the interior decreases. As a result, the boundary effects described in Section 4.5 diminish and the behavior of the structure approaches the continuum equivalent. In Table 4.2, we summarize the parameters identified for geometry #1 from both the methods against homogenization for 25 unit cell tessellation (see Table 4.3, Table 4.4, Table 4.5 for the other geometries). We also perform by changing the discretization elements in the unit cell, the
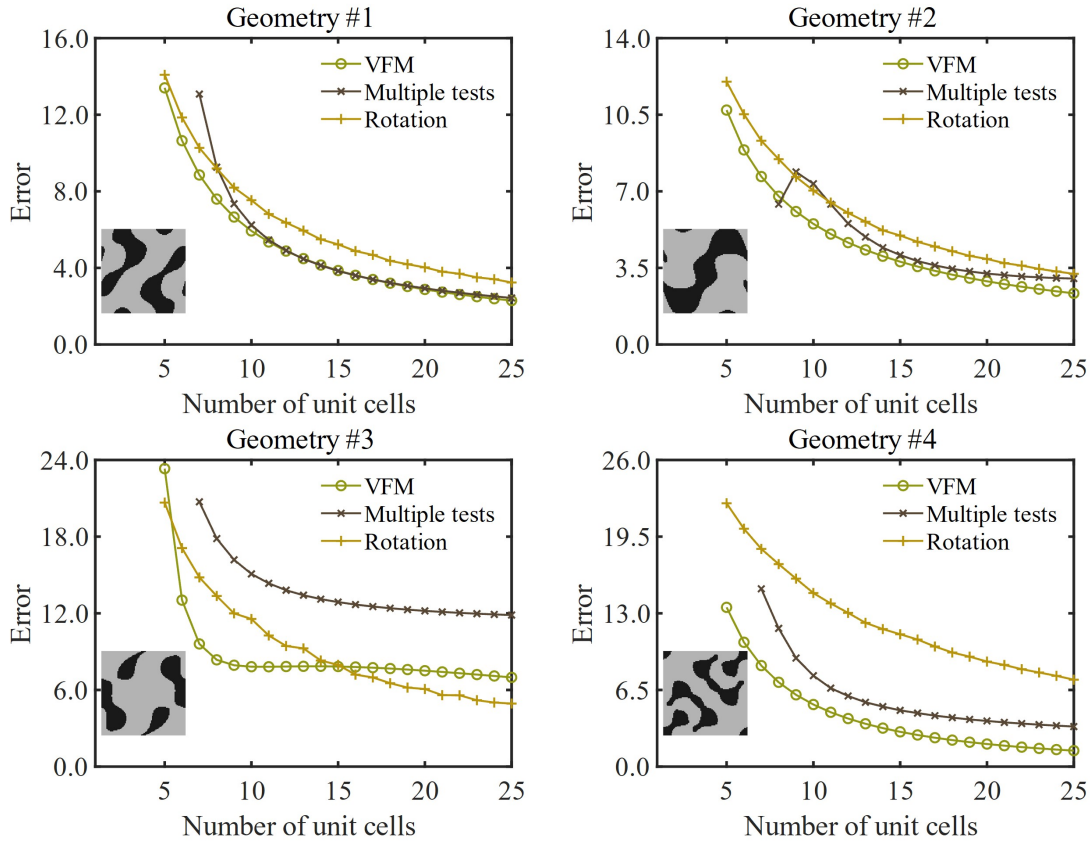
Figure 4.9: Variation of least square error between homogenized stiffness tensor and stiffness tensor identified using the VFM and the conventional methods as the number of unit cells in each direction are varied.

results of which are shown in Table 4.6. For a fixed 10×10 tessellation, mesh convergence is studied by varying the RVE size between 50 to 300 pixels for the tension test. Mesh convergence is estimated through reaction forces in the whole structure, minimum and maximum values for U_1 displacements, and average strains in the stiff phase. The following table summarizes [min max] for U1, strains, and reaction forces. The results indicate that an RVE size of 100 pixels is good enough to capture all the details.

Method	C_{11} (MPa)	C_{12} (MPa)	C_{22} (MPa)	C_{16} (MPa)	C_{26} (MPa)	C_{66} (MPa)
Homogenization	131.62	61.98	198.38	63.58	83.87	95.30
VFM	125.97	62.57	196.15	61.35	82.39	93.48
Multiple tests	129.86	67.93	199.37	64.01	85.47	95.54

Table 4.2: Comparison of stiffness tensor parameters identified for geometry #1 with 25 unit cell tessellation based on synthetic data using the VFM and the conventional methods against the computational homogenization.

Method	C_{11} (MPa)	C_{12} (MPa)	C_{22} (MPa)	C_{16} (MPa)	C_{26} (MPa)	C_{66} (MPa)
Homogenization	127.14	59.50	105.83	73.42	55.16	110.15
VFM	129.92	58.84	102.72	77.43	55.25	113.73
Multiple tests	123.82	57.44	102.35	72.74	54.68	110.12

Table 4.3: Comparison of stiffness tensor parameters identified for geometry #2 with 25 unit cell tessellation based on synthetic data using the VFM and the conventional methods against the computational homogenization.

Method	C_{11} (MPa)	C_{12} (MPa)	C_{22} (MPa)	C_{16} (MPa)	C_{26} (MPa)	C_{66} (MPa)
Homogenization	44.70	-9.42	107.19	-12.52	-20.71	105.35
VFM	33.95	-5.84	106.48	-4.44	-20.78	92.65
Multiple tests	45.78	-19.27	112.01	-11.30	-20.30	105.65

Table 4.4: Comparison of stiffness tensor parameters identified for geometry #3 with 25 unit cell tessellation based on synthetic data using the VFM and the conventional methods against the computational homogenization.

Method	C_{11} (MPa)	C_{12} (MPa)	C_{22} (MPa)	C_{16} (MPa)	C_{26} (MPa)	C_{66} (MPa)
Homogenization	65.74	40.36	65.74	18.95	18.95	86.47
VFM	65.45	40.94	65.43	17.93	17.76	82.19
Multiple tests	66.66	41.58	66.66	18.75	18.75	86.86

Table 4.5: Comparison of stiffness tensor parameters identified for geometry #4 with 25 unit cell tessellation based on synthetic data using the VFM and the conventional methods against the computational homogenization.

Size	Nodes	U_1 (mm)	ε_1 (max)	ε_2 (max)	ε_6 (max)	F_x (N)	$F_y(N)$
50	251001	0.2195	0.0402	0.0402	0.1303	185	668
100	1002001	0.2251	0.0252	0.0716	0.0792	192	704
150	2253001	0.2440	0.0190	0.0515	0.0570	193	718
200	4004001	0.2227	0.0146	0.0415	0.0418	194	727
300	9006001	0.2217	0.0106	0.0280	0.0288	195	730

Table 4.6: Mesh convergence study for a structured material made with 10×10 tessellation. The unit cell discretization is increased from 50 pixels to 300 pixels along one axis. There is a strong convergence in the displacement and force quantities, which are crucial for this analysis.

Parameter identification based on experimental data

Fig. 4.10 summarizes the material parameters identified by the VFM using the simulated and experimental data for 10 unit cell tessellations in comparison to the homogenized stiffness. The parameters identified using synthetic data compare well with the homogenized properties for all the geometries. Further, a good qualitative agreement is observed for the parameters identified using experimental data. For some of the parameters, such as $C_{12}, C_{22}, C_{16}, C_{26}$, the experimentally

determined parameters match the expectations quantitatively. In contrast, there is a larger discrepancy in the values of C_{11}, C_{66}, for almost all the geometries. These discrepancies are related to the fact that the experimentally measured displacement u_1 appears higher than in the simulations, i.e., about 0.1 mm, leading to an under-prediction of the stiffness in the lateral directions. An interesting observation is made for geometry #4. Based on the numerical data, we know that $C_{11} = C_{22}$ and $C_{16} = C_{26}$. However, we observe experimentally that $C_{11} < C_{22}$ and $C_{16} < C_{26}$. Geometry #3 has thin and sharp features in the softer phase. The presence of these sharp features inducing local stress singularities likely led to local material damage, which was subsequently observed as non-linear load-displacement behavior (see Fig. 4.13). As it is well known, the behavior of materials in the vicinity of such sharp discontinuities markedly deviates from a two-dimensional linear elastic continuum [142]. Therefore, we attribute such non-linear behavior to the architecture of geometry #3 itself. In such micro-structures, our linear elastic model assumption fails.
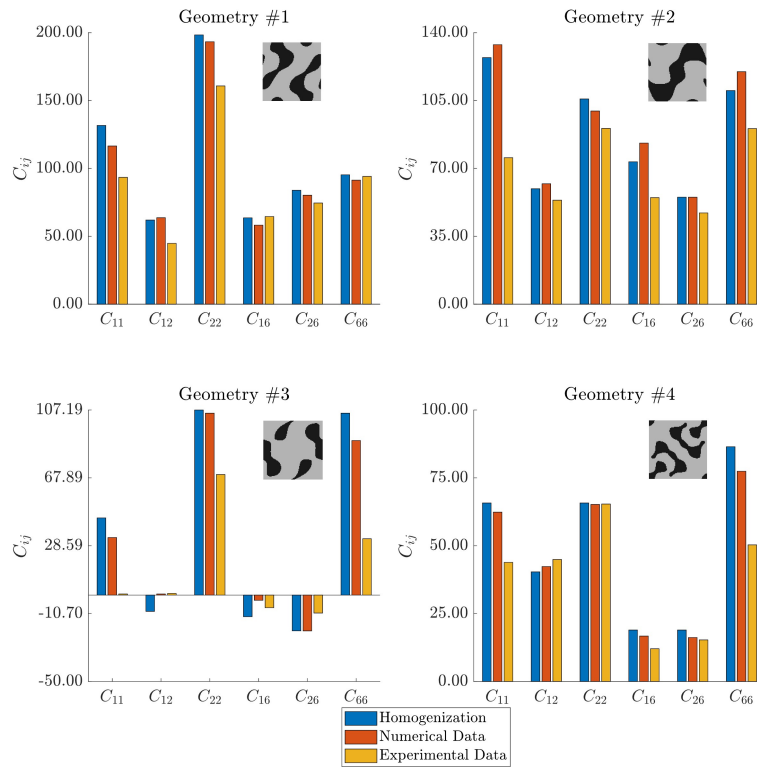
Figure 4.10: Comparison of material parameters identified using the VFM from numerical and experimental data of 10 unit cell tessellations.

We finalize the study by applying the Bayesian method described in Section 4.2 to the experimental data. The resulting marginal posterior probability distributions of the material parameters are shown in Fig. 4.11. It is observed that the computed mean values of the marginal posteriors are

similar to the deterministic results shown in Fig. 4.10. Beyond that, the standard deviations of the marginal posteriors indicate (un)certainty in the parameter predictions. Matching our expectations, the parameter C_{22} is identified with the highest certainty, while for example, the identification of the parameter C_{11} shows a high uncertainty. An interesting observation is made for geometry #3. The parameters identified using synthetic data with the largest error are also the same parameters identified using experimental data with the largest standard deviation in the marginal posterior distribution. Additionally, it is noteworthy that the marginal posteriors of the parameters identified when the Bayesian method is applied to the numerical data show low standard deviations as the data is not affected by the experimental noise (see Fig. 4.12).
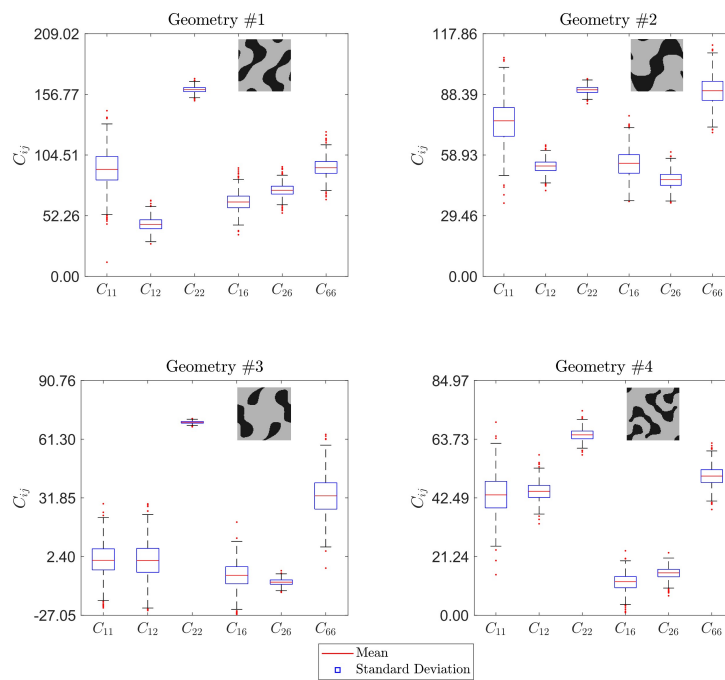
Figure 4.11: Marginal posterior probability distributions of the material parameters obtained through Bayesian linear regression on the experimental data. The red lines indicate the mean of the marginal posterior distributions. The blue boxes indicate the standard deviation from the mean, i.e., the 68% probability interval. The black intervals indicate three times the standard deviation from the mean, i.e., the 99% probability interval.

We note that, for geometry #3, the marginal posterior probability distributions of the parameters exceed the thermodynamically admissible range, e.g., the marginal posterior of C_{11} is partially negative. This must be considered when interpreting the results. In this work, no measure was taken to enforce thermodynamic admissibility in the Bayesian method, which thus remains a future objective.
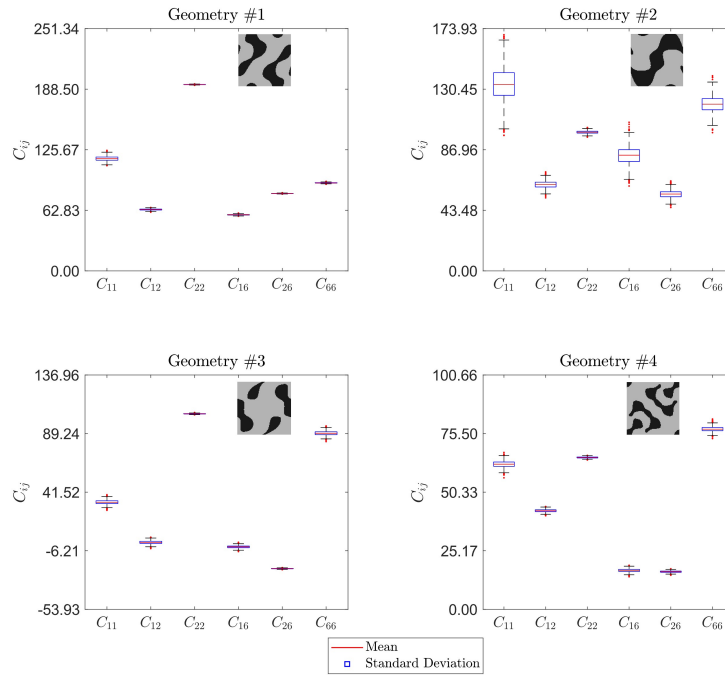
Figure 4.12: Marginal posterior probability distributions of the material parameters obtained through Bayesian linear regression on the numerical data. The red lines indicate the mean of the marginal posterior distributions. The blue boxes indicate the standard deviation from the mean, i.e., the 68% probability interval. The black intervals indicate three times the standard deviation from the mean, i.e., the 99% probability interval.

4.6 Conclusion

In this chapter, we present an approach to identify the 6 independent elastic material parameters of plane anisotropic elasticity from a single experiment, using the virtual fields method. This approach allows for identifying shear-normal coupling parameters experimentally, a task that has remained challenging so far. We first demonstrate the effectiveness of our method using numerically generated data from a single tension test. We then experimentally validate the method on additively manufactured specimens, by measuring full-field displacement data and traction forces. We show that our method is effective for materials that include at least 10 repeated unit cells in their structure, to satisfy homogenization conditions. We calculate the uncertainty in the identification estimation of the material parameters using Bayesian linear regression. In the future, to further refine the experimental parameter identification, it is necessary to optimize the shape of the specimens to ensure strong contributions of strains from different stiffness tensor components. The proposed approach has the potential for measurements of elasticity parameters of complex, anisotropic, three-dimensional structured materials and composites with shear-shear couplings, and for the study of

their nonlinear behavior. A further potential application of the method could be for parameter identification of constitutive tensors corresponding to different types of coupled behavior, such as generalized piezoelectric, flexoelectric, and piezomagnetic tensors.

4.7 Additional figures
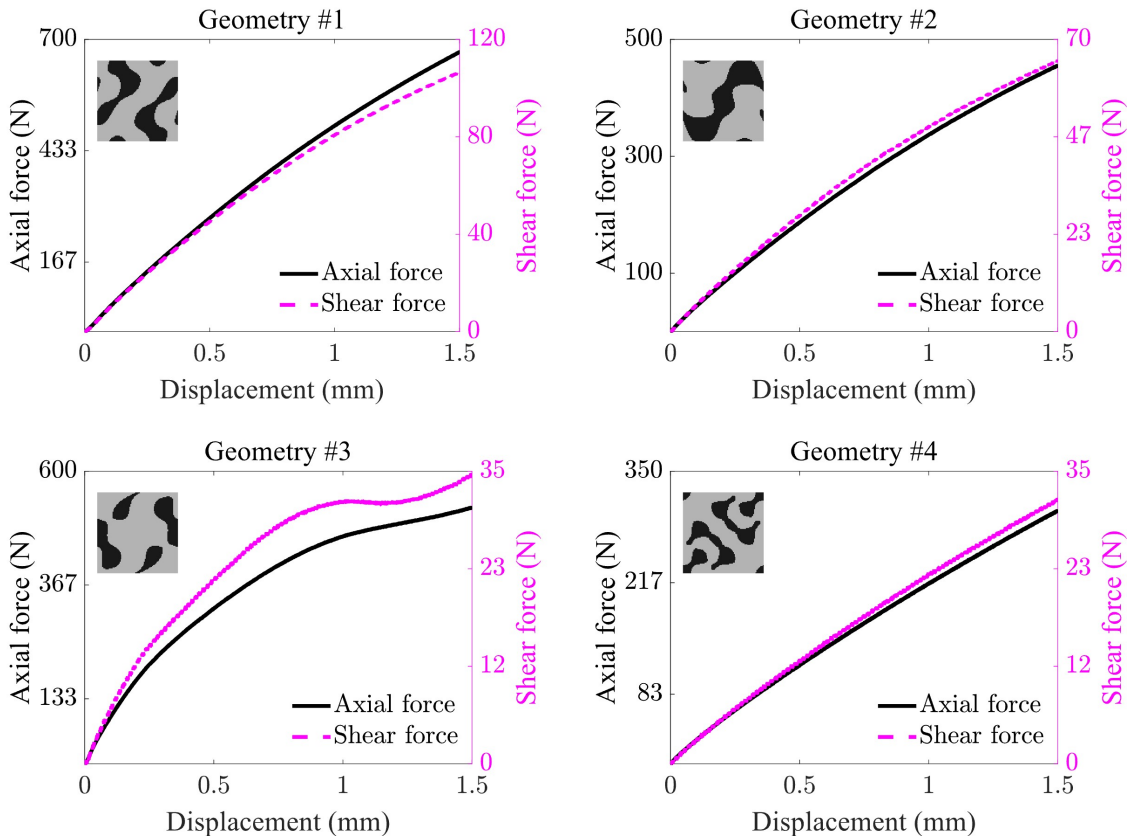
Figure 4.13: Axial and shear load-displacement data for all the experimentally tested specimens.
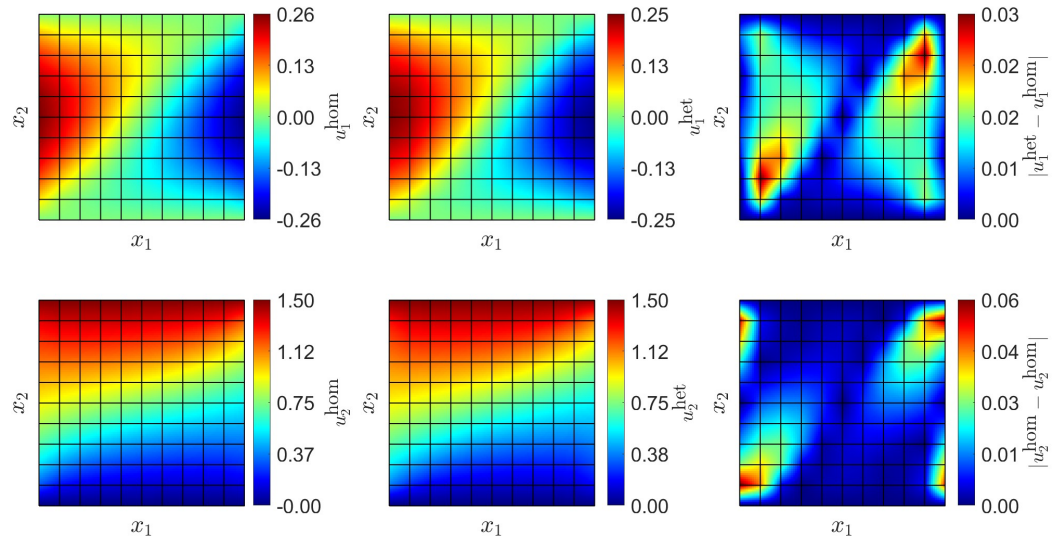
Figure 4.14: Comparison between the displacement fields obtained from finite element simulations of a homogeneous specimen (left) and a heterogeneous structure made of geometry #2 (center). The data is generated and post-processed akin to Fig. 4.7.
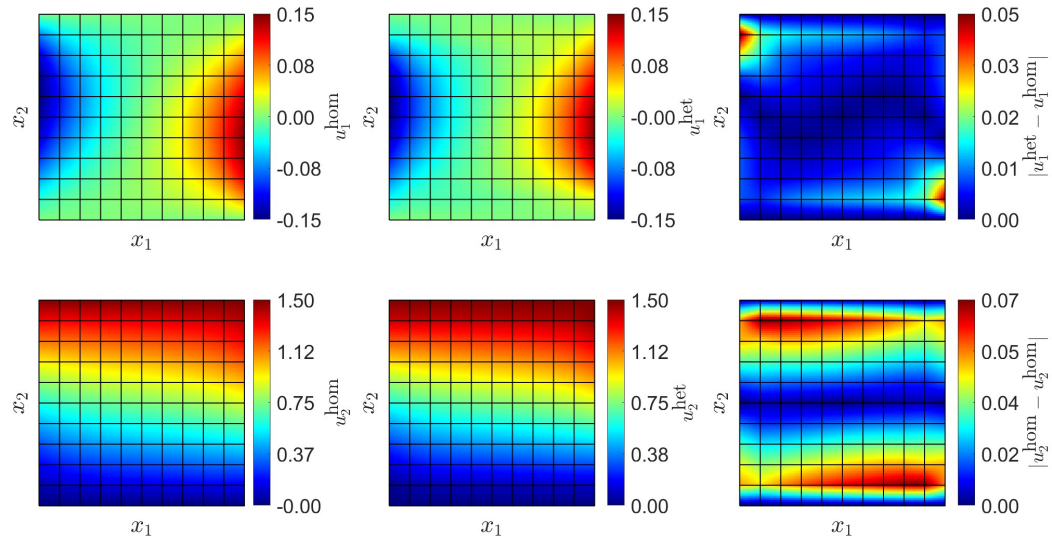
Figure 4.15: Comparison between the displacement fields obtained from finite element simulations of a homogeneous specimen (left) and a heterogeneous structure made of geometry #3 (center). The data is generated and post-processed akin to Fig. 4.7.
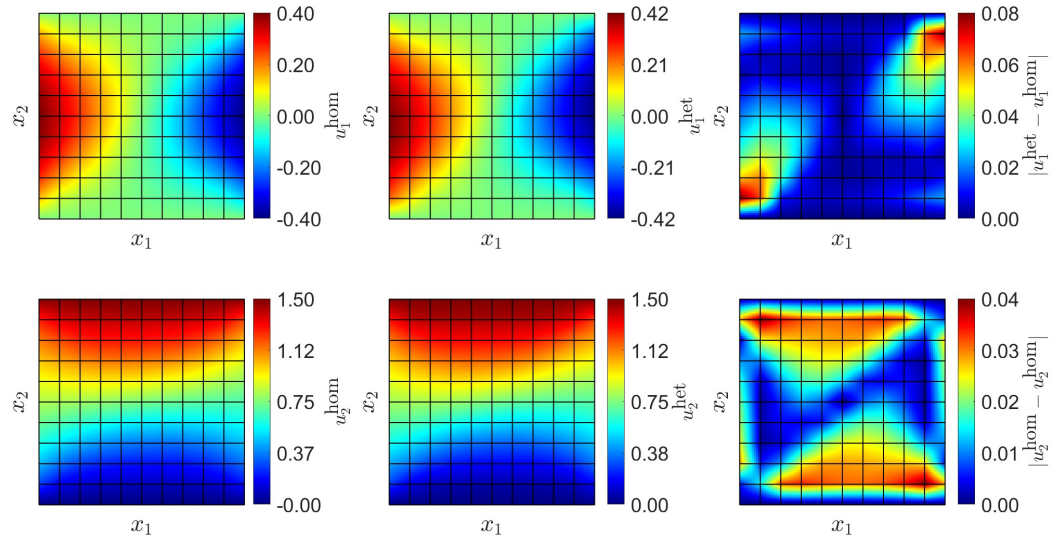
Figure 4.16: Comparison between the displacement fields obtained from finite element simulations of a homogeneous specimen (left) and a heterogeneous structure made of geometry #4 (center). The data is generated and post-processed akin to Fig. 4.7.
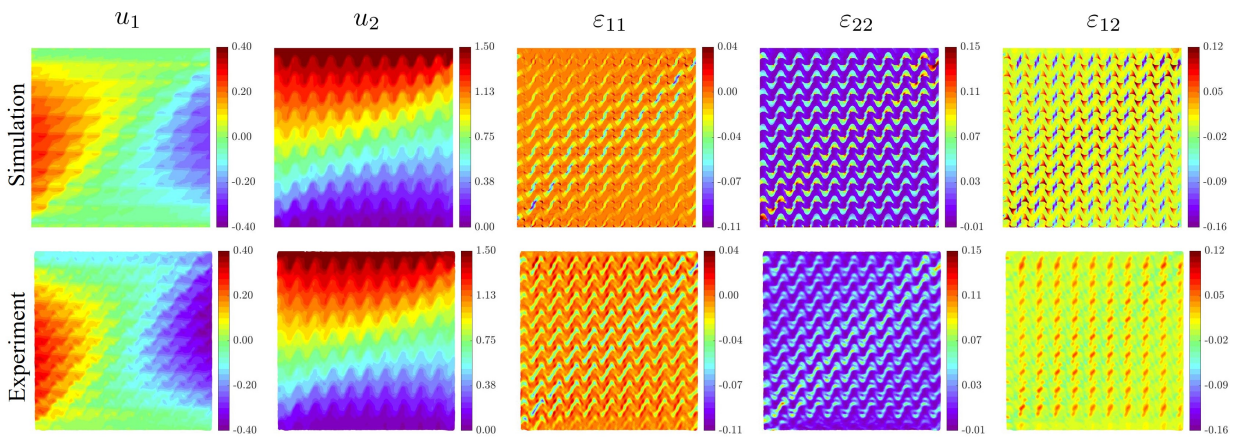
Figure 4.17: Comparison between numerical (top) and experimentally measured(bottom) full-field displacement and strain field data for the 10×10 tessellation of unit cell geometry #2 subjected to displacement-controlled uniaxial tension test.
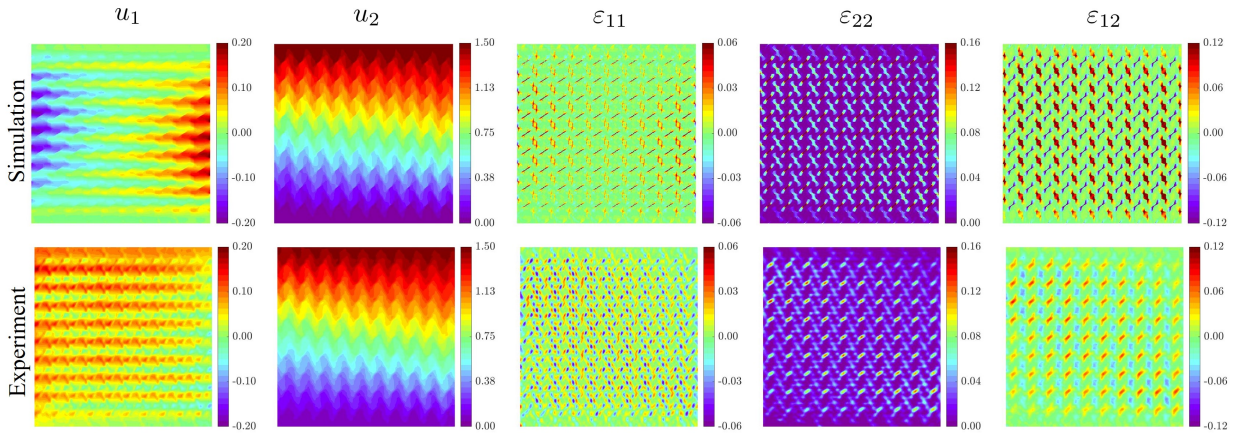
Figure 4.18: Comparison between numerical (top) and experimentally measured (bottom) full-field displacement and strain field data for the 10×10 tessellation of unit cell geometry #3 subjected to displacement-controlled uniaxial tension test.
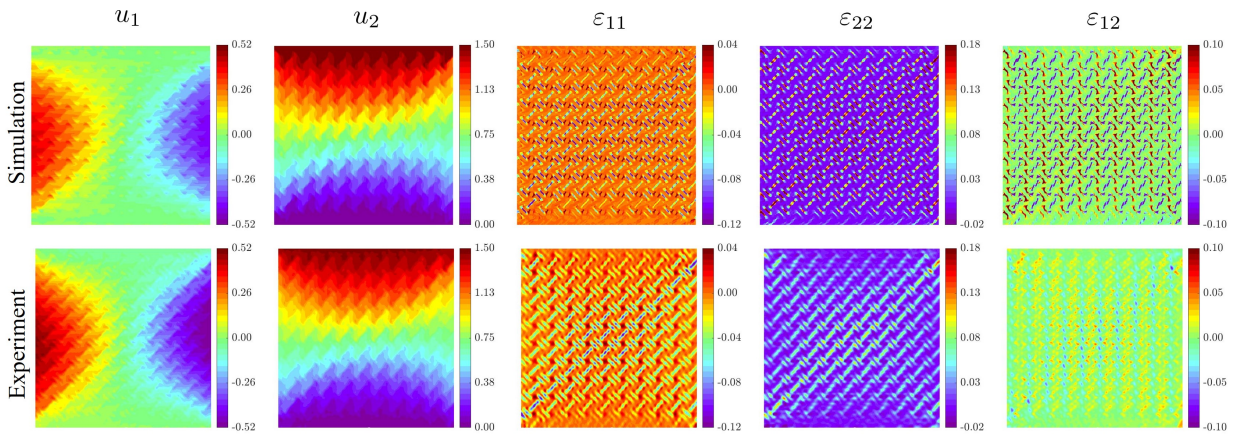
Figure 4.19: Comparison between numerical (top) and experimentally measured (bottom) full-field displacement and strain field data for the 10×10 tessellation of unit cell geometry #4 subjected to displacement-controlled uniaxial tension test.
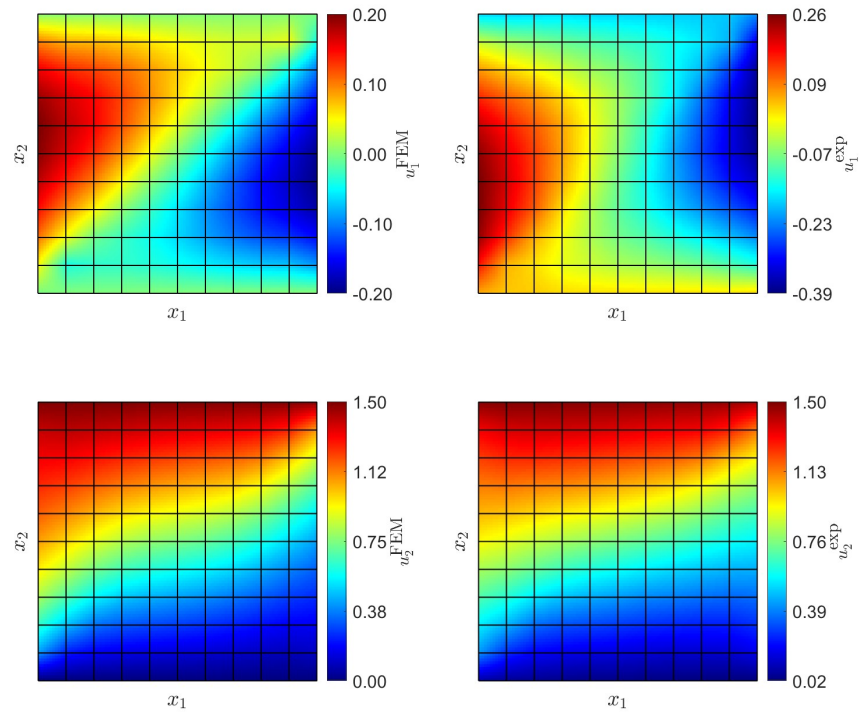
Figure 4.20: Comparison between numerical (top) and experimentally measured (bottom) full-field displacement and strain field data for the 10×10 tessellation of unit cell geometry #1 subjected to displacement-controlled uniaxial tension.
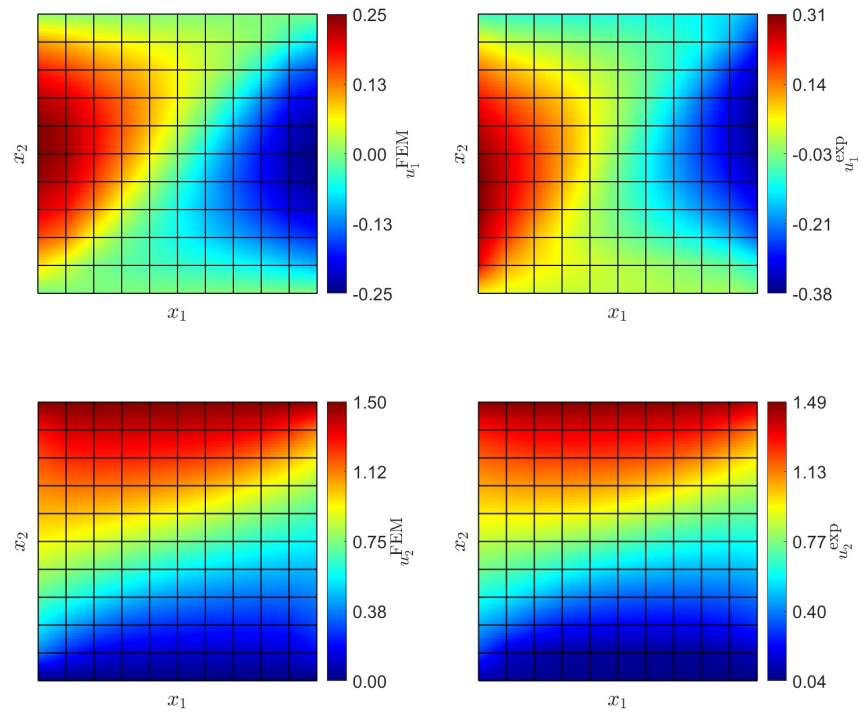
Figure 4.21: Comparison between the synthetic (left) and experimentally measured (right) displacement fields of the heterogeneous structure made of geometry #2. Note that bilinear polynomials are used to interpolate the displacement data at the unit cell corners.
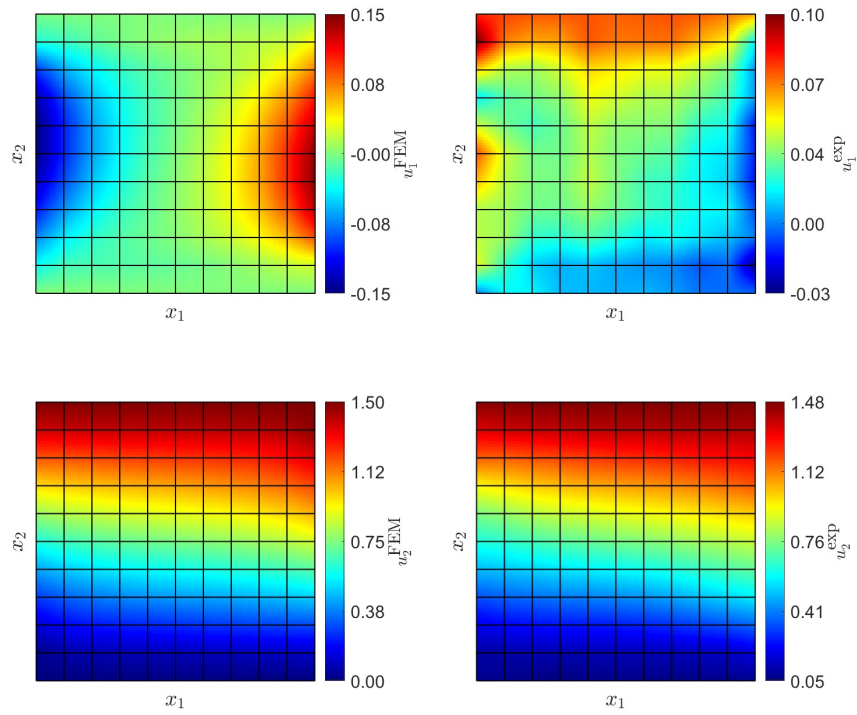
Figure 4.22: Comparison between the synthetic (left) and experimentally measured (right) displacement fields of the heterogeneous structure made of geometry 3. Note that bilinear polynomials are used to interpolate the displacement data at the unit cell corners.
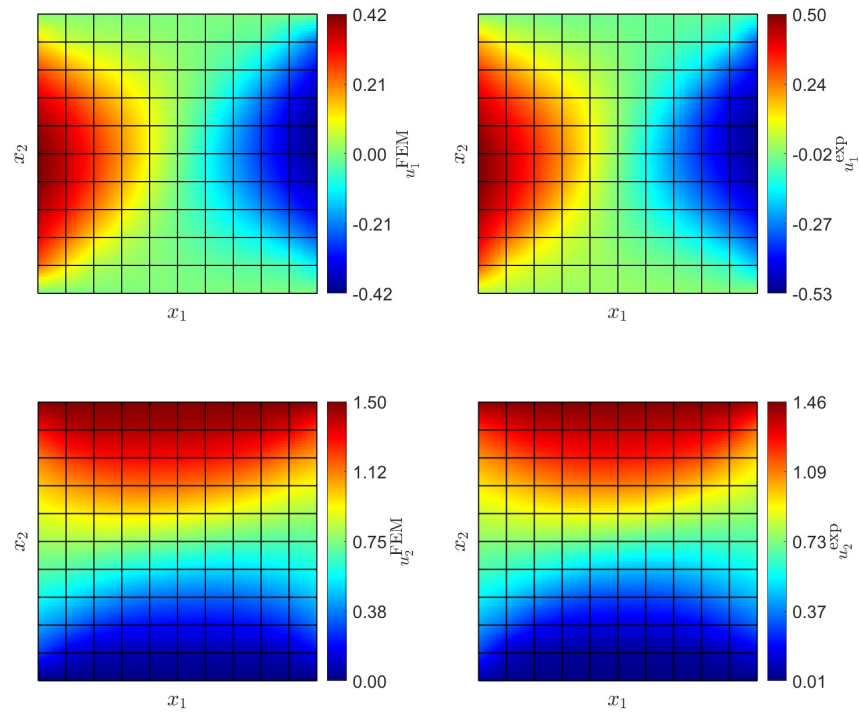
Figure 4.23: Comparison between the synthetic (left) and experimentally measured (right) displacement fields of the heterogeneous structure made of geometry 4. Note that bilinear polynomials are used to interpolate the displacement data at the unit cell corners.
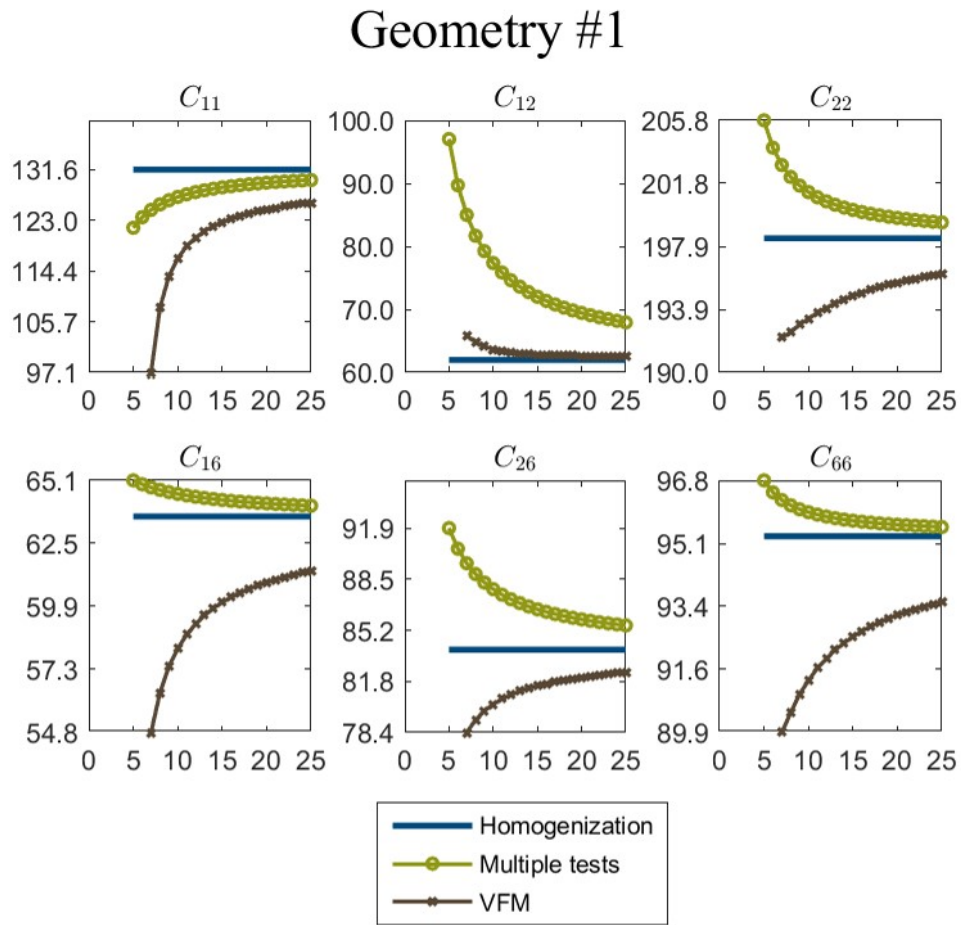
Geometry #1

Figure 4.24: Variation of individual material parameters identified using synthetic data as the number of unit cells for tessellation is varied for geometry #1.
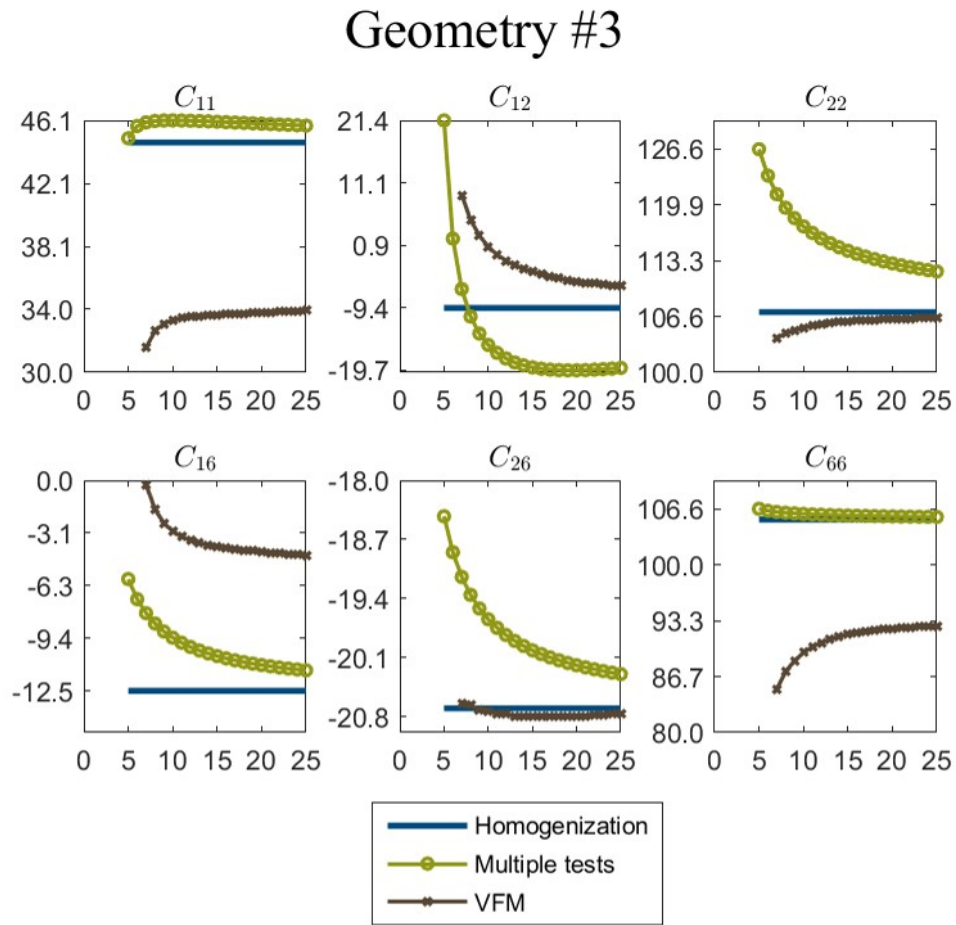
Figure 4.25: Variation of individual material parameters identified using synthetic data as the number of unit cells for tessellation is varied for geometry #3.

C h a p t e r 5

DESIGN OF FUNCTIONALLY GRADED ANISOTROPIC STRUCTURES AND THEIR ANOMALOUS MECHANICAL BEHAVIOR

Jagannadh Boddapati and Chiara Daraio. Planar structured materials with extreme elastic anisotropy. *Under Review*, July 2024.

5.1 Introduction

Functionally graded structures have been shown to exhibit unique mechanical behavior such as avoiding shear-banding [50, 51] and, mimicking bone stiffness [52]. To generate such structures, often the parametrization associated with the structure such as truss thickness is adjusted [53–55]. Therefore, these approaches are particularly effective in controlling the isotropic Young's Modulus, relative density, and to some extent, the degree of orthotropic elasticity [56, 57]. However, achieving smooth spatial gradients in the anisotropic mechanical properties while ensuring the connectivity of adjacent unit cells is challenging. Here, we illustrate the construction of functionally graded anisotropic structures with seamless transition between unit cells with distinct patterns.

5.2 Method of generation of functionally graded structures

For this purpose, we use the proposed functional representation used to generate unit cells in Section 2.3. We introduce the local variables x_1, x_2 as well as the global variables X_1, X_2. The global variables are defined only on a coarser grid, while the local variables are defined on a finer grid. In a graded structure with $p \times q$ unit cells, with $p, q \in \mathbb{Z}^+$, the global variables change at discrete locations given by the unit cell centers, while the local variables X_1, X_2 change at each pixel location within the unit cell at a given x_1, x_2. The function that is required to generate the graded structure $h(x_1, x_2, X_1, X_2)$ is thus given by

$$h(x_1, x_2, X_1, X_2) = \beta(X_1, X_2) f_1(x_1, x_2) + \alpha(X_1, X_2) f_2(x_1, x_2), \qquad (5.1a)$$

$$= \beta(X_1, X_2) \sum_{m,n} A_{mn} \cos\left(2\pi(mx_1 + nx_2)\right)$$

$$+ \alpha(X_1, X_2) \sum_{m,n} B_{mn} \cos\left(2\pi(mx_1 + nx_2)\right), \qquad (5.1b)$$

where $\alpha(X_1, X_2), \beta(X_1, X_2) \in [0, 1]$ are weighing parameters such that $\alpha(X_1, X_2) + \beta(X_1, X_2) = 1$. An increase in α signifies the increase in the contribution of second function $f_2(x_1, x_2)$ in the interpolated unit cell. The threshold to generate graded structure from the function is subsequently set by a bilinear interpolation determined by the thresholds set for the unit cells at the ends.

This method allows for independent control of several functional gradients, such as porosity, anisotropic moduli, and symmetry. In Fig. 5.1A-D, various functionally graded structures are shown with different gradients along the X_1-axis using Eq. (5.1a) while maintaining periodicity along the X_2-axis. Fig. 5.1E-F shows the bilinear interpolation between four unit cells with different anisotropic behavior at four corners of the boundary. By using nonlinearly interpolated weighing parameters, various graded designs such as spiral, star, elliptical, radial and many more can be created as shown in Fig. 5.2. More examples on the graded designs are shown in Fig. 5.3, Fig. 5.4, Fig. 5.5, Fig. 5.6, Fig. 5.7. Further, the interpolation can be extended to construct other conformally mapped strucutres such as radially graded designs as shown in Fig. 5.8. In the next sections, we further investigate the mechanical behavior in two gradient structures with nonlinear interpolations in eliciting atypical mechanical behavior.

5.3 Selective elastic energy localization in radially graded structures

Energy localization refers to the phenomenon where strain energy in a material or structure is concentrated in specific regions. Energy localization finds use in applications such as mechanical sensing [143], and energy harvesting [144]. Here we show that graded structures with anisotropic unit cells achieve selective energy localization, i.e., different localization behavior under different loadings. we achieve this using functionally graded structures with strategically selected unit cells in a radially interpolated design. The unit cells are chosen such that unit cell #1 at the boundary is obtained by a 90° rotation of the unit cell #2 at the interior. The fill fraction of the stiff phase of both the unit cells is 80% respectively. Therefore, this choice makes most of the unit cells in the 20 × 20 interpolated structure also have uniform fill fractions close to 80%. A uniform fill fraction is selected in the graded design to isolate the impact of differences in stiffness parameters from unit cells that may also be affected by varying fill fractions. The (vectorized) stiffness tensor of the unit cell #1 at the boundary is $[0.698\ 0.131\ 0.221\ 0.138\ 0.095\ 0.150]^{T}$ [1]. Therefore, the (vectorized) stiffness tensor of the unit cell #2 is $[0.221\ 0.131\ 0.698\ 0.095\ 0.138\ 0.150]^{T}$.

We subject this graded structure to three different loading conditions namely, tension along x_2 direction, simple shear along applied on the top edge towards x_1 direction, and a biaxial tensile loading by prescribing a displacement of 1.5 mm. In Fig. 5.9, the elastic energy density stored in the structure, defined as $W = \frac{1}{2}\boldsymbol{\sigma} : \boldsymbol{\varepsilon}$ is obtained from finite element analysis (FEA). Here we have used the Einstein summation convention, assuming summation over repeated indices, and the double dot ":" indicates a double contraction of indices. The energy density is plotted first just in the stiff phase, then as areal (volumetric) average at each unit cell while including both the phases. The energy distribution is then compared with an effective isotropic medium. The isotropic equivalent is calculated by replacing unit cell with a material whose bulk and shear moduli are

---

[1]In the vectorized format, the stiffness components are ordered as $[C_{11}, C_{12}, C_{22}, C_{16}, C_{26}, C_{66}]^{T}$.

that of Hashin-Shtrikman upper bound for the corresponding fill fraction. We observe that under tensile loading the energy distribution becomes significantly localized in a few unit cells in the central region. In contrast, for the simple-shear boundary condition, the energy is localized in the diagonal region. For the biaxial loading condition, energy is distributed in the region exterior to the center [2]. The unit cell #2 in the interior has a higher C_{22} compared to the unit cell #1 at

---

[2]It should be noted that the maximum value of the energy density for three loading cases is different. We are
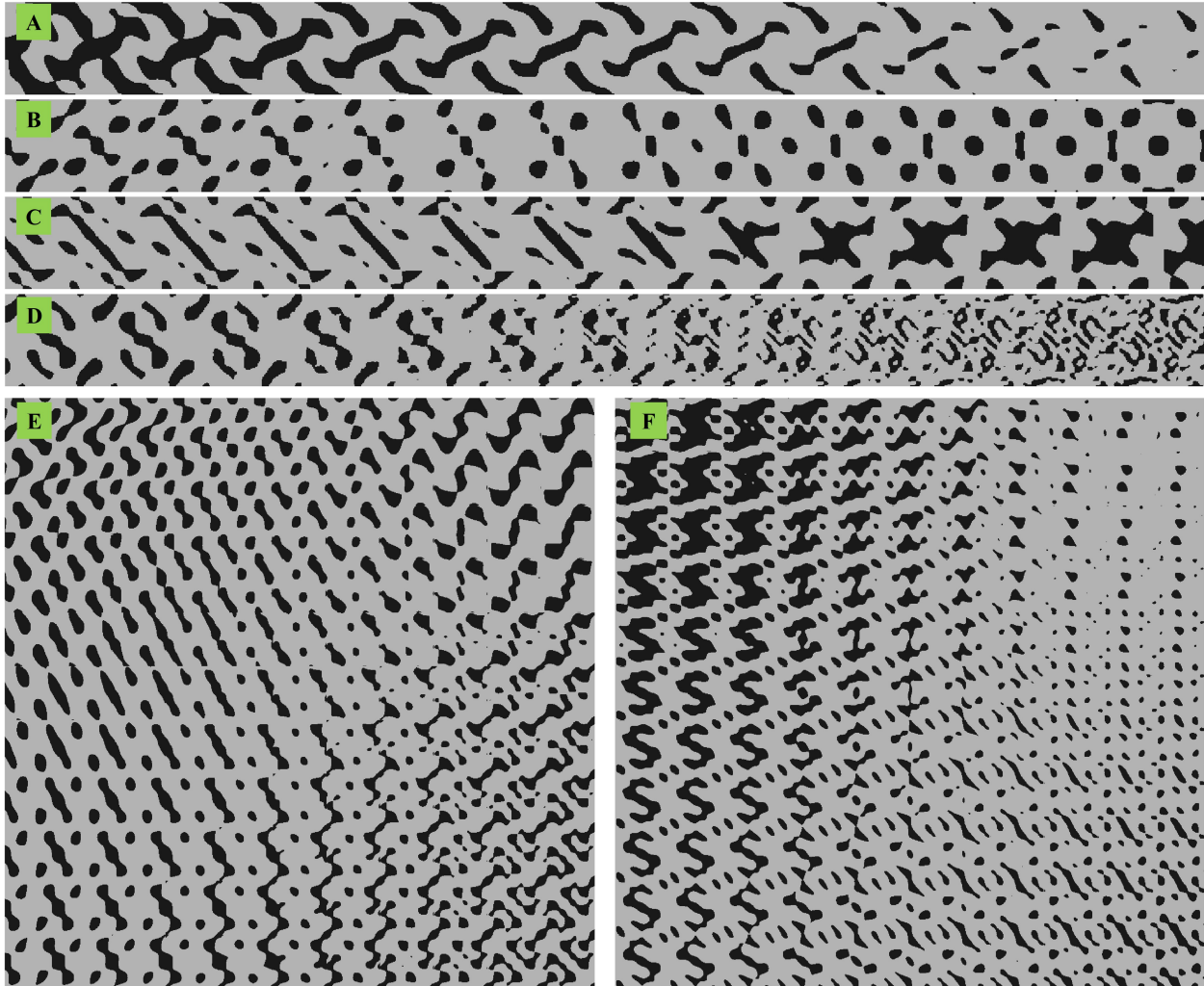
Figure 5.1: Functionally graded metamaterial generation between two unit-cells with different spatial characteristics: (A) increasing volume fraction of the stiff phase while using the same periodic function (B) interpolation from asymmetric to symmetric unit-cells by changing the symmetry in the function weights (C) interpolation between two asymmetric structures with distinct anisotropic properties (D) interpolation between unit-cells with increasing number of spatial modes in the periodic function. (E,F) Interpolation between four unit cells with different anisotropic behavior at four corners of the boundary.
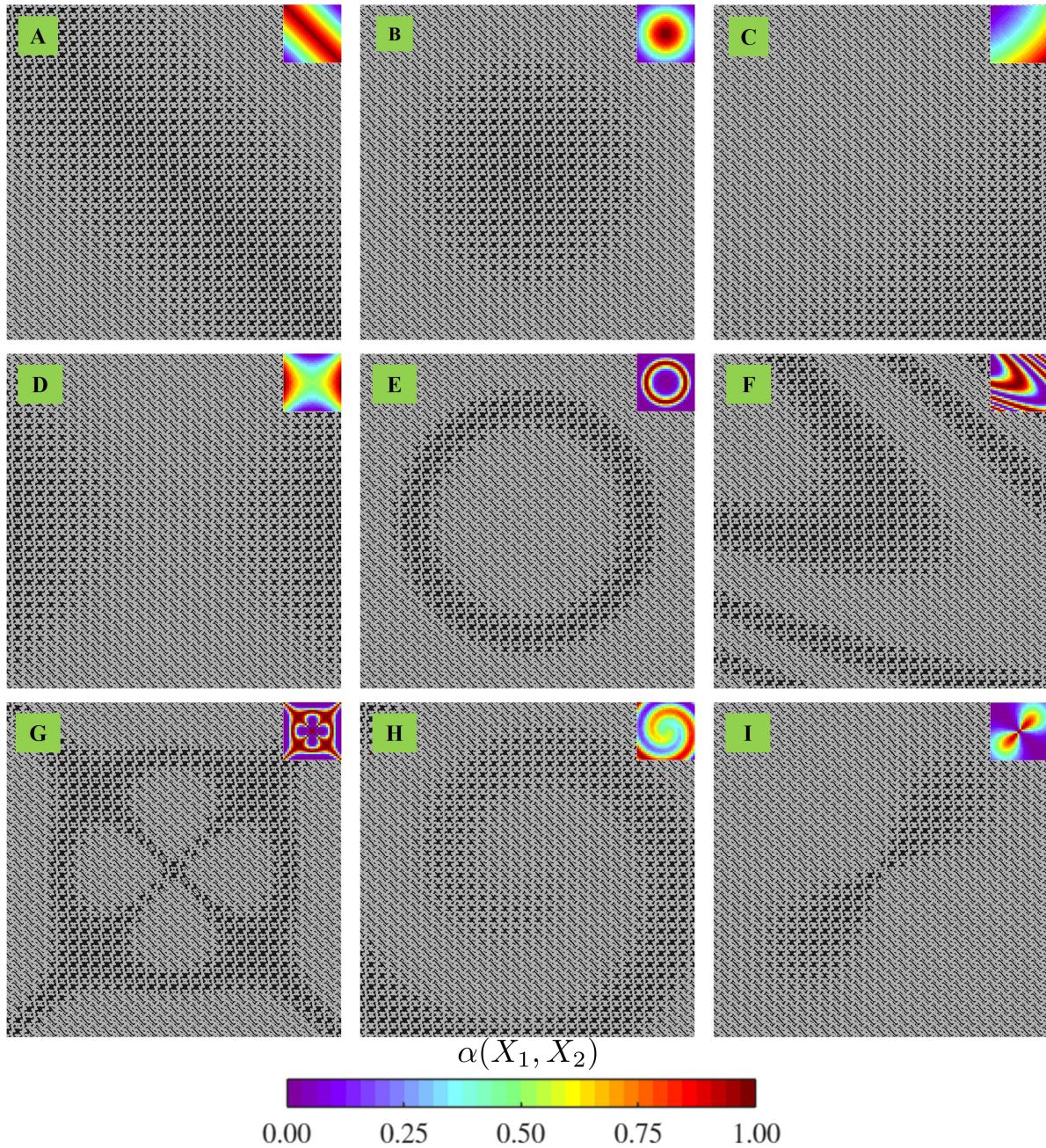
Figure 5.2: Functionally graded metamaterials with various nonlinear interpolations (A) diagonal (B) circular (C) semi-circular (D) hyperbolic (E) annular (F) parabolic (G) star (H) spiral (I) orbital. The colormap transitions from red to blue, illustrating how the interpolation parameter $\alpha(X_1, X_2)$ changes from one unit cell to another. The tessellation contains 30×30 unit cells.

the boundary. Therefore, under tensile loading along x_2 direction, the interior region acts stiffer compared to the exterior region. This geometric frustration results in increased stresses in the

interested in the distribution over the exact values of the energy density distribution.
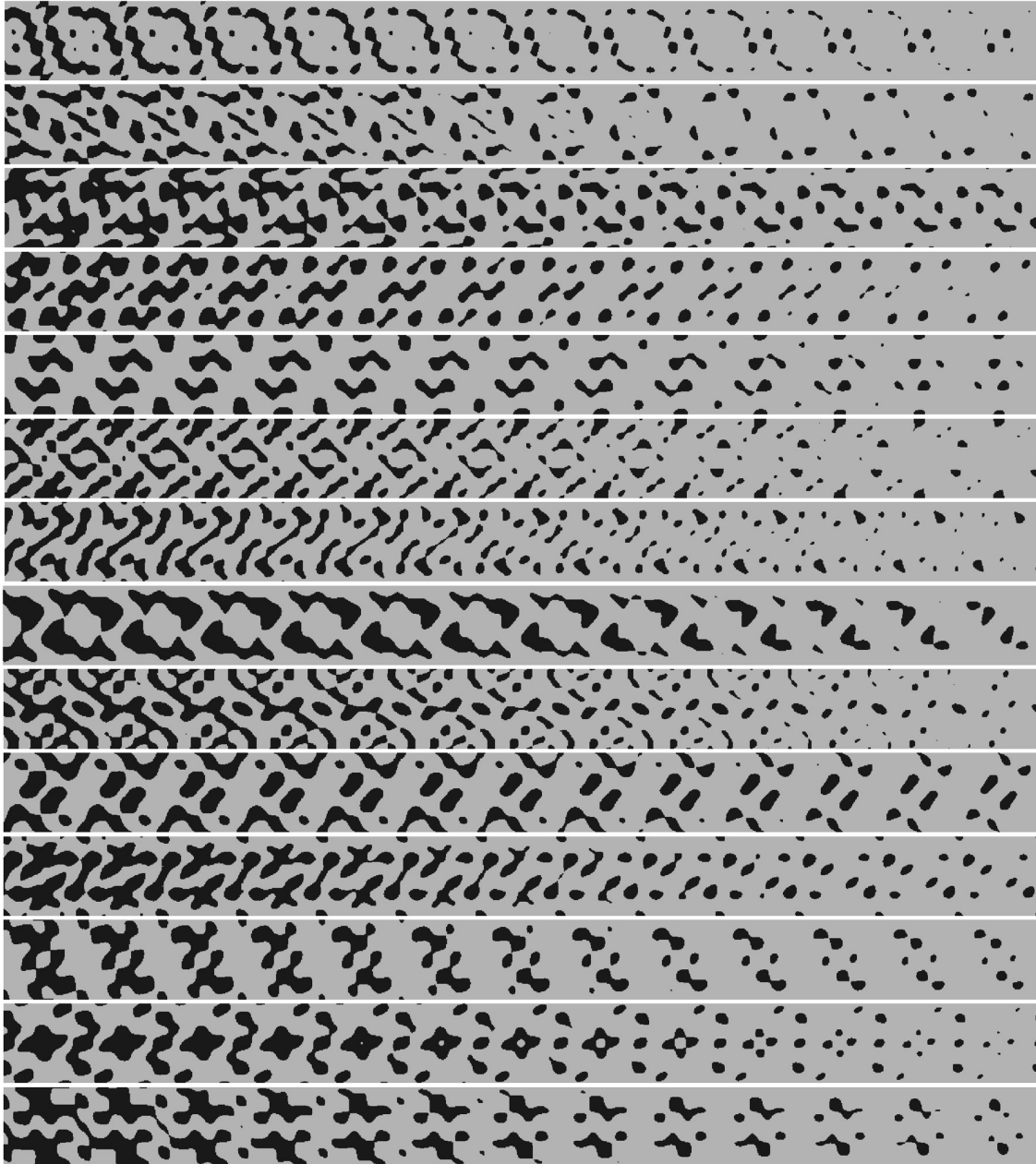
Figure 5.3: Examples of functionally graded structures with increase in fill fraction from left to right. Each of these gradients are generated from a fixed function while increasing the threshold value of the function.

interior region. Subsequently, the energy is significantly localized in the center. As for shear loading, the shear-normal coupling in the unit cells distributes the stresses along the identified diagonal region. In the biaxial loading condition, although the fill fraction of all the unit cells is almost same, the interior region is under relatively lower stresses. If both the unit cells were to be
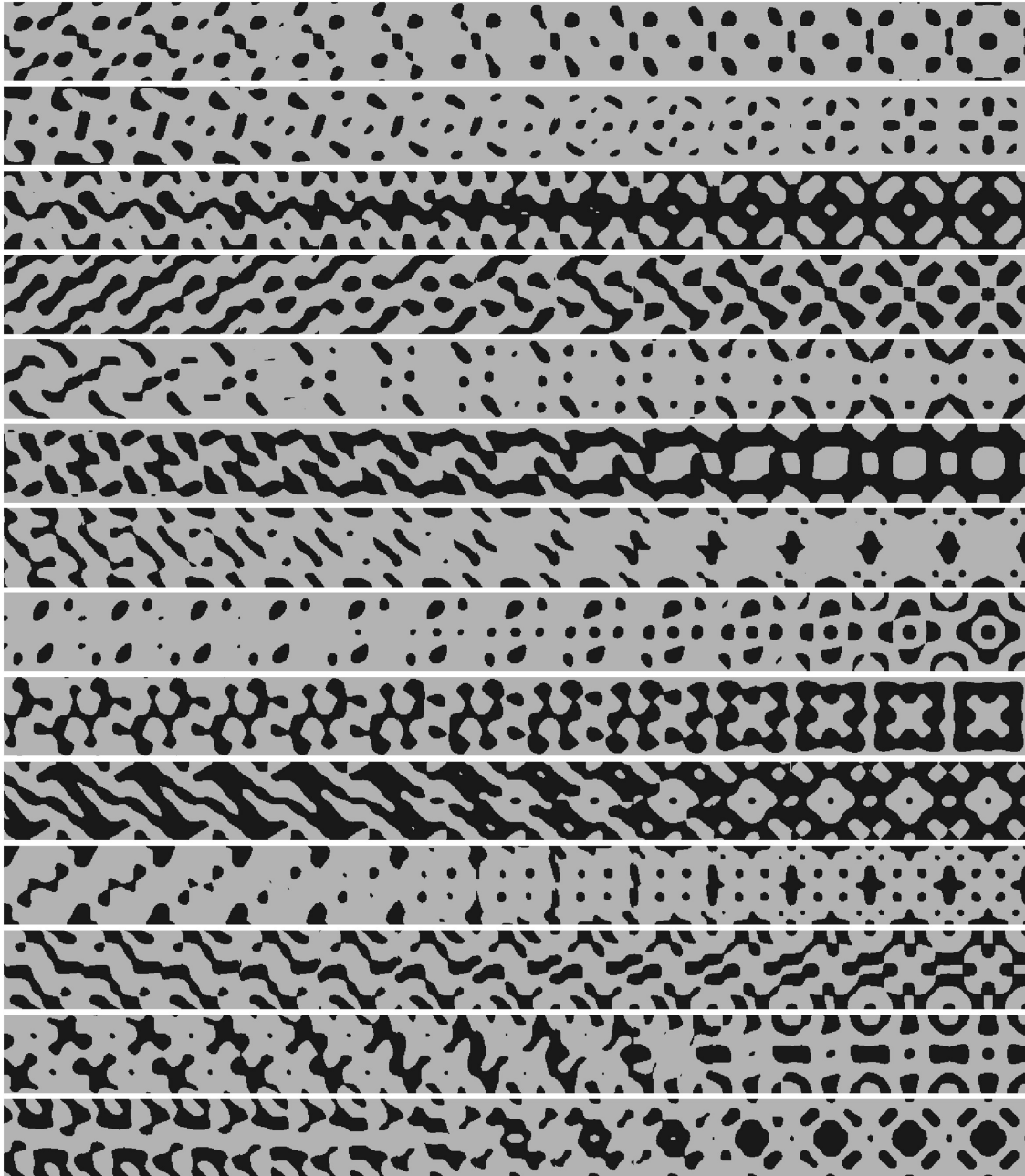
Figure 5.4: Examples of functionally graded structures with interpolation between unit cells that transition from p2 to p4 symmetry from left to right.

isotropic, this distinctive energy localization is not seen. The gradient structures can thus localize energy which can be programmed to have a specific failure mode and/or localize stresses and strains in a preprogrammed location. We further demonstrate the general applicability of this effect when tested with two other unit cells (see Fig. 5.10).
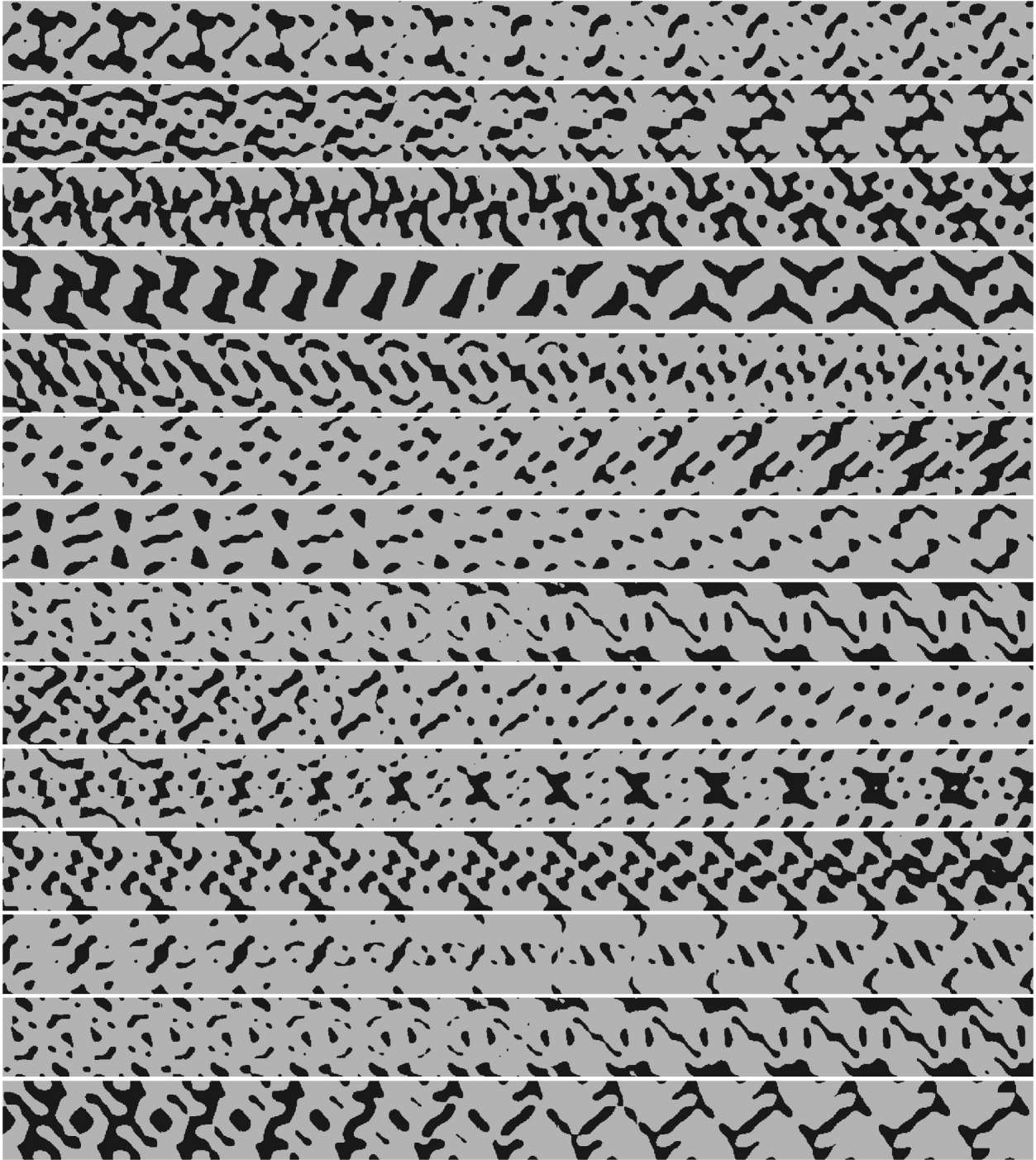
Figure 5.5: Examples of functionally graded structures with interpolation between two unit cells of p2 symmetry.

While plotting the energy density distribution provides valuable insights, localization occurs due to all stress and strain components. To delve deeper into this, we select unit cells where the interior
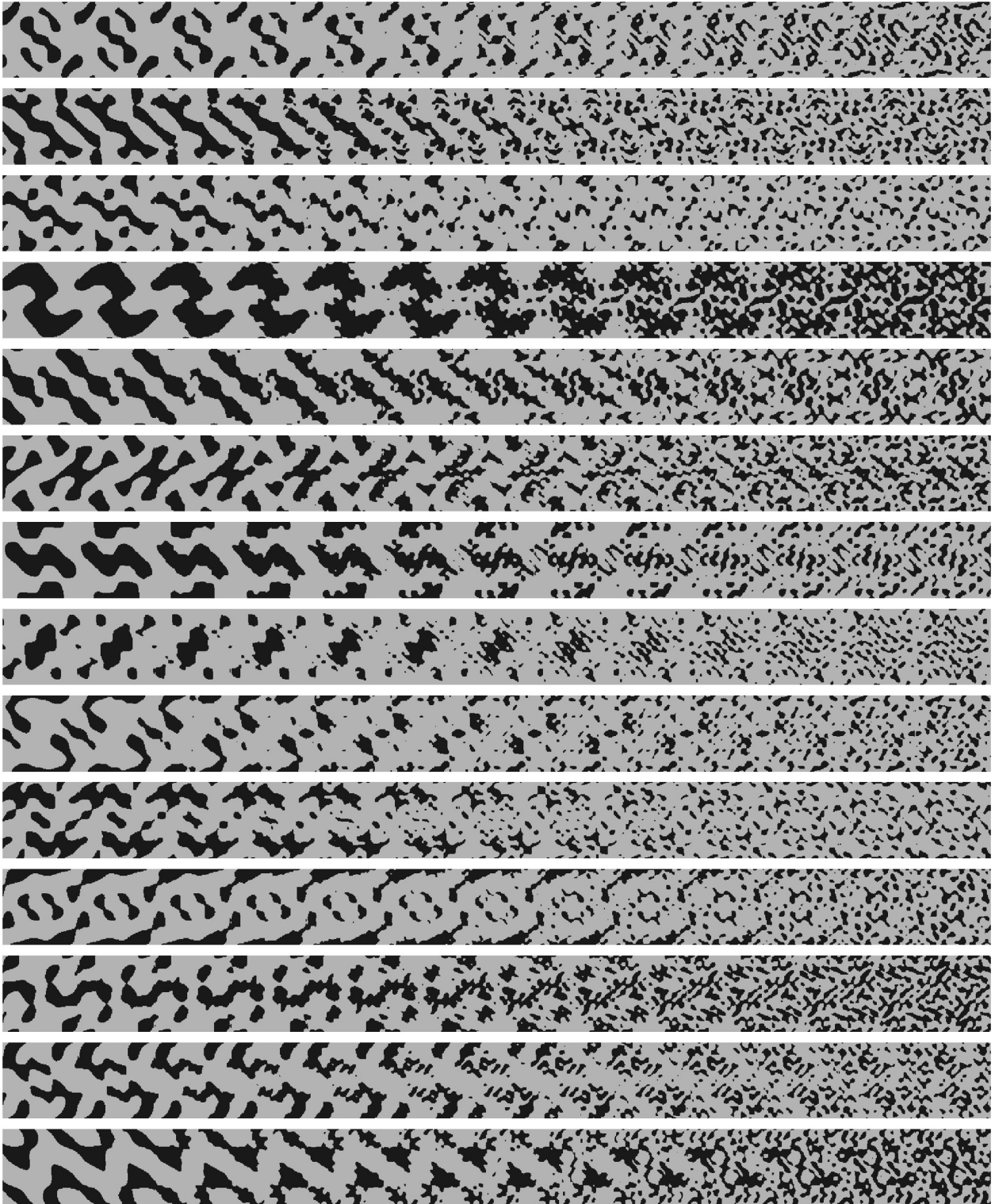
Figure 5.6: Examples of functionally graded structures with interpolation between unit cells that whose number of spatial frequencies increase from left to right.
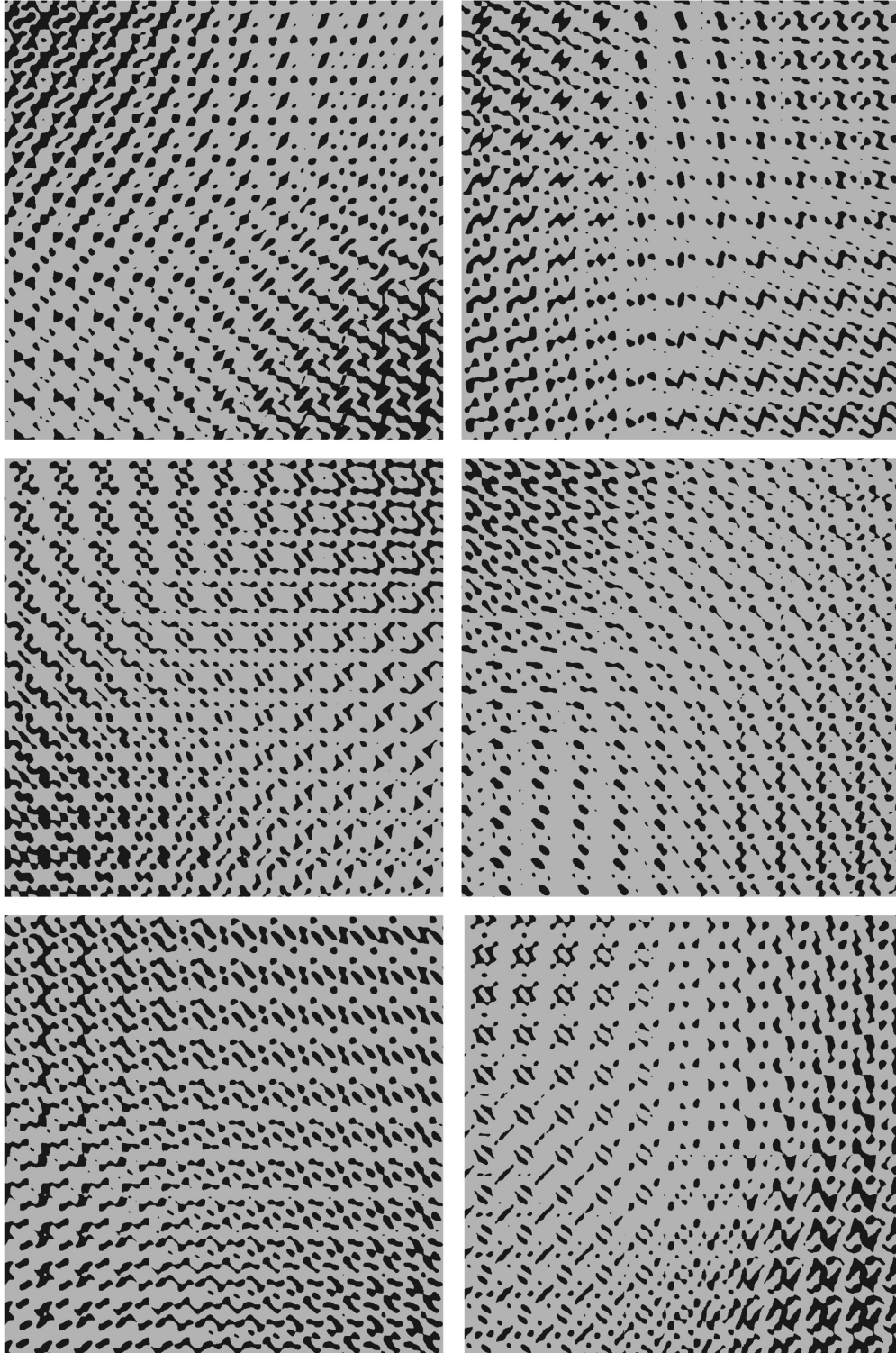
Figure 5.7: Examples of functionally graded structures with bilinear interpolation between four unit cells with distinct patterns.
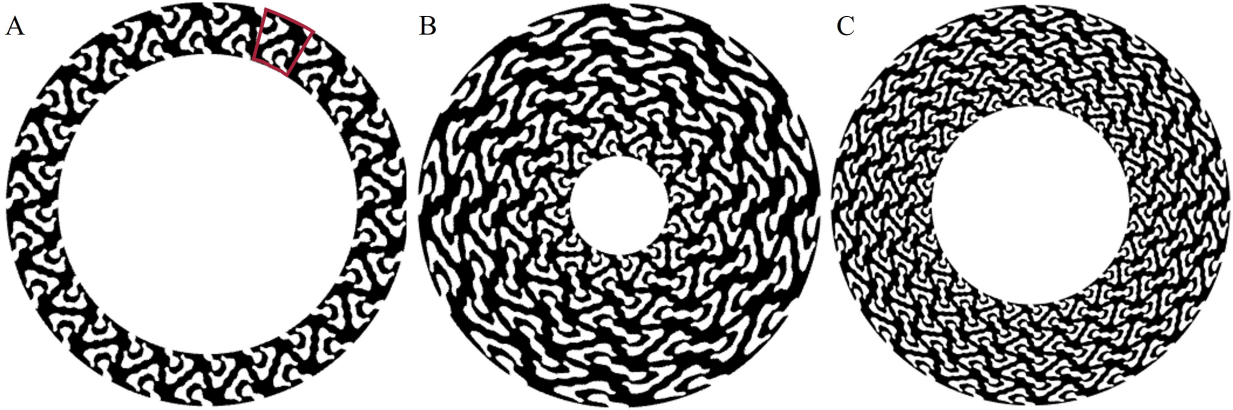
Figure 5.8: Conformally mapped structures along an annular disc using a single unit cell. (A) Mapping with 1 unit cell radially and 24 unit cells along the circumference. (B) Mapping with 4 unit cells radially with 12 unit cells along the circumference. (C) Interpolation with 4 unit cells radially and 24 unit cells along the circumference. 1D gradients shown in Fig. 5.1 could be further incorporated into these conformally mapped designs radially and/or along the circumference.

region contains those with negative values for C_{12}, while the exterior region contains positive values for C_{12}, as depicted in Fig. 5.11. The (vectorized) stiffness tensor of the unit cell #1 (UC1) at the boundary is $[0.134\ 0.082\ 0.370\ \text{-}0.050\ \text{-}0.120\ 0.107]^T$. Similarly, the (vectorized) stiffness tensor of the unit cell #2 (UC2) in the interior is $[0.171\ \text{-}0.009\ 0.096\ 0.001\ \text{-}0.017\ 0.248]^T$. The fill fraction of the stiff phase for the unit cells is $[73.7\%, 59.2\%]$, respectively. The behavior of this design under tensile loading is studied. In this specific scenario, we observe that unit cells in the interior exhibit chiral characteristics, resulting in lateral expansion akin to auxetic behavior. Conversely, unit cells in the exterior, lacking chirality, contract laterally under tensile loading. This geometric mismatch compels interior unit cells to experience compression despite their inherent tendency to expand. Consequently, the region with softer-like properties bears greater stresses and strains, leading to a concentration of energy in the center.

5.4 Non-affine deformations in structures with annular interpolation

Non-affine deformations refer to deformations of a material where the local strain or displacement of the material points does not follow the global deformation applied to the material. Often soft materials such as polymers, biological tissues, and granular systems exhibit non-affine deformations due to the rearrangement of molecules, particles and/or grains [145, 146]. Such non-affine deformations play a crucial role in energy dissipation.

Here, we present an example of inducing non-affine deformations in metamaterials on a global scale by utilizing functionally graded structures with strategically selected unit cells. The two

unit cells selected for interpolation are chosen such that their off-diagonal shear-normal coupling moduli are opposite in sign while the other moduli and fill fraction are comparably close. We then create an annular interpolated structure as discussed in Fig. 5.2C with 20 unit cells along each axis. Please refer to Fig. 5.12 for more details on the selection of unit cells and their interpolation. The (vectorized) stiffness tensor of the unit cell in the boundary upon normalization is $[0.374, 0.101, 0.108, 0.134, 0.066, 0.110]^T$. The (vectorized) stiffness tensor of the unit cell in the annular region upon normalization is $[0.115, 0.121, 0.494, -0.084, -0.147, 0.138]^T$. The fill fraction of the stiff phase for the unit cells is $[62.7\%, 69.5\%]$, respectively. As a result, most of the unit cells in the 20 x 20 interpolated structure have fill fractions close to 65%.
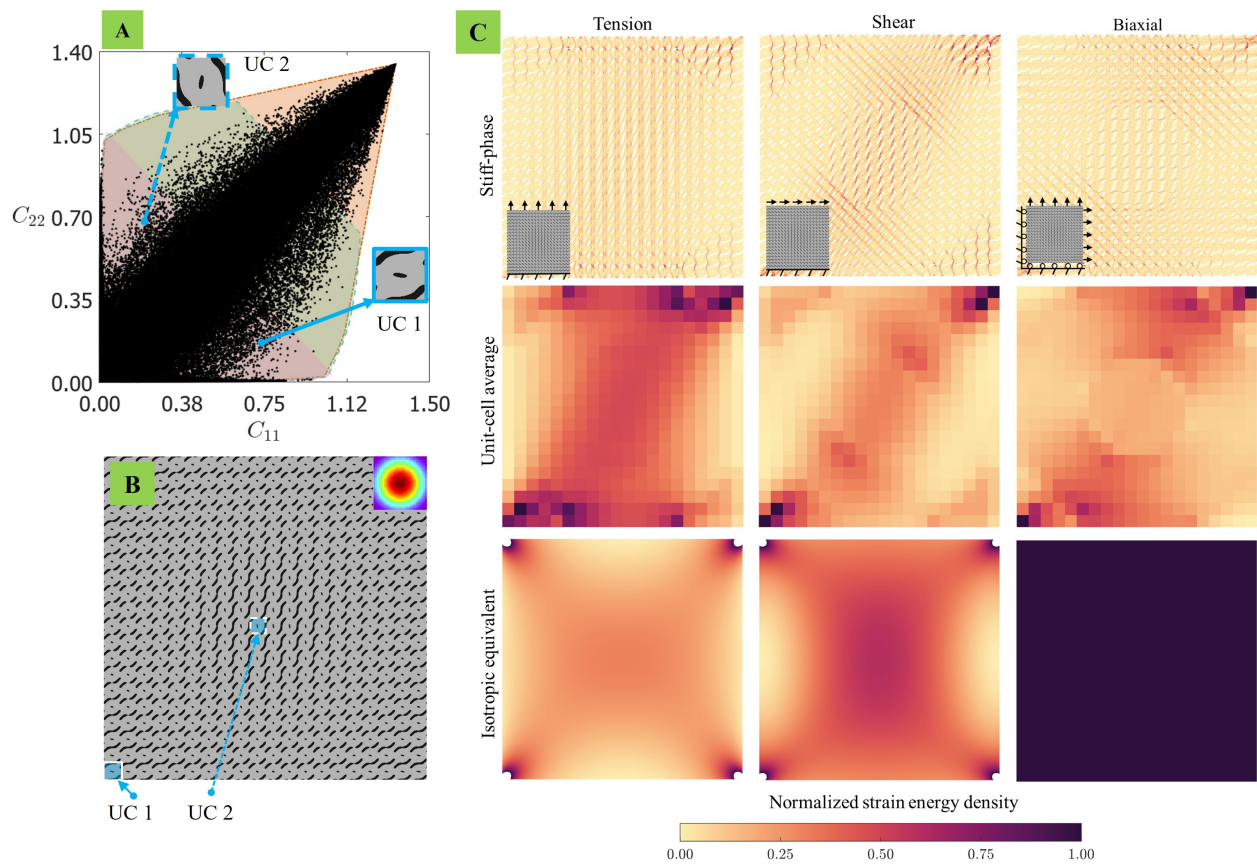
Figure 5.9: Demonstration of selective energy localization: (A) Unit cell selection based on the extremity in the property space plot of C_{11} vs. C_{22}. (B) Radially graded design with 20×20 tessellation from the chosen unit cells named UC1, UC2. The inset color map shows the variation of interpolation parameter $\alpha(X_1, X_2)$. (C) Distribution of (normalized) elastic energy stored in the circularly interpolated structure for tensile, shear, and biaxial loading displaying selective energy localization arising from anisotropy of the unit cells. The first row shows the energy distribution in just the stiff phase, the second row shows the energy averaged over each unit cell, the third row shows the energy distribution in a continuum-isotropic equivalent.
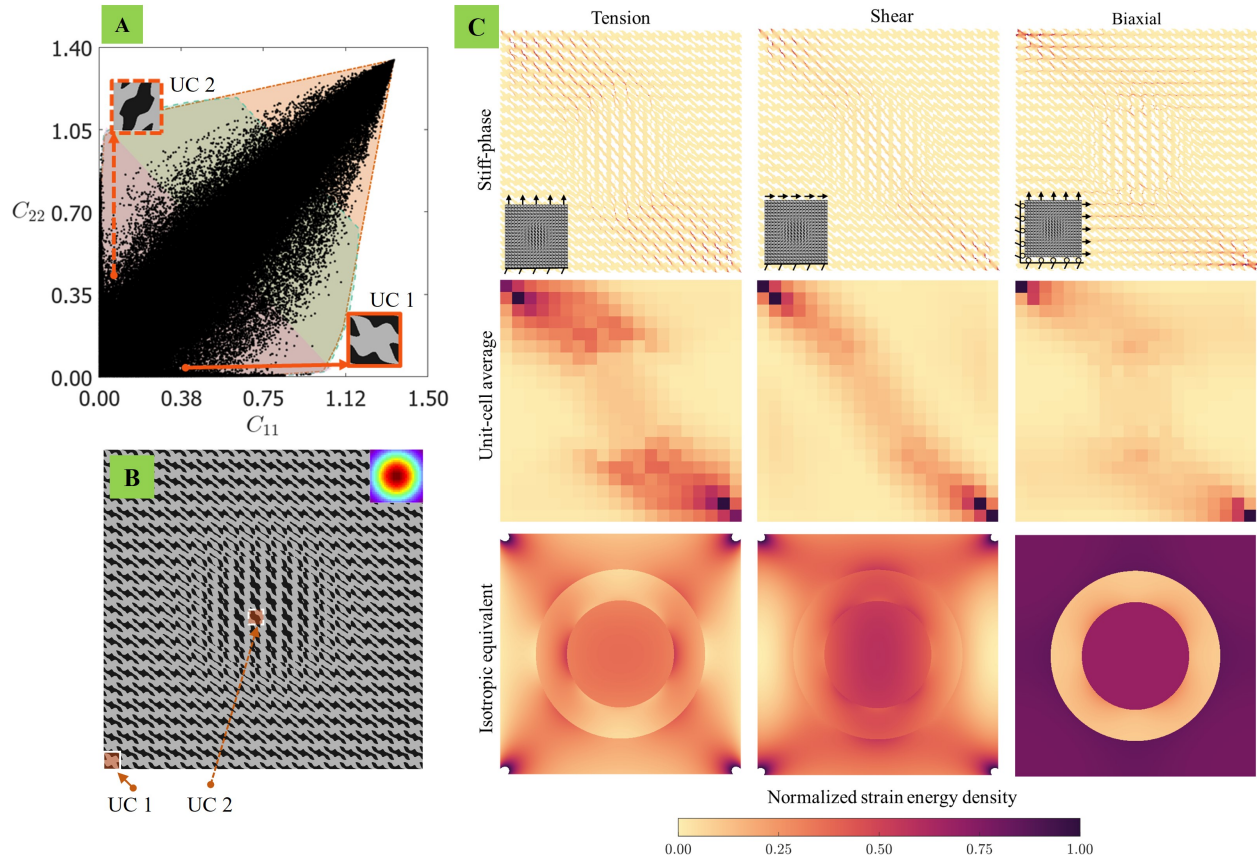
Figure 5.10: Another demonstration of selective energy localization in radially graded structure akin to Fig. 5.9. (A) Unit cell selection based on the extremity in the property space plot of C_{11} vs. C_{22}. The elasticity tensor of the unit cell (named UC 1) at the boundary is [0.378, 0.066, 0.068, -0.083, -0.041, 0.067]^T. The elasticity tensor of the unit cell (named UC 2) at the interior is [0.116, 0.086, 0.479, -0.077, -0.078, 0.097]^T. The fill fractions of the stiff phase in the unit cells are [59.9%, 59.3%], respectively. (B) Radially graded design with 20×20 tessellation from the chosen unit cells UC 1, UC 2. (C) Distribution of (normalized) elastic energy stored in the circularly interpolated structure for tensile, shear, and biaxial loading displaying selective energy localization arising from anisotropy of the unit cells. Although the fill fractions of the two unit cells are almost the same, the radial interpolation resulted in unit cells with higher fill fractions in the interface part of the graded region. Therefore, an approximate annular region filled with a stiffer isotropic medium is used when calculating the isotropic equivalence.

This structure is subjected to a tensile loading along x_2 direction by prescribing a displacement of 1.5 mm at the top end. In Fig. 7.1, the numerical simulations (assuming linear elasticity) reveal that the horizontal displacements exhibit a rotation-like characteristic under this tensile loading. We further experimentally corroborate the same behavior using full-field measurements obtained using digital image correlation (DIC). More details on the experimental procedure can be found in Section 2.4. This non-affine deformation behavior seems to arise from the incompatibilities in

the off-diagonal shear-normal coupling moduli (C_{16}, C_{26}) between the two selected unit cells. The unit cells with positive shear-normal coupling moduli have a preferential direction to shear under tension, which is opposite to the preferential direction of the unit cells with negative shear-normal coupling moduli. Therefore this incompatibility in the preferential direction to shear under tension creates internal torque and directs the annular region to rotate while extending in the x_2 direction. In Fig. 5.14, we demonstrate that the observed behavior can also be seen in other pairs of unit cells with opposing shear-normal coupling moduli. Additionally, experimentally measured strains are presented for this example in Fig. 5.15, indicating the localization of strain around the annular region.
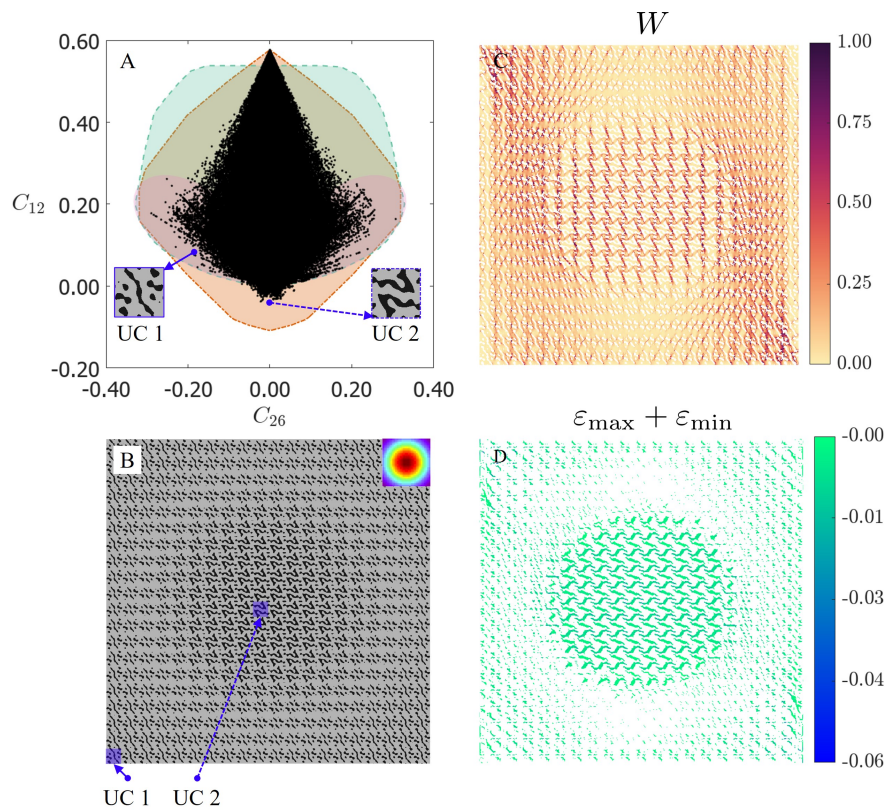
Figure 5.11: Compressive strains under tensile loading: (A) Unit cell selection based on the extremity in the property space plot of C_{26} vs. C_{12}, such that (B) the radially graded design from the selected unit cells that can be additively manufactured using only the stiff phase. (C) Normalized energy distribution in the stiff phase under tensile loading applied along x_2 direction. (D) The plot of the sum of principal strains (compressive part only) in the stiff phase which shows compressive strains in the interior region of the radially graded design under the applied tensile loading. Due to geometric incompatibility, the unit cells in the interior undergo compressive strains and compressive stresses under tensile loading.
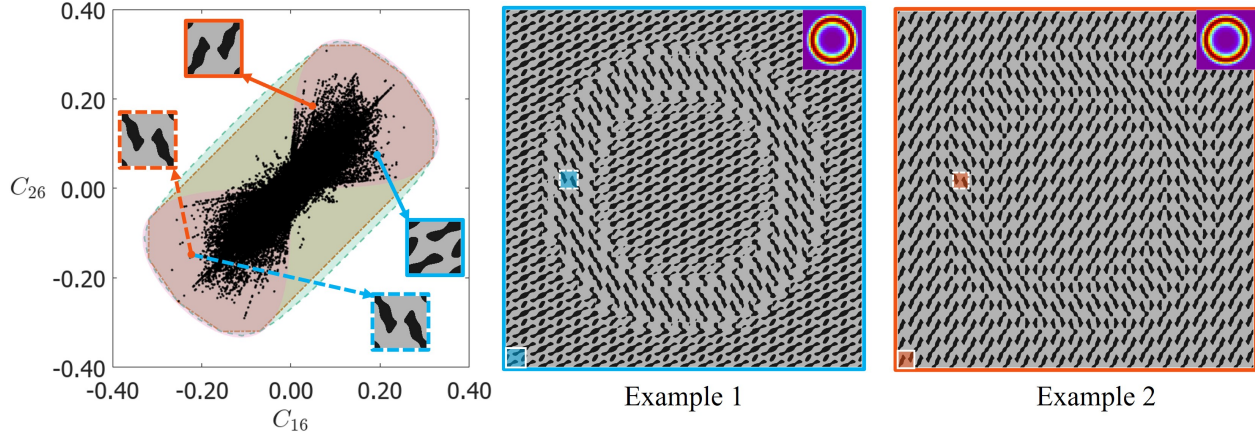
Figure 5.12: The selection of unit cells used for annular interpolation is based on the extremity of the property plot of C_{16} vs. C_{26}. The annular interpolations in examples 1 and 2 illustrate non-affine rotation-like deformation under tension in Figs. 5.14 and 7.1. Note that in example 2, the unit cell in the annular region is obtained by a 90° rotation of the unit cell at the boundary. Additionally, it is important to mention that these designs can be fabricated using only the stiff phase.

5.5 Supercell tessellations and their scale-dependent behavior

Here, we explore the mechanical behavior of a tessellation obtained by repeating the supercell 4 × 4 times. We define the supercell as the entire annular interpolated structure shown in Fig. 7.1 with 20 × 20 unit cells. In Fig. 5.16, we plot the displacement and strain contours from the FEA on this supercell tessellation subjected to tensile loading by prescribing a displacement of 1.5 mm. Due to computational limitations, we limit our study to a 4 × 4 tessellation and reduce the unit cell size to 50 pixels from 100 pixels. For this 4 × 4 supercell tessellation, therefore, there are a total of $4 \times 4 \times 20 \times 20 = 6400$ unit cells resulting in a finite element mesh with $6400 \times 50 \times 50 = 16,000,000$ elements. We observe that the non-affine rotation-like deformations induced by geometric frustration are present in this supercell tessellation at all the annular regions. Additionally, there is an observed gradient in this non-affine behavior in the horizontal displacement component (U_1). However, the magnitude of the horizontal displacement is reduced compared to the single supercell. There are non-local interactions from the neighboring annular regions. Similar behavior is observed in the case of supercell tessellation of example #2, as shown in Fig. 5.17. This suggests that the length scale as well as the separation between the annular regions play a significant role in affecting this rotation-like behavior, indicating the need to utilize micropolar elasticity in the context of such non-affine deformations in mechanical metamaterials [147].

In the future, a detailed investigation into this scale dependence could be conducted using a multi-scale homogenization approach. Further, it is interesting to note that when this structure is subjected to simple shear loading no distinct non-affine deformation is observed, as the unit

cells do not differ in the shear-modulus like parameter C_{66}. Therefore, investigations on the role of incompatibilities in other moduli may unveil new insights into graded structures experiencing geometric frustration under other complex loading conditions. Finally, exploring other choices of unit cells with contrasting moduli interpolated non-linearly could reveal unseen atypical mechanical behavior, which we leave for future work. In metallic materials with microstructure, defects such as grains and grain boundaries serve as strengthening mechanisms by creating incompatibilities that obstruct simple deformation paths. For example, twin boundaries that arise when a sufficiently high shear load is applied, act as an energy dissipation mechanism contributing to the plasticity of various metals. Therefore, the nonlinear interpolations introduced in this work could be utilized to design strengthening mechanisms in metamaterials, notably for energy dissipation and impact loading, extending beyond lattice materials as discussed further in [148].
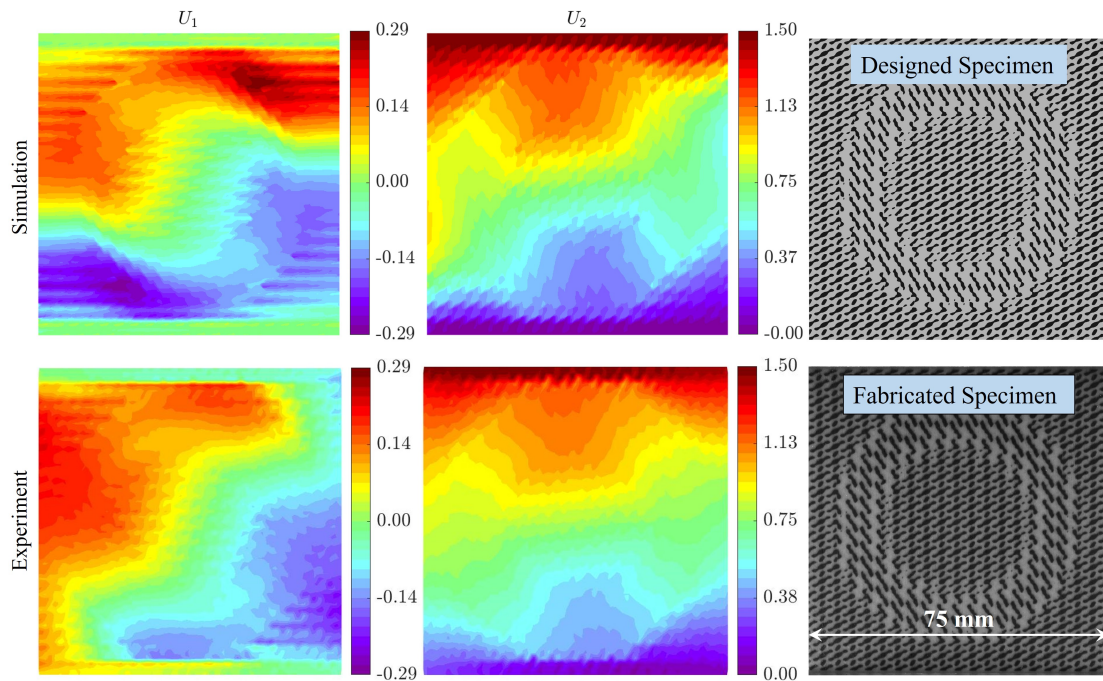
Figure 5.13: Rotation-like deformation under tensile loading in a gradient structure made with annular interpolation. The prescribed displacement is 1.5 mm. The unit cell selection is discussed in Fig. 5.12. The geometric incompatibility between two unit cells with opposing shear-normal coupling behavior leads to non-affine deformation. The top row shows finite element simulation results while the bottom row shows the displacement contours measured using the digital image correlation (DIC) on an additively manufactured specimen.
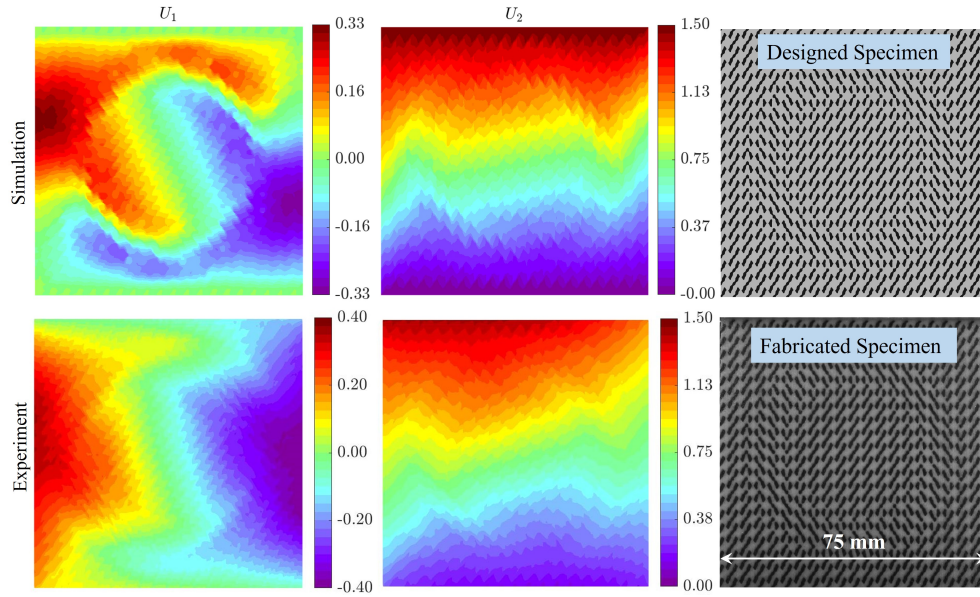
Figure 5.14: Rotation-like deformation under tensile loading in the gradient structure named example 2 as shown in Fig. 5.12 made with annular interpolation. The geometric incompatibility between two unit cells with opposing shear-normal coupling behavior leads to non-affine deformation. The top row shows finite element simulation results while the bottom row compares the displacement contours measured using the digital image correlation (DIC) on an additively manufactured specimen.

5.6   Conclusion

In this chapter, by utilizing the unit cells with extreme anisotropy that lie on the property gamut boundary, we design and fabricate functionally graded metamaterials. These graded metamaterials exhibit behaviors such as energy localization and localized rotations, which are atypical of the corresponding boundary conditions. In the future, investigations on the role of incompatibilities in other moduli could reveal newer information regarding geometric frustration under other complex loading conditions. In supercell designs, which were created by tessellating an entire annular graded structure, we observed that the annular regions displayed non-local interactions leading to length-scale dependent behavior. Furthermore, the exploration of other supercell tessellations incorporating different interpolation schemes could potentially open up new avenues in the design of multi-scale metamaterials.
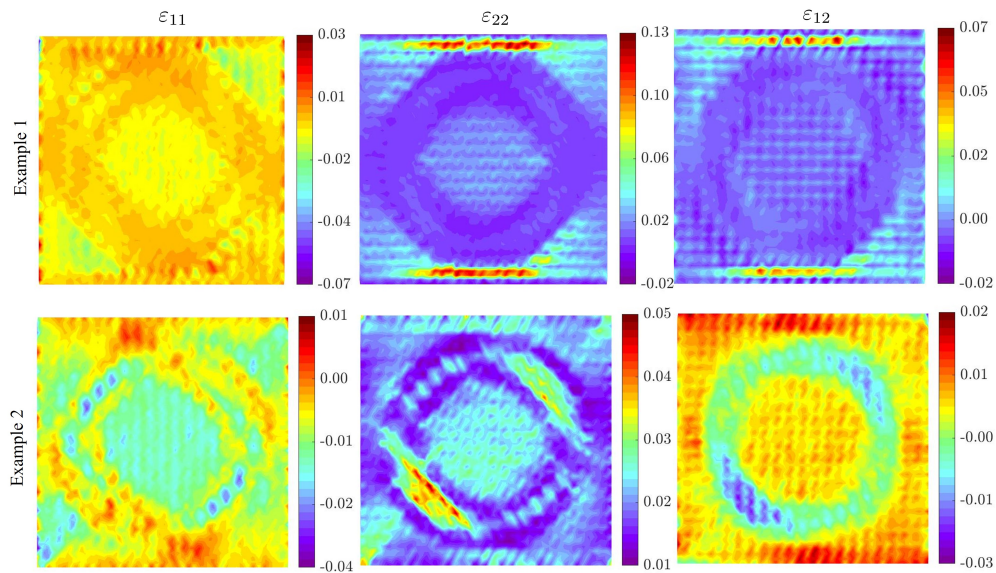
Figure 5.15: Experimentally measured strains obtained using DIC for example 1 shown in Fig. 7.1 and for example 2 shown in Fig. 5.14 that discuss non-affine deformations. In both examples, the strain contours indicate strain localization in the annular region which is different from the strain observed in the rest of the structure. Stresses are not plotted as they are difficult to obtain experimentally.
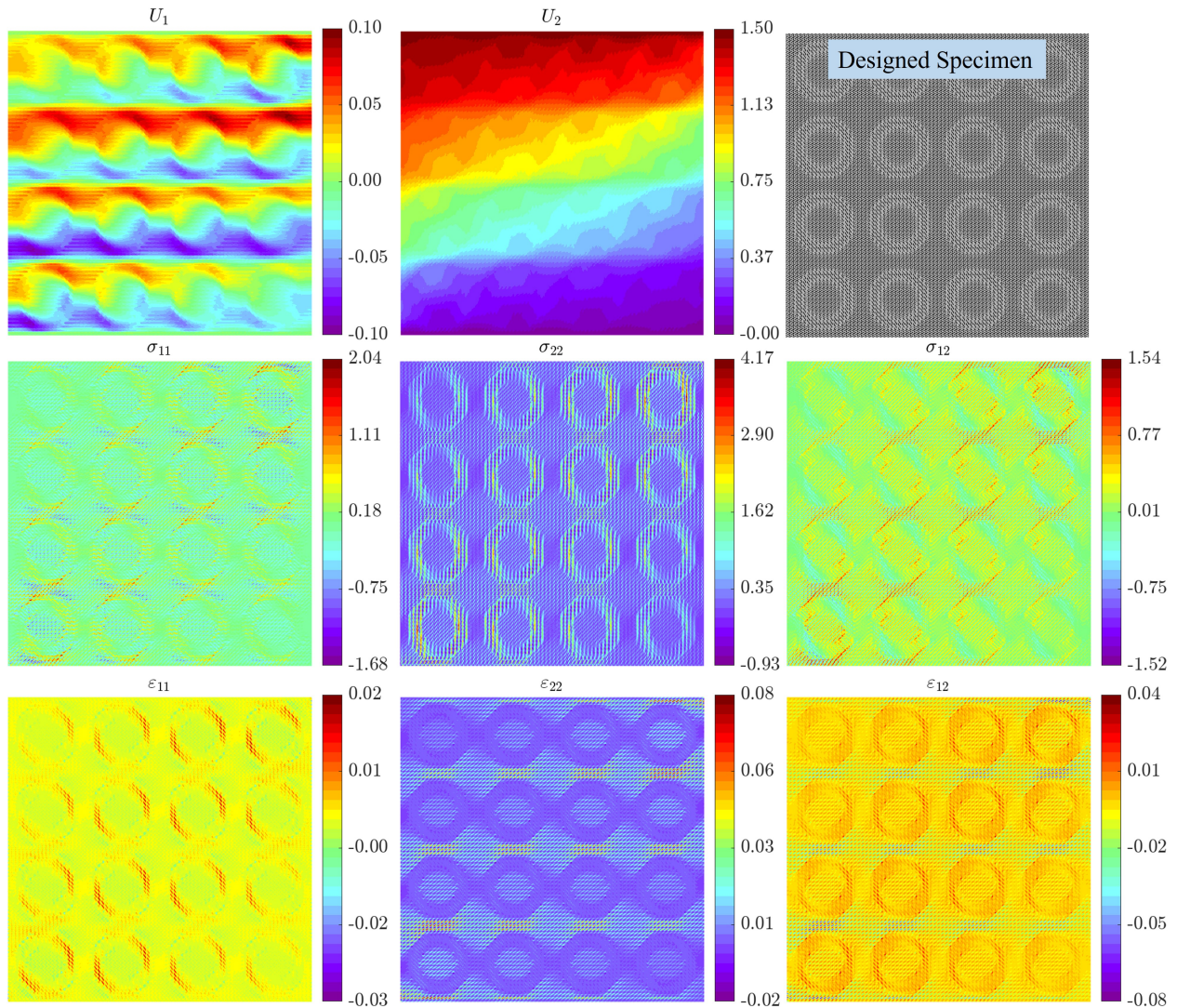
Figure 5.16: Mechanical behavior in a 4×4 supercell tessellation design subjected to tensile loading. The supercell consists of unit cells with opposing shear-normal coupling arranged in an annular interpolation scheme, which is the entire specimen considered in Fig. 7.1. The displacement contour U_1 displays multiple regions of rotation-like deformation arising from incompatibilities in the deformation modes of the unit cells. σ_{11}, σ_{22} contours (in units of MPa) display how these incompatibilities in C_{16}, C_{26} lead to alternative regions of compressive and tensile stresses in the tessellated supercell undergoing tensile loading. σ_{12} contour shows the rotation-induced shear stress localization. All the strain contours further corroborate the localization of the strains around the annular interface.
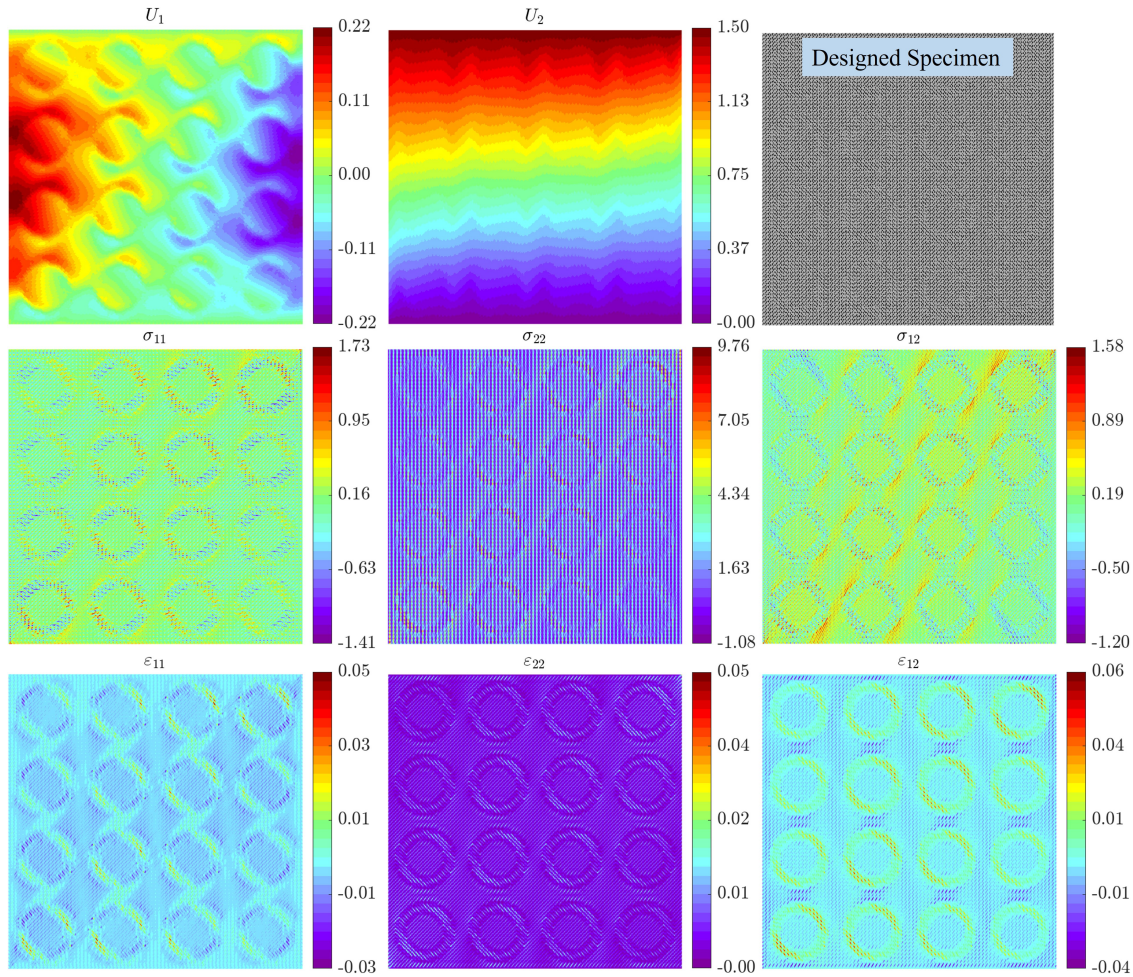
Figure 5.17: Mechanical behavior in a 4×4 supercell tessellation design subjected to tensile loading. The supercell consists of unit cells with opposing shear-normal coupling arranged in an annular interpolation scheme, which is the entire specimen considered in Fig. 5.14. The displacement contour U_1 displays multiple regions of rotation-like deformation arising from incompatibilities in the deformation modes of the unit cells. σ_{11}, σ_{22} contours (in units of MPa) display how these incompatibilities in C_{16}, C_{26} lead to alternative regions of compressive and tensile stresses in the tessellated supercell undergoing tensile loading. σ_{12} contour shows the rotation-induced shear stress localization. All the strain contours further corroborate the localization of the strains around the annular interface.

C h a p t e r   6

SHEAR-LONGITUDINAL WAVE MODE CONVERSION THROUGH GRADED ANISOTROPIC METAMATERIALS

Jagannadh Boddapati, Alexander Ogren, Jihoon Ahn, Gunho Kim, Chiara Daraio. (2024). "Shear-longitudinal wave mode conversion through functionally graded anisotropic metamaterials." In Preparation.

This chapter is temporarily embargoed.

Chapter 7

FUTURE OUTLOOK

7.1 Conclusion

In conclusion, this thesis extends our understanding of anisotropy elasticity tensors and shear-normal coupled deformations from theory to realizable structured materials. By changing the patterning in the unit cells with two simple isotropic phases, it is demonstrated that one could explore a very diverse range of anisotropic material properties. Theoretical calculations from the literature indicate the need for hierarchical materials to explore a diverse range of properties beyond these single-scale unit cells. Consequently, when the base properties of the phases are anisotropic, the range of achievable properties surpasses those of isotropic phases.

Anisotropy allows for very unique mechanical behavior such as (non-affine) rotational deformations under a simple tensile loading. Such non-affine deformations arise when there are incompatibilites in the effective anisotropic elastic moduli of the unit cells, especially the off-diagonal parameters of the elasticity tensors. Anisotropy also allows for hybridization of deformation modes as observed dispersion relations calculated from dynamic homogenization. We used the knowledge from designing functionally graded materials under static loading and utilized them to engineer wave propagation and convert waves from one polarization mode to the other.

These demonstrations using anisotropy open several interesting avenues such as multi-scale meta-materials with supercell tessellations. On the experimental side, characterizing full anisotropy always required use of multiple experiments. We demonstrated a method that uses the entire data available from a single tension experiment to measure all six stiffness parameters. These experiments further corroborated our designs exhibiting shear-normal coupling.

This fundamental understanding of shear-normal coupled deformations in structured materials further lays foundation for design of advanced transducers enabling complex mechanical character-ization. In the dynamic domain, this study will be valuable for structures aimed at impact mitigation and redirection (such as helmets), vibration and noise control, wearable and haptic devices. The heterogeneous distribution of unit cells with contrasting anisotropic behavior could play a significant role in enhancing the strength of structured materials beyond simple periodic tessellations. Some of these ideas are outlined in the next section.

7.2 Future outlook

The tools thus developed in this thesis open door for several exciting future directions.

Design approaches

2D structured materials: By using the structures with extreme shear-normal coupling embedded in a nanoindenter, nano-architected materials could be characterized under complex loading conditions beyond tension and compression. One could also study the range of possible anisotropic behaviors in nonlinear hyperelastic materials and the time-dependent viscoelastic two-phase composites with directional response. For example, with viscoelastic composites, one could elicit fast response in one direction and a really low response in another direction. Machine learning techniques such as diffusion model-based generative modeling could be used to enhance the existing database to discover new unit cells beyond user represenation especially at low fill fractions.

2.5D structured materials: By embedding the unit cell patterns, either periodic or functionally graded, onto plates and shells with arbitrary curvatures, one could study and engineer their directional response.

3D structured materials: In three dimensions, the elasticity tensor has 21 independent parameters. This anisotropy allows for shear-shear coupling: shear strains in one direction affect shear stresses in orthogonal directions. Extending the cosine function representation to generate 3D microstructures, one could study the limits of shear-shear coupling.

Multi-physics extensions: Another interesting avenue is in estimating bounds when there is multiple domains of physics controlling the deformation such as piezoelectric, flexoelectric tensors. Using inks with magnetically particles embedded in them, nonlinear nonlocal directional responses could be elicited.

Experimental methods

Parameter identification: The proposed parameter identification approach based on the Virtual fields method has the potential for measurements of elasticity parameters of complex, anisotropic, three-dimensional structured materials and composites with shear-shear couplings, and for the study of their nonlinear behavior. A further potential application of the method could be for parameter identification of constitutive tensors corresponding to different types of coupled behavior, such as generalized piezoelectric, flexoelectric, and piezomagnetic tensors. *Fabrication of hierarchical structures:* State-of-the-art printers such as Markforged Mark Two printers are capable of printing carbon-fiber reinforced parts with detailed control of the layup of the fibers. Therefore, this printing technique could be used to realize near-hierarchical-laminates-like structured materials.

Dynamic behavior

High-strain rate behavior: While graded designs exhibit phenomena like selective energy local-ization and strain localization, their behavior under dynamic loading at high strains has not been studied in this work. One could investigate the role of the heterogeneous defects introduced through gradients leading to energy dissipation and energy absorption. Computational modeling of these multi-scale structures requires efficient reduced order models much like in the design and analysis of multiscale modeling of metallic materials.

Mode conversion: In this work, a 1D graded design is used for the conversion of the shear-longitudinal waves. The dispersion behavior can be further expanded with the addition of nonlinear interactions by adding magnets, leading to nonlinear interactions. Mode-conversion in 2D and 3D strucutres open up new avenues for steering waves in complex paths.
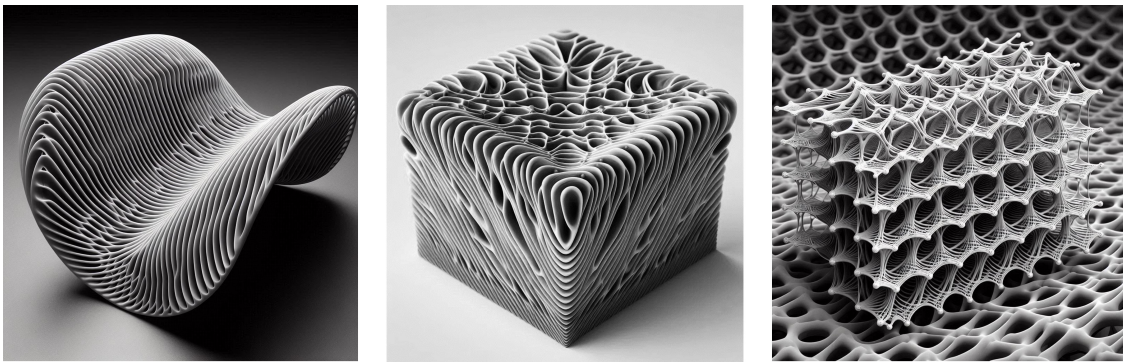
Figure 7.1: Potential future extensions of this thesis work include anisotropic metamaterial plates and shells, as well as three-dimensional anisotropic and hierarchical structures. (The images were generated using Microsoft Copilot image generator.)

Bibliography

[1]   Vikram S. Deshpande, Norman A. Fleck, and Michael F. Ashby. Effective properties of the octet-truss lattice material. *Journal of the Mechanics and Physics of Solids*, 49(8): 1747–1769, 2001.

[2]   Patrick Ziemke, Tobias Frenzel, Martin Wegener, and Peter Gumbsch. Tailoring the characteristic length scale of 3D chiral mechanical metamaterials. *Extreme Mechanics Letters*, 32: 100553, 2019.

[3]   Yuze Nian, Shui Wan, Mehmet Avcar, Ru Yue, and Mo Li. 3D printing functionally graded metamaterial structure: Design, fabrication, reinforcement, optimization. *International Journal of Mechanical Sciences*, 258:108580, November 2023. ISSN 0020-7403. doi: 10.1016/j.ijmecsci.2023.108580.

[4]   Liwei Wang, Jagannadh Boddapati, Ke Liu, Ping Zhu, Chiara Daraio, and Wei Chen. Mechanical cloak via data-driven aperiodic metamaterial design. *Proceedings of the National Academy of Sciences*, 119(13):e2122185119, March 2022. ISSN 0027-8424, 1091-6490. doi: 10.1073/pnas.2122185119.

[5]   Peter Chadwick, Maurizio Vianello, and Stephen C. Cowin. A new proof that the number of linear elastic symmetries is eight. *Journal of the Mechanics and Physics of Solids*, 49(11): 2471–2492, 2001.

[6]   Graeme W. Milton. Chapter 30: Properties of the G-closure and extremal families of composites. In *The Theory of Composites*, Classics in Applied Mathematics, pages 643–669. Society for Industrial and Applied Mathematics, January 2022. ISBN 978-1-61197-747-9. doi: 10.1137/1.9781611977486.ch30.

[7]   Cai Wenshan and Vladimir Shalaev. Optical metamaterials. Fundamentals and applications. *Springer. pp. xi*, 3(8):9, 2010.

[8]   Jae-Hwang Lee, Jonathan P. Singer, and Edwin L. Thomas. Micro-/Nanostructured mechanical metamaterials. *Advanced Materials*, 24(36):4782–4810, 2012. ISSN 1521-4095. doi: 10.1002/adma.201201644. _eprint: https://onlinelibrary.wiley.com/doi/pdf/10.1002/adma.201201644.

[9]   Johan Christensen, Muamer Kadic, Martin Wegener, Oliver Kraft, and Martin Wegener. Vibrant times for mechanical metamaterials. *MRS Communications*, 5(3):453–462, September 2015. ISSN 2159-6859, 2159-6867. doi: 10.1557/mrc.2015.51.

[10]   Amir A. Zadpoor. Mechanical meta-materials. *Materials Horizons*, 3(5):371–381, 2016. ISSN 2051-6347, 2051-6355. doi: 10.1039/C6MH00065G.

[11]   Katia Bertoldi, Vincenzo Vitelli, Johan Christensen, and Martin van Hecke. Flexible mechanical metamaterials. *Nature Reviews Materials*, 2(11):1–11, October 2017. ISSN 2058-8437. doi: 10.1038/natrevmats.2017.66. Number: 11 Publisher: Nature Publishing Group.

[12] James Utama Surjadi, Libo Gao, Huifeng Du, Xiang Li, Xiang Xiong, Nicholas Xuanlai Fang, and Yang Lu. Mechanical metamaterials and their engineering applications. *Advanced Engineering Materials*, 21(3):1800864, 2019. ISSN 1527-2648. doi: 10.1002/adem. 201800864. _eprint: https://onlinelibrary.wiley.com/doi/pdf/10.1002/adem.201800864.

[13] Roderic Lakes. Foam structures with a negative Poisson's ratio. *Science*, 235:1038–1041, 1987.

[14] George N. Greaves, Lindsay Greer, Roderic S. Lakes, and Tanguy Rouxel. Poisson's ratio and modern materials. *Nature Materials*, 10(11):823–837, November 2011. ISSN 1476-1122, 1476-4660. doi: 10.1038/nmat3134.

[15] Muamer Kadic, Tiemo Bückmann, Nicolas Stenger, Michael Thiel, and Martin Wegener. On the practicability of pentamode mechanical metamaterials. *Applied Physics Letters*, 100 (19):191901, May 2012. ISSN 0003-6951. doi: 10.1063/1.4709436. Publisher: American Institute of Physics.

[16] Nadège Kaina, Fabrice Lemoult, Mathias Fink, and Geoffroy Lerosey. Negative refractive index and acoustic superlens from multiple scattering in single negative metamaterials. *Nature*, 525(7567):77–81, September 2015. ISSN 1476-4687. doi: 10.1038/nature14678. Number: 7567 Publisher: Nature Publishing Group.

[17] Lorna J. Gibson and Michael F. Ashby. *Cellular solids: Structure and properties*. Cambridge University Press, 1999.

[18] Xiaoyu Zheng, Howon Lee, Todd H. Weisgraber, Maxim Shusteff, Joshua DeOtte, Eric B. Duoss, Joshua D. Kuntz, Monika M. Biener, Qi Ge, Julie A Jackson, et al. Ultralight, ultrastiff mechanical metamaterials. *Science*, 344(6190):1373–1377, 2014.

[19] Tobias A. Schaedler, Alan J. Jacobsen, Anna Torrents, Adam E. Sorensen, Jie Lian, Julia R. Greer, Lorenzo Valdevit, and Wiliam B. Carter. Ultralight metallic microlattices. *Science*, 334(6058):962–965, 2011.

[20] Guancong Ma and Ping Sheng. Acoustic metamaterials: From local resonances to broad horizons. *Science Advances*, 2(2):e1501595, 2016.

[21] Mehrdad Mohsenizadeh, Federico Gasbarri, Michael Munther, Ali Beheshti, and Keivan Davami. Additively-manufactured lightweight Metamaterials for energy absorption. *Materials & Design*, 139:521–530, 2018.

[22] Tiemo Bückmann, Michael Thiel, Muamer Kadic, Robert Schittny, and Martin Wegener. An elasto mechanical unfeelability cloak made of pentamode metamaterials. *Nature communications*, 5(1):1–6, 2014.

[23] Graeme W. Milton and Andrej V. Cherkaev. Which elasticity tensors are realizable? *Journal of Engineering Materials and Technology*, 117(4):483–493, October 1995. ISSN 0094-4289. doi: 10.1115/1.2804743.

[24] Wenwang Wu, Wenxia Hu, Guian Qian, Haitao Liao, Xiaoying Xu, and Filippo Berto. Mechanical design and multifunctional applications of chiral mechanical metamaterials: A review. *Materials & Design*, 180:107950, October 2019. ISSN 02641275. doi: 10.1016/j. matdes.2019.107950.

[25] Roman Kulagin, Yan Beygelzimer, Yuri Estrin, Artem Schumilin, and Peter Gumbsch. Architectured lattice materials with tunable anisotropy: Design and analysis of the material property space with the aid of machine learning. *Advanced Engineering Materials*, 22(12): 2001069, December 2020. ISSN 1438-1656, 1527-2648. doi: 10.1002/adem.202001069.

[26] Huina Mao, Romain Rumpler, Mathieu Gaborit, Peter Göransson, John Kennedy, Daragh O'Connor, Daniel Trimble, and Henry Rice. Twist, tilt and stretch: From isometric Kelvin cells to anisotropic cellular materials. *Materials & Design*, 193:108855, August 2020. ISSN 02641275. doi: 10.1016/j.matdes.2020.108855.

[27] Jan-Hendrik Bastek, Siddhant Kumar, Bastian Telgen, Raphaël N. Glaesener, and Dennis M. Kochmann. Inverting the structure–property map of truss metamaterials by deep learning. *Proceedings of the National Academy of Sciences*, 119(1):e2111505119, January 2022. doi: 10.1073/pnas.2111505119. Publisher: Proceedings of the National Academy of Sciences.

[28] Tobias Frenzel, Muamer Kadic, and Martin Wegener. Three-dimensional mechanical metamaterials with a twist. *Science*, 358(6366):1072–1074, November 2017. ISSN 0036-8075, 1095-9203. doi: 10.1126/science.aao4640.

[29] Wei Chen, Dong Ruan, and Xiaodong Huang. Optimization for twist chirality of structural materials induced by axial strain. *Materials Today Communications*, 15:175–184, June 2018. ISSN 2352-4928. doi: 10.1016/j.mtcomm.2018.03.010.

[30] Zhihao Yuan, Zhiming Cui, and Jaehyung Ju. Micropolar homogenization of wavy tetra-chiral and tetra-achiral lattices to identify axial–shear coupling and directional negative Poisson's ratio. *Materials & Design*, 201:109483, March 2021. ISSN 02641275. doi: 10.1016/j.matdes.2021.109483.

[31] Xiaoyue Ni, Xiaogang Guo, Jiahong Li, Yonggang Huang, Yihui Zhang, and John A. Rogers. 2D Mechanical metamaterials with widely tunable unusual modes of thermal expansion. *Advanced Materials*, 31(48):1905405, 2019. ISSN 1521-4095. doi: 10.1002/adma.201905405. _eprint: https://onlinelibrary.wiley.com/doi/pdf/10.1002/adma.201905405.

[32] Ruslan Guseinov, Connor McMahan, Jesús Pérez, Chiara Daraio, and Bernd Bickel. Programming temporal morphing of self-actuated shells. *Nature Communications*, 11(1):237, January 2020. ISSN 2041-1723. doi: 10.1038/s41467-019-14015-2. Number: 1 Publisher: Nature Publishing Group.

[33] Giada Risso, Maria Sakovsky, and Paolo Ermanni. Instability-driven shape forming of fiber reinforced polymer frames. *Composite Structures*, 268:113946, July 2021. ISSN 0263-8223. doi: 10.1016/j.compstruct.2021.113946.

[34] Filippo Agnelli, Grigor Nika, and Andrei Constantinescu. Design of thin micro-architectured panels with extension–bending coupling effects using topology optimization. *Computer Methods in Applied Mechanics and Engineering*, 391:114496, March 2022. ISSN 0045-7825. doi: 10.1016/j.cma.2021.114496.

[35] Young Kwan Ahn, Hyung Jin Lee, and Yoon Young Kim. Conical refraction of elastic waves by anisotropic metamaterials and application for parallel translation of elastic waves. *Scientific Reports*, 7(1):10072, December 2017. ISSN 2045-2322. doi: 10.1038/s41598-017-10691-6.

[36] Mingye Zheng, Xiaoning Liu, Yi Chen, Hongchen Miao, Rui Zhu, and Gengkai Hu. Theory and realization of nonresonant anisotropic singly polarized solids carrying only shear waves. *Physical Review Applied*, 12(1):014027, July 2019. ISSN 2331-7019. doi: 10.1103/PhysRevApplied.12.014027.

[37] Xiongwei Yang, Minwoo Kweun, and Yoon Young Kim. Monolayer metamaterial for full mode-converting transmission of elastic waves. *Applied Physics Letters*, 115(7):071901, August 2019. ISSN 0003-6951. doi: 10.1063/1.5109758. Publisher: American Institute of Physics.

[38] Mingye Zheng, Chung Il Park, Xiaoning Liu, Rui Zhu, Gengkai Hu, and Yoon Young Kim. Non-resonant metasurface for broadband elastic wave mode splitting. *Applied Physics Letters*, 116(17):171903, April 2020. ISSN 0003-6951. doi: 10.1063/5.0005408. Publisher: American Institute of Physics.

[39] Tobias Frenzel, Muamer Kadic, and Martin Wegener. Three-dimensional mechanical meta-materials with a twist. *Science*, 358(6366):1072–1074, 2017.

[40] Rongchang Zhong, Minghui Fu, Xuan Chen, Binbin Zheng, and Lingling Hu. A novel three-dimensional mechanical metamaterial with compression-torsion properties. *Composite Structures*, 226:111232, 2019.

[41] Graeme W. Milton. Some open problems in the theory of composites. *Philosophical Transactions of the Royal Society A: Mathematical, Physical and Engineering Sciences*, 379 (2201):20200115, May 2021. doi: 10.1098/rsta.2020.0115. Publisher: Royal Society.

[42] Robert Schittny, Tiemo Bückmann, Muamer Kadic, and Martin Wegener. Elastic measurements on macroscopic three-dimensional pentamode metamaterials. *Applied Physics Letters*, 103(23):231905, December 2013. ISSN 0003-6951. doi: 10.1063/1.4838663. Publisher: American Institute of Physics.

[43] John M. Considine, Fabrice Pierron, Kevin T. Turner, and David W. Vahey. General anisotropy identification of paperboard with virtual fields method. *Experimental Mechanics*, 54(8):1395–1410, October 2014. ISSN 1741-2765. doi: 10.1007/s11340-014-9903-1.

[44] Renaud Gras, Hugo Leclerc, Francois Hild, Stéphane Roux, and Julien Schneider. Identification of a set of macroscopic elastic parameters in a 3D woven composite: Uncertainty analysis and regularization. *International Journal of Solids and Structures*, 55:2–16, March 2015. ISSN 0020-7683. doi: 10.1016/j.ijsolstr.2013.12.023.

[45] Hyung Jin Lee, Heung Son Lee, Pyung Sik Ma, and Yoon Young Kim. Effective material parameter retrieval of anisotropic elastic metamaterials with inherent nonlocality. *Journal of Applied Physics*, 120(10):104902, September 2016. ISSN 0021-8979. doi: 10.1063/1.4962274. Publisher: American Institute of Physics.

[46] Chanyang Kim, Jin-Hwan Kim, and Myoung-Gyu Lee. A virtual fields method for identifying anisotropic elastic constants of fiber reinforced composites using a single tension test: Theory and validation. *Composites Part B: Engineering*, 200:108338, November 2020. ISSN 1359-8368. doi: 10.1016/j.compositesb.2020.108338.

[47] Filippo Agnelli, Pierre Margerit, Paolo Celli, Chiara Daraio, and Andrei Constantinescu. Systematic two-scale image analysis of extreme deformations in soft architectured sheets. *International Journal of Mechanical Sciences*, 194:106205, March 2021. ISSN 0020-7403. doi: 10.1016/j.ijmecsci.2020.106205.

[48] Arthur. G. Every and Wolfgang Sachse. Determination of the elastic constants of anisotropic solids from acoustic-wave group-velocity measurements. *Physical Review B*, 42(13):8196–8205, November 1990. doi: 10.1103/PhysRevB.42.8196. Publisher: American Physical Society.

[49] Marc Francois, Giuseppe Geymonat, and Yves Berthaud. Determination of the symmetries of an experimentally determined stiffness tensor: Application to acoustic measurements. *International Journal of Solids and Structures*, 35(31):4091–4106, November 1998. ISSN 0020-7683. doi: 10.1016/S0020-7683(97)00303-X.

[50] Da Chen, Kang Gao, Jie Yang, and Lihai Zhang. Functionally graded porous structures: Analyses, performances, and applications – A Review. *Thin-Walled Structures*, 191:111046, October 2023. ISSN 0263-8231. doi: 10.1016/j.tws.2023.111046.

[51] Lihao Tian, Bingteng Sun, Xin Yan, Andrei Sharf, Changhe Tu, and Lin Lu. Continuous transitions of triply periodic minimal surfaces. *Additive Manufacturing*, 84:104105, March 2024. ISSN 2214-8604. doi: 10.1016/j.addma.2024.104105.

[52] Siddhant Kumar, Stephanie Tan, Li Zheng, and Dennis M. Kochmann. Inverse-designed spinodoid metamaterials. *npj Computational Materials*, 6(1):73, December 2020. ISSN 2057-3960. doi: 10.1038/s41524-020-0341-6.

[53] Ajit Panesar, Meisam Abdi, Duncan Hickman, and Ian Ashcroft. Strategies for functionally graded lattice structures derived using topology optimisation for Additive Manufacturing. *Additive Manufacturing*, 19:81–94, January 2018. ISSN 2214-8604. doi: 10.1016/j.addma.2017.11.008.

[54] Emily D. Sanders, Anderson Pereira, and Glaucio H. Paulino. Optimal and continuous multilattice embedding. *Science Advances*, 7(16):eabf4838, April 2021. doi: 10.1126/sciadv.abf4838. Publisher: American Association for the Advancement of Science.

[55] Chi Wu, Junjie Luo, Jingxiao Zhong, Yanan Xu, Boyang Wan, Wenwei Huang, Jianguang Fang, Grant P. Steven, Guangyong Sun, and Qing Li. Topology optimisation for design

and additive manufacturing of functionally graded lattice structures using derivative-aware machine learning algorithms. *Additive Manufacturing*, 78:103833, September 2023. ISSN 2214-8604. doi: 10.1016/j.addma.2023.103833.

[56] Hao Li, Zhen Luo, Liang Gao, and Paul Walker. Topology optimization for functionally graded cellular composites with metamaterials by level sets. *Computer Methods in Applied Mechanics and Engineering*, 328:340–364, January 2018. ISSN 0045-7825. doi: 10.1016/j.cma.2017.09.008.

[57] Eric Garner, Helena M. A. Kolken, Charlie C. L. Wang, Amir A. Zadpoor, and Jun Wu. Compatibility in microstructural optimization for additive manufacturing. *Additive Manufacturing*, 26:65–75, March 2019. ISSN 2214-8604. doi: 10.1016/j.addma.2018.12.007.

[58] Jan Rychlewski. On Hooke's law. *Journal of Applied Mathematics and Mechanics*, 48(3):303–314, January 1984. ISSN 0021-8928. doi: 10.1016/0021-8928(84)90137-0.

[59] Thomas Chi-Tsai Ting. *Anisotropic elasticity: theory and applications*. Number 45. Oxford University Press on Demand, 1996.

[60] Nikolaos Karathanasopoulos, Francisco Dos Reis, Marianna Diamantopoulou, and Jean F. Ganghoffer. Mechanics of beams made from chiral metamaterials: Tuning deflections through normal-shear strain couplings. *Materials & Design*, 189:108520, April 2020. ISSN 0264-1275. doi: 10.1016/j.matdes.2020.108520.

[61] Francisco Dos Reis and Nikolaos Karathanasopoulos. Inverse metamaterial design combining genetic algorithms with asymptotic homogenization schemes. *International Journal of Solids and Structures*, 250:111702, August 2022. ISSN 0020-7683. doi: 10.1016/j.ijsolstr.2022.111702.

[62] Juan M Podestá, Carlos Gustavo Méndez, Sebastian Toro, and Alfredo Edmundo Huespe. Symmetry considerations for topology design in the elastic inverse homogenization problem. *Journal of the Mechanics and Physics of Solids*, 128:54–78, July 2019. ISSN 00225096. doi: 10.1016/j.jmps.2019.03.018.

[63] Sandra Forte and Maurizio Vianello. A unified approach to invariants of plane elasticity tensors. *Meccanica*, 49(9):2001–2012, September 2014. ISSN 0025-6455, 1572-9648. doi: 10.1007/s11012-014-9916-y.

[64] Nicolas Auffray and Pierre Ropars. Invariant-based reconstruction of bidimensional elasticity tensors. *International Journal of Solids and Structures*, 87:183–193, June 2016. ISSN 00207683. doi: 10.1016/j.ijsolstr.2016.02.013.

[65] Martin H. Sadd. *Elasticity: Theory, applications, and numerics*. Academic Press, 2009.

[66] Gilles A. Francfort and François Murat. Homogenization and optimal bounds in linear elasticity. *Archive for Rational Mechanics and Analysis*, 94(4):307–334, December 1986. ISSN 1432-0673. doi: 10.1007/BF00280908.

[67] Erik Andreassen and Casper Schousboe Andreasen. How to determine composite material properties using numerical homogenization. *Computational Materials Science*, 83:488–495, February 2014. ISSN 0927-0256. doi: 10.1016/j.commatsci.2013.09.006.

[68] John W. Cahn. Phase separation by spinodal decomposition in isotropic systems. *The Journal of Chemical Physics*, 42(1):93–99, January 1965. ISSN 0021-9606. doi: 10.1063/1.1695731. Publisher: American Institute of Physics.

[69] Celal Soyarslan, Swantje Bargmann, Marc Pradas, and Jörg Weissmüller. 3D stochastic bicontinuous microstructures: Generation, topology and elasticity. *Acta Materialia*, 149: 326–340, May 2018. ISSN 1359-6454. doi: 10.1016/j.actamat.2018.01.005.

[70] Dengsheng Zhang and Guojun Lu. Shape-based image retrieval using generic Fourier descriptor. *Signal Processing: Image Communication*, 17(10):825–848, November 2002. ISSN 0923-5965. doi: 10.1016/S0923-5965(02)00084-X.

[71] Shuangcheng Yu, Yichi Zhang, Chen Wang, Won-kyu Lee, Biqin Dong, Teri W. Odom, Cheng Sun, and Wei Chen. Characterization and design of functional quasi-random nanostructured materials using spectral density function. *Journal of Mechanical Design*, 139(7): 071401, July 2017. ISSN 1050-0472, 1528-9001. doi: 10.1115/1.4036582.

[72] Hubert Schreier, Jean-José Orteu, and Michael A. Sutton. *Image Correlation for Shape, Motion and Deformation Measurements: Basic Concepts,Theory and Applications*. Springer US, Boston, MA, 2009. ISBN 978-0-387-78746-6 978-0-387-78747-3. doi: 10.1007/978-0-387-78747-3.

[73] François Hild and Stéphane Roux. Comparison of local and global approaches to digital image correlation. *Experimental Mechanics*, 52(9):1503–1519, November 2012. ISSN 0014-4851, 1741-2765. doi: 10.1007/s11340-012-9603-7.

[74] Gilles Besnard, François Hild, and Stéphane Roux. "Finite-element" displacement fields analysis from digital images: application to Portevin–Le Châtelier bands. *Experimental Mechanics*, 46(6):789–803, December 2006. ISSN 1741-2765. doi: 10.1007/s11340-006-9824-8.

[75] Benoît Blaysat, Jan Neggers, Michel Grediac, and Frédéric Sur. Towards criteria characterizing the metrological performance of full-field measurement techniques: application to the comparison between local and global versions of DIC. *Experimental Mechanics*, 60(3): 393–407, March 2020. ISSN 1741-2765. doi: 10.1007/s11340-019-00566-4.

[76] Ole Sigmund. Systematic design of metamaterials by topology optimization. In R. Pyrz and J. C. Rauhe, editors, *IUTAM Symposium on Modelling Nanomaterials and Nanosystems*, pages 151–159, Dordrecht, 2009. Springer Netherlands. ISBN 978-1-4020-9557-3. doi: 10.1007/978-1-4020-9557-3_16.

[77] Alejandro R. Diaz and André Bénard. Designing materials with prescribed elastic properties using polygonal cells. *International Journal for Numerical Methods in Engineering*, 57(3):301–314, 2003. ISSN 1097-0207. doi: 10.1002/nme.677. _eprint: https://onlinelibrary.wiley.com/doi/pdf/10.1002/nme.677.

[78] Julian Panetta, Qingnan Zhou, Luigi Malomo, Nico Pietroni, Paolo Cignoni, and Denis Zorin. Elastic textures for additive fabrication. *ACM Transactions on Graphics*, 34(4):1–12, July 2015. ISSN 0730-0301, 1557-7368. doi: 10.1145/2766937.

[79] Christian Schumacher, Bernd Bickel, Jan Rys, Steve Marschner, Chiara Daraio, and Markus Gross. Microstructures to control elasticity in 3D printing. *ACM Transactions on Graphics*, 34(4):1–13, July 2015. ISSN 0730-0301, 1557-7368. doi: 10.1145/2766926.

[80] Igor Ostanin, George Ovchinnikov, Davi Colli Tozoni, and Denis Zorin. A parametric class of composites with a large achievable range of effective elastic properties. *Journal of the Mechanics and Physics of Solids*, 118:204–217, September 2018. ISSN 0022-5096. doi: 10.1016/j.jmps.2018.05.018.

[81] Thomas S. Lumpe and Tino Stankovic. Exploring the property space of periodic cellular structures based on crystal networks. *Proceedings of the National Academy of Sciences*, 118(7):e2003504118, February 2021. ISSN 0027-8424, 1091-6490. doi: 10.1073/pnas. 2003504118.

[82] Shengzhi Luan, Enze Chen, Joel John, and Stavros Gaitanaros. A data-driven framework for structure-property correlation in ordered and disordered cellular metamaterials. *Science Advances*, 9(41):eadi1453, October 2023. doi: 10.1126/sciadv.adi1453. Publisher: American Association for the Advancement of Science.

[83] Zhan Zhang, Christopher Brandt, Jean Jouve, Yue Wang, Tian Chen, Mark Pauly, and Julian Panetta. Computational design of flexible planar microstructures. *ACM Transactions on Graphics*, 42(6):1–16, December 2023. ISSN 0730-0301, 1557-7368. doi: 10.1145/ 3618396.

[84] Desai Chen, Mélina Skouras, Bo Zhu, and Wojciech Matusik. Computational discovery of extremal microstructure families. *Science Advances*, 4(1):eaao7005, January 2018. ISSN 2375-2548. doi: 10.1126/sciadv.aao7005.

[85] Xiaoyang Zheng, Xubo Zhang, Ta-Te Chen, and Ikumu Watanabe. Deep Learning in mechanical metamaterials: From prediction and generation to inverse design. *Advanced Materials*, 35(45):2302530, 2023. ISSN 1521-4095. doi: 10.1002/adma.202302530. _eprint: https://onlinelibrary.wiley.com/doi/pdf/10.1002/adma.202302530.

[86] Doksoo Lee, Wei (Wayne) Chen, Liwei Wang, Yu-Chin Chan, and Wei Chen. Data-driven design for metamaterials and multiscale systems: A review. *Advanced Materials*, 36(8):2305254, 2024. ISSN 1521-4095. doi: 10.1002/adma.202305254. _eprint: https://onlinelibrary.wiley.com/doi/pdf/10.1002/adma.202305254.

[87] Liwei Wang, Yu-Chin Chan, Faez Ahmed, Zhao Liu, Ping Zhu, and Wei Chen. Deep generative modeling for mechanistic-based learning and design of metamaterial systems. *Computer Methods in Applied Mechanics and Engineering*, 372:113377, December 2020. ISSN 0045-7825. doi: 10.1016/j.cma.2020.113377.

[88] Yunwei Mao, Qi He, and Xuanhe Zhao. Designing complex architectured materials with generative adversarial networks. *Science Advances*, 6(17):eaaz4169, April 2020. ISSN 2375-2548. doi: 10.1126/sciadv.aaz4169.

[89] Li Zheng, Konstantinos Karapiperis, Siddhant Kumar, and Dennis M. Kochmann. Unifying the design space and optimizing linear and nonlinear truss metamaterials by generative modeling. *Nature Communications*, 14(1):7563, November 2023. ISSN 2041-1723. doi: 10.1038/s41467-023-42068-x. Number: 1 Publisher: Nature Publishing Group.

[90] Charles Yang, Youngsoo Kim, Seunghwa Ryu, and Grace X. Gu. Using convolutional neural networks to predict composite properties beyond the elastic limit. *MRS Communications*, 9(2):609–617, June 2019. ISSN 2159-6859, 2159-6867. doi: 10.1557/mrc.2019.49. Publisher: Cambridge University Press.

[91] Marco Maurizi, Chao Gao, and Filippo Berto. Inverse design of truss lattice materials with superior buckling resistance. *npj Computational Materials*, 8(1):1–12, November 2022. ISSN 2057-3960. doi: 10.1038/s41524-022-00938-w. Number: 1 Publisher: Nature Publishing Group.

[92] Jan-Hendrik Bastek and Dennis M. Kochmann. Inverse design of nonlinear mechanical metamaterials via video denoising diffusion models. *Nature Machine Intelligence*, 5(12): 1466–1475, December 2023. ISSN 2522-5839. doi: 10.1038/s42256-023-00762-x. Number: 12 Publisher: Nature Publishing Group.

[93] Zvi Hashin and Shmuel Shtrikman. Note on a variational approach to the theory of composite elastic materials. *Journal of the Franklin Institute*, 271(4):336–341, April 1961. ISSN 00160032. doi: 10.1016/0016-0032(61)90032-1.

[94] Zvi Hashin and Shmuel Shtrikman. On some variational principles in anisotropic and nonhomogeneous elasticity. *Journal of the Mechanics and Physics of Solids*, 10(4):335–342, October 1962. ISSN 0022-5096. doi: 10.1016/0022-5096(62)90004-2.

[95] John R. Willis. Bounds and self-consistent estimates for the overall properties of anisotropic composites. *Journal of the Mechanics and Physics of Solids*, 25(3):185–202, June 1977. ISSN 0022-5096. doi: 10.1016/0022-5096(77)90022-9.

[96] Graeme W. Milton and Robert V. Kohn. Variational bounds on the effective moduli of anisotropic composites. *Journal of the Mechanics and Physics of Solids*, 36(6):597–629, January 1988. ISSN 0022-5096. doi: 10.1016/0022-5096(88)90001-4.

[97] Andrej V. Cherkaev and Leonid V. Gibiansky. Coupled estimates for the bulk and shear moduli of a two-dimensional isotropic elastic composite. *Journal of the Mechanics and Physics of Solids*, 41(5):937–980, May 1993. ISSN 0022-5096. doi: 10.1016/0022-5096(93) 90006-2.

[98] Grégoire Allaire and Robert V. Kohn. Optimal bounds on the effective behavior of a mixture of two well-ordered elastic materials. *Quarterly of Applied Mathematics*, 51(4):643–674, 1993. ISSN 0033-569X, 1552-4485. doi: 10.1090/qam/1247433.

[99] Graeme W. Milton and Mohamed Camar-Eddine. Near optimal pentamodes as a tool for guiding stress while minimizing compliance in 3d-printed materials: A complete solution to the weak G-closure problem for 3d-printed materials. *Journal of the Mechanics and Physics of Solids*, 114:194–208, May 2018. ISSN 0022-5096. doi: 10.1016/j.jmps.2018.02.003.

[100] Ole Sigmund. A new class of extremal composites. *Journal of the Mechanics and Physics of Solids*, 48(2):397–428, February 2000. ISSN 0022-5096. doi: 10.1016/S0022-5096(99)00034-4.

[101] Zhou Hu, Zhibo Wei, Kun Wang, Yan Chen, Rui Zhu, Guoliang Huang, and Gengkai Hu. Engineering zero modes in transformable mechanical metamaterials. *Nature Communications*, 14(1):1266, March 2023. ISSN 2041-1723. doi: 10.1038/s41467-023-36975-2. Number: 1 Publisher: Nature Publishing Group.

[102] Alexander B. Freidin. On new phase inclusions in elastic solids. *Journal of Applied Mathematics and Mechanics*, 87(2):102–116, February 2007. ISSN 00442267, 15214001. doi: 10.1002/zamm.200610305.

[103] Isaac V. Chenchiah and Kaushik Bhattacharya. The relaxation of two-well energies with possibly unequal moduli. *Archive for Rational Mechanics and Analysis*, 187(3):409–479, March 2008. ISSN 1432-0673. doi: 10.1007/s00205-007-0075-3.

[104] Mikhail A. Antimonov, Andrej Cherkaev, and Alexander B. Freidin. Phase transformations surfaces and exact energy lower bounds. *International Journal of Engineering Science*, 98: 153–182, January 2016. ISSN 00207225. doi: 10.1016/j.ijengsci.2015.10.004.

[105] Alexander B. Freidin and Leah L. Sharipova. Two-phase equilibrium microstructures against optimal composite microstructures. *Archive of Applied Mechanics*, 89(3):561–580, March 2019. ISSN 0939-1533, 1432-0681. doi: 10.1007/s00419-019-01510-7.

[106] Gilles A. Francfort and Graeme W. Milton. Sets of conductivity and elasticity tensors stable under lamination. *Communications on Pure and Applied Mathematics*, 47(3):257–279, 1994. ISSN 1097-0312. doi: 10.1002/cpa.3160470302. _eprint: https://onlinelibrary.wiley.com/doi/pdf/10.1002/cpa.3160470302.

[107] Graeme Milton, Marc Briane, and Davit Harutyunyan. On the possible effective elasticity tensors of 2-dimensional and 3-dimensional printed materials. *Mathematics and Mechanics of Complex Systems*, 5(1):41–94, March 2017. ISSN 2325-3444, 2326-7186. doi: 10.2140/memocs.2017.5.41.

[108] Marco Avellaneda. Optimal bounds and microgeometries for elastic two-phase composites. *SIAM Journal on Applied Mathematics*, 47(6):1216–1228, December 1987. ISSN 0036-1399. doi: 10.1137/0147082. Publisher: Society for Industrial and Applied Mathematics.

[109] Dhriti Nepal, Saewon Kang, Katarina M. Adstedt, Krishan Kanhaiya, Michael R. Bockstaller, L. Catherine Brinson, Markus J. Buehler, Peter V. Coveney, Kaushik Dayal, Jaafar A. El-Awady, Luke C. Henderson, David L. Kaplan, Sinan Keten, Nicholas A. Kotov, George C. Schatz, Silvia Vignolini, Fritz Vollrath, Yusu Wang, Boris I. Yakobson, Vladimir V. Tsukruk,

and Hendrik Heinz. Hierarchically structured bioinspired nanocomposites. *Nature Materials*, 22(1):18–35, January 2023. ISSN 1476-4660. doi: 10.1038/s41563-022-01384-1.

[110] Klaus Feyrer. *Wire Ropes*. Springer, Berlin, Heidelberg, 2007. ISBN 978-3-540-33821-5 978-3-540-33831-4. doi: 10.1007/978-3-540-33831-4.

[111] Javad Tavakoli and John J. Costi. Ultrastructural organization of elastic fibres in the partition boundaries of the annulus fibrosus within the intervertebral disc. *Acta Biomaterialia*, 68: 67–77, March 2018. ISSN 1742-7061. doi: 10.1016/j.actbio.2017.12.017.

[112] Gaia Volandri, Francesca Di Puccio, Paola Forte, and Costantino Carmignani. Biomechanics of the tympanic membrane. *Journal of Biomechanics*, 44(7):1219–1236, April 2011. ISSN 0021-9290. doi: 10.1016/j.jbiomech.2010.12.023.

[113] Stéphane Avril, Marc Bonnet, Anne-Sophie Bretelle, Michel Grédiac, François Hild, Patrick Ienny, Félix Latourte, Didier Lemosse, Stéphane Pagano, Emmanuel Pagnacco, and Fabrice Pierron. Overview of identification methods of mechanical parameters based on full-field measurements. *Experimental Mechanics*, 48(4):381–402, August 2008. ISSN 0014-4851, 1741-2765. doi: 10.1007/s11340-008-9148-y.

[114] Stéphane Roux and François Hild. Optimal procedure for the identification of constitutive parameters from experimentally measured displacement fields. *International Journal of Solids and Structures*, 184:14–23, February 2020. ISSN 00207683. doi: 10.1016/j.ijsolstr. 2018.11.008.

[115] Fabrice Pierron. Material Testing 2.0: A brief review. *Strain*, n/a (n/a):e12434, 2023. ISSN 1475-1305. doi: 10.1111/str.12434. _eprint: https://onlinelibrary.wiley.com/doi/pdf/10.1111/str.12434.

[116] Moritz Flaschel, Siddhant Kumar, and Laura De Lorenzis. Unsupervised discovery of interpretable hyperelastic constitutive laws. *Computer Methods in Applied Mechanics and Engineering*, 381:113852, August 2021. doi: 10.1016/j.cma.2021.113852.

[117] Robert Tibshirani. Regression shrinkage and selection via the lasso. *Journal of the Royal Statistical Society: Series B (Methodological)*, 58(1):267–288, January 1996. ISSN 00359246. doi: 10.1111/j.2517-6161.1996.tb02080.x.

[118] Moritz Flaschel, Siddhant Kumar, and Laura De Lorenzis. Discovering plasticity models without stress data. *npj Computational Materials*, 8(1):91, December 2022. ISSN 2057-3960. doi: 10.1038/s41524-022-00752-4.

[119] Enzo Marino, Moritz Flaschel, Siddhant Kumar, and Laura De Lorenzis. Automated identification of linear viscoelastic constitutive laws with EUCLID. *Mechanics of Materials*, 181:104643, June 2023. ISSN 01676636. doi: 10.1016/j.mechmat.2023.104643. URL https://linkinghub.elsevier.com/retrieve/pii/S0167663623000893.

[120] Moritz Flaschel, Siddhant Kumar, and Laura De Lorenzis. Automated discovery of generalized standard material models with EUCLID. *Computer Methods in Applied Mechanics and Engineering*, 405:115867, February 2023. ISSN 00457825. doi:

10.1016/j.cma.2022.115867. URL https://linkinghub.elsevier.com/retrieve/pii/S0045782522008234.

[121] Moritz Flaschel. *Automated Discovery of Material Models in Continuum Solid Mechanics*. PhD thesis, ETH Zurich, 2023. URL http://hdl.handle.net/20.500.11850/602750.

[122] Akshay Joshi, Prakash Thakolkaran, Yiwen Zheng, Maxime Escande, Moritz Flaschel, Laura De Lorenzis, and Siddhant Kumar. Bayesian-EUCLID: Discovering hyperelastic material laws with uncertainties. *Computer Methods in Applied Mechanics and Engineering*, 398: 115225, August 2022. ISSN 00457825. doi: 10.1016/j.cma.2022.115225.

[123] Hou Man and Tomonari Furukawa. Neural network constitutive modelling for non-linear characterization of anisotropic materials. *International Journal for Numerical Methods in Engineering*, 85(8):939–957, February 2011. ISSN 00295981. doi: 10.1002/nme.2999. URL https://onlinelibrary.wiley.com/doi/10.1002/nme.2999.

[124] Daniel Z. Huang, Kailai Xu, Charbel Farhat, and Eric Darve. Learning constitutive relations from indirect observations using deep neural networks. *Journal of Computational Physics*, 416:109491, September 2020. ISSN 00219991. doi: 10.1016/j.jcp.2020.109491. URL https://linkinghub.elsevier.com/retrieve/pii/S0021999120302655.

[125] Xin Liu, Fei Tao, Haodong Du, Wenbin Yu, and Kailai Xu. Learning constitutive relations from indirect observations using deep neural networks. *Journal of Applied Mechanics*, 87 (8):081003, August 2020. ISSN 0021-8936, 1528-9036. doi: 10.1115/1.4047036.

[126] Prakash Thakolkaran, Akshay Joshi, Yiwen Zheng, Moritz Flaschel, Laura De Lorenzis, and Siddhant Kumar. NN-EUCLID: Deep-learning hyperelasticity without stress data. *Journal of the Mechanics and Physics of Solids*, 169:105076, December 2022. ISSN 00225096. doi: 10.1016/j.jmps.2022.105076.

[127] Michel Grédiac. Principle of virtual work and identification. *Comptes Rendus de L Academie des Sciences Serie Ii*, (309(1)):1–5, 1989.

[128] Michel Grediac, Fabrice Pierron, Stéphane Avril, and Evelyne Toussaint. The virtual fields method for extracting constitutive parameters from full-field measurements: A review. *Strain*, 42(4):233–253, October 2008. ISSN 00392103. doi: 10.1111/j.1475-1305.2006.tb01504.x.

[129] Fabrice Pierron and Michel Grédiac. *The Virtual Fields Method*. Springer New York, New York, NY, 2012. ISBN 978-1-4614-1823-8 978-1-4614-1824-5. doi: 10.1007/978-1-4614-1824-5.

[130] Michel Grédiac and Fabrice Pierron. Applying the Virtual Fields Method to the identification of elasto-plastic constitutive parameters. *International Journal of Plasticity*, 22(4):602–627, April 2006. ISSN 07496419. doi: 10.1016/j.ijplas.2005.04.007.

[131] Nattawit Promma, Bumedijen Raka, Michel Grediac, Evelyne Toussaint, J-B Le Cam, Xavier Balandraud, and François Hild. Application of the virtual fields method to mechanical

characterization of elastomeric materials. *International Journal of Solids and Structures*, 46 (3):698–715, February 2009. ISSN 0020-7683. doi: 10.1016/j.ijsolstr.2008.09.025.

[132] Stéphane Avril, Michel Grédiac, and Fabrice Pierron. Sensitivity of the virtual fields method to noisy data. *Computational Mechanics*, 34(6):439–452, November 2004. ISSN 1432-0924. doi: 10.1007/s00466-004-0589-6.

[133] Fabrice Pierron, Stéphane Avril, and Vinh The Tran. Extension of the virtual fields method to elasto-plastic material identification with cyclic loads and kinematic hardening. *International Journal of Solids and Structures*, 47(22):2993–3010, November 2010. ISSN 0020-7683. doi: 10.1016/j.ijsolstr.2010.06.022.

[134] Aleksander Marek, Frances M. Davis, and Fabrice Pierron. Sensitivity-based virtual fields for the non-linear virtual fields method. *Computational Mechanics*, 60(3):409–431, September 2017. ISSN 0178-7675, 1432-0924. doi: 10.1007/s00466-017-1411-6.

[135] Raymond David Mindlin and N. N. Eshel. On first strain-gradient theories in linear elasticity. *International Journal of Solids and Structures*, 4(1):109–124, January 1968. ISSN 0020-7683. doi: 10.1016/0020-7683(68)90036-X.

[136] Paul Fischer, Markus Klassen, Julia Mergheim, Paul Steinmann, and Ralf Müller. Isogeometric analysis of 2D gradient elasticity. *Computational Mechanics*, 47(3):325–334, March 2011. ISSN 0178-7675, 1432-0924. doi: 10.1007/s00466-010-0543-8.

[137] Ugo Andreaus, Francesco dell'Isola, Ivan Giorgio, Luca Placidi, Tomasz Lekszycki, and Nicola Luigi Rizzi. Numerical simulations of classical problems in two-dimensional (non) linear second gradient elasticity. *International Journal of Engineering Science*, 108:34–50, November 2016. ISSN 00207225. doi: 10.1016/j.ijengsci.2016.08.003.

[138] Hua Yang, Dmitry Timofeev, B. Emek Abali, Baotong Li, and Wolfgang H. Müller. Verification of strain gradient elasticity computation by analytical solutions. *ZAMM–Journal of Applied Mathematics and Mechanics / Zeitschrift für Angewandte Mathematik und Mechanik*, July 2021. ISSN 0044-2267, 1521-4001. doi: 10.1002/zamm.202100023.

[139] J.-H. Kim, Frederic Barlat, Fabrice Pierron, and Myoung-Gyu Lee. Determination of anisotropic plastic constitutive parameters using the virtual fields method. *Experimental Mechanics*, 54(7):1189–1204, September 2014. ISSN 1741-2765. doi: 10.1007/s11340-014-9879-x.

[140] Marco Rossi, P Lava, F Pierron, D Debruyne, and Marco Sasso. Effect of DIC spatial resolution, noise and interpolation error on identification results with the VFM. *Strain*, 51(3):206–222, 2015. ISSN 1475-1305. doi: 10.1111/str.12134. _eprint: https://onlinelibrary.wiley.com/doi/pdf/10.1111/str.12134.

[141] Marie Dalémat, Michel Coret, Adrien Leygue, and Erwan Verron. Measuring stress field without constitutive equation. *Mechanics of Materials*, 136:103087, September 2019. ISSN 0167-6636. doi: 10.1016/j.mechmat.2019.103087.

[142] Ares J. Rosakis and K. Ravi-Chandar. On crack-tip stress state: An experimental evaluation of three-dimensional effects. *International Journal of Solids and Structures*, 22(2):121–134, January 1986. ISSN 0020-7683. doi: 10.1016/0020-7683(86)90002-8.

[143] Geon Lee, Seong-Jin Lee, Junsuk Rho, and Miso Kim. Acoustic and mechanical metamaterials for energy harvesting and self-powered sensing applications. *Materials Today Energy*, 37:101387, October 2023. ISSN 2468-6069. doi: 10.1016/j.mtener.2023.101387.

[144] Geon Lee, Dongwoo Lee, Jeonghoon Park, Yeongtae Jang, Miso Kim, and Junsuk Rho. Piezoelectric energy harvesting using mechanical metamaterials and phononic crystals. *Communications Physics*, 5(1):1–16, April 2022. ISSN 2399-3650. doi: 10.1038/s42005-022-00869-4. Publisher: Nature Publishing Group.

[145] Michael Rubinstein and Sergei Panyukov. Nonaffine deformation and elasticity of polymer networks. *Macromolecules*, 30(25):8036–8044, December 1997. ISSN 0024-9297. doi: 10.1021/ma970364k. Publisher: American Chemical Society.

[146] Wouter G Ellenbroek, Zorana Zeravcic, Wim van Saarloos, and Martin van Hecke. Nonaffine response: Jammed packings vs. spring networks. *Europhysics Letters*, 87(3):34004, August 2009. ISSN 0295-5075. doi: 10.1209/0295-5075/87/34004.

[147] Brahim Lemkalli, Muamer Kadic, Youssef El Badri, Sébastien Guenneau, Abdenbi Bouzid, and Younes Achaoui. Mapping of elastic properties of twisting metamaterials onto micropolar continuum using static calculations. *International Journal of Mechanical Sciences*, 254: 108411, September 2023. ISSN 0020-7403. doi: 10.1016/j.ijmecsci.2023.108411.

[148] Minh-Son Pham, Chen Liu, Iain Todd, and Jedsada Lertthanasarn. Damage-tolerant architected materials inspired by crystal microstructure. *Nature*, 565(7739):305–311, January 2019. ISSN 1476-4687. doi: 10.1038/s41586-018-0850-3. Publisher: Nature Publishing Group.

A p p e n d i x A

ASSEMBLY, OPERATION, AND MAINTENANCE OF SELECTIVE LASER SINTERING TECHNOLOGY-BASED 3D PRINTER

A.1 Introduction

Additive manufacturing, also known as 3D printing, is the process of creating objects layer by layer. Unlike subtractive manufacturing, where the material is removed from a solid block, additive manufacturing builds up the object. Additive manufacturing allows for rapid prototyping of complex geometries. Additive manufacturing encompasses a variety of techniques, including extrusion-based methods like Fused Deposition Modeling (FDM), vat polymerization techniques such as Stereolithography (SLA), digital light projection (DLP) technologies, and Selective Laser Sintering (SLS), which uses a laser to sinter powdered material, binding it together to create a solid structure.

Selective Laser Sintering (SLS) technology has revolutionized the field of additive manufacturing, as it allows 3D printing of metallic components. In SLS, the powder itself serves as the support material, making part cleaning easier. Unlike other 3D printing methods where separate support structures are needed, SLS parts can be removed from the powder bed without additional steps. The Sintratec Kit is the world's first and only assembly kit for Selective Laser Sintering (SLS) technology. Developed by Swiss SLS experts, it is designed for productive prototyping and is especially suitable for creating functional prototypes. The kit is easy to operate and comes with open parameters, allowing users to adjust settings such as laser speed and temperature for research purposes. It supports multiple materials, including standard Nylon (PA12) and flexible TPE, and offers open parameters for research purposes. Its features include a print volume of 110 x 110 x 110 mm (recommended: 90 x 90 x 90 mm), laser speed of 5 – 600 mm/s, layer height of 100 – 150 μm, dimensions of 520 x 520 x 360 mm, weight of 36 kg, chamber temperature range of 30 – 145 °C, and a surface temperature range of 80 – 180 °C.

In this section of the thesis, we delve into the intricate process of assembling a Sintratec Kit 3D printer. The assembly took place primarily during June and July of 2020, during the COVID-19 lockdown at Caltech. We then cover the printer's operation, from powder loading to part cleaning. Finally, we discuss the essential maintenance practices essential to ensure that the printer functions effectively.

A.2 Assembling the Sintratec Kit 3D Printer

The assembly of the Sintratec Kit printer involves several meticulous steps, which are explained in detail in this section.

1. **Frame Construction**: The initial step in assembling the 3D printer involves building the frame. The frame provides the necessary structural support, and thermal insulation for the entire system. The frame is primarily supported by 20×20 aluminum extrusions of various lengths. This step is indicated in Fig. A.1 (top row) with some crucial parts highlighted. The door assembly contains a laser-safe glass window to monitor the print chambers. The door also contains an insulation pad embedded inside it.

2. **Print Chamber Assembly**: The build chamber, where the actual printing occurs, is then assembled. This includes installing the build platform, powder coater, heating elements, and
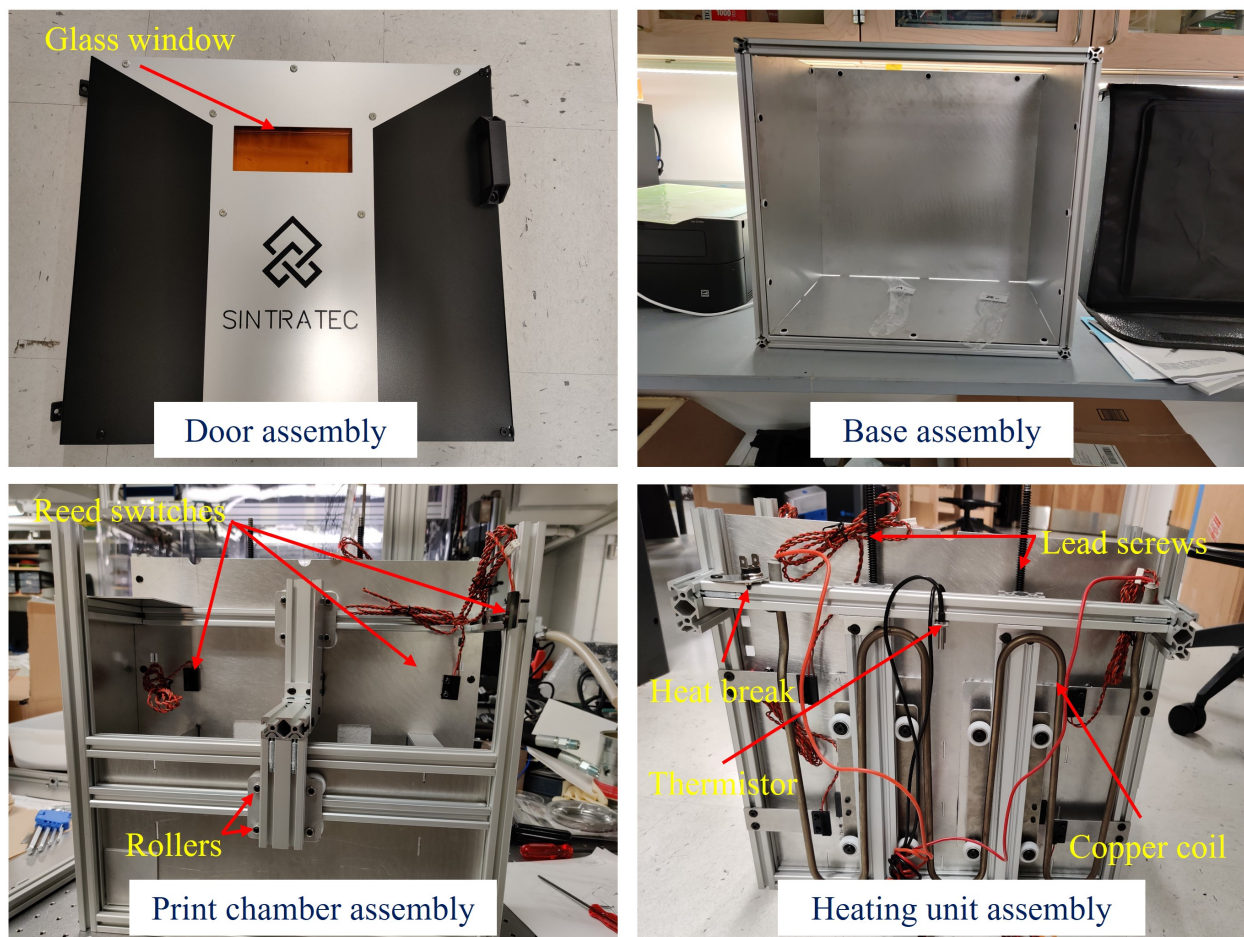

Figure A.1: Assembly sequence of the frame (top) and the print chamber (bottom).

temperature sensors. Accurate temperature control ensures proper sintering and prevents warping or other defects in the printed parts. The *lead screws* play a crucial role in the movement and positioning of the print beds. They are responsible for converting rotational motion from the stepper motors into linear motion, allowing precise vertical movement of the print bed during the printing process. The *reed switches* are used as sensors to detect the position of the powder beds, the coater, and the door. These switches are activated by a magnetic field, allowing them to provide precise feedback on the position and movement of the parts they monitor. These steps are indicated in Fig. A.1 (bottom row). *Powder Handling System*: The print chamber also contains the powder handling system, including the powder supply and recycling units, which is installed next. roper sealing and calibration are essential to prevent powder leakage and ensure efficient material usage. The sealing of powder beds is highlighted in Fig. A.4.

3. **Hat Assembly and Electronics**: The control electronics, including the main control board, motor drivers, heating lamps, and sensors, are then installed and connected to the core hat part of the printer. The hat part that faces the powder chamber also contains insulating pads. These steps are highlighted in the top two rows of Fig. A.2.

4. **Installation of Laser System**: Electronics also includes the galvanometer laser scanner system. The core component of the printer is its laser system. This step involves mounting the diode laser (2.3 W) and aligning it precisely with the optical path. Proper alignment is crucial as any deviation can result in inaccurate sintering and poor-quality prints. laser system also contains an IR sensor which measures the surface temperature directly. This is indicated in Fig. A.3. Certain subassemblies are highlighted further in Fig. A.4.

5. **Calibration and Testing**: Once all components are assembled, the printer undergoes a thorough calibration process. The screws on the Galvo scanners had to be adjusted manually first so that the laser fits the print bed precisely. Then a test part is printed. After printing a test part, its dimensions are input into the computer for precise calibration of the laser system. Then, the printer's firmware and software are configured to manage the printing process, control the laser, and monitor various parameters. This is indicated in Fig. A.5.
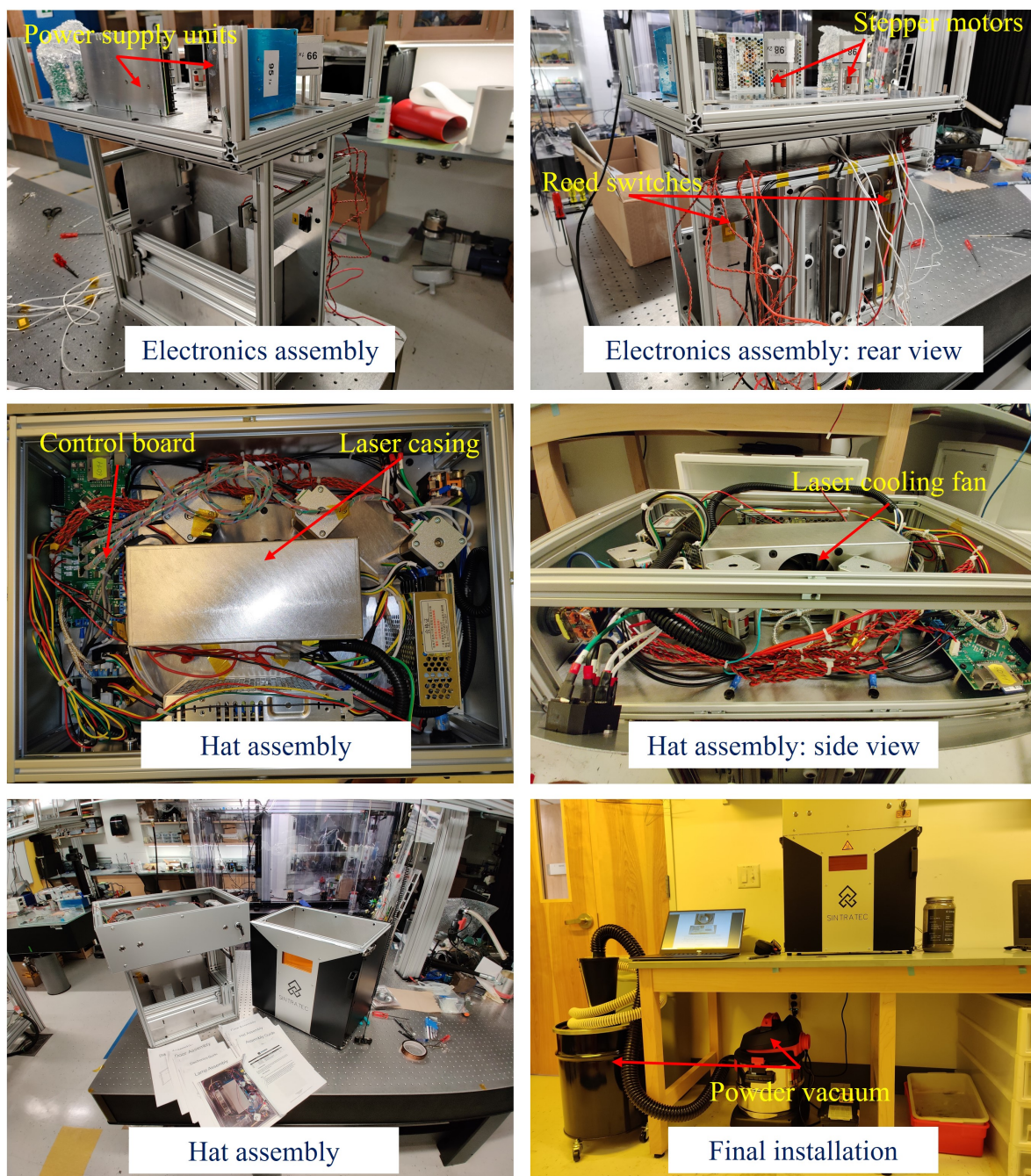
Figure A.2: Hat assembly sequence (top two rows) containing the electronics, stepper motors, power supply units, and laser. Final installation (last row).

A.3 Printing a part with the Sintratec Kit 3D Printer

Printing Instructions

1. The minimum resolution in the z-direction is 0.15 mm, determined by powder diameter and layer height. The resolution along the x-y direction is 0.2 mm, determined by the laser focus size. It is advisable to ensure that your minimum features are above 1 mm. If you require smaller sizes, be mindful of the cleaning process after printing.

2. Refer to the operation manual for detailed instructions on the recommended orientation of the STLs for efficient printing. For optimal results, consider orienting the part during printing to avoid having a single layer with an excessive sintering area.

3. There is a lead time of 100 minutes for the print chamber to reach the required chamber temperature ($\approx 180°$). Ensure this in your planning and schedule accordingly.

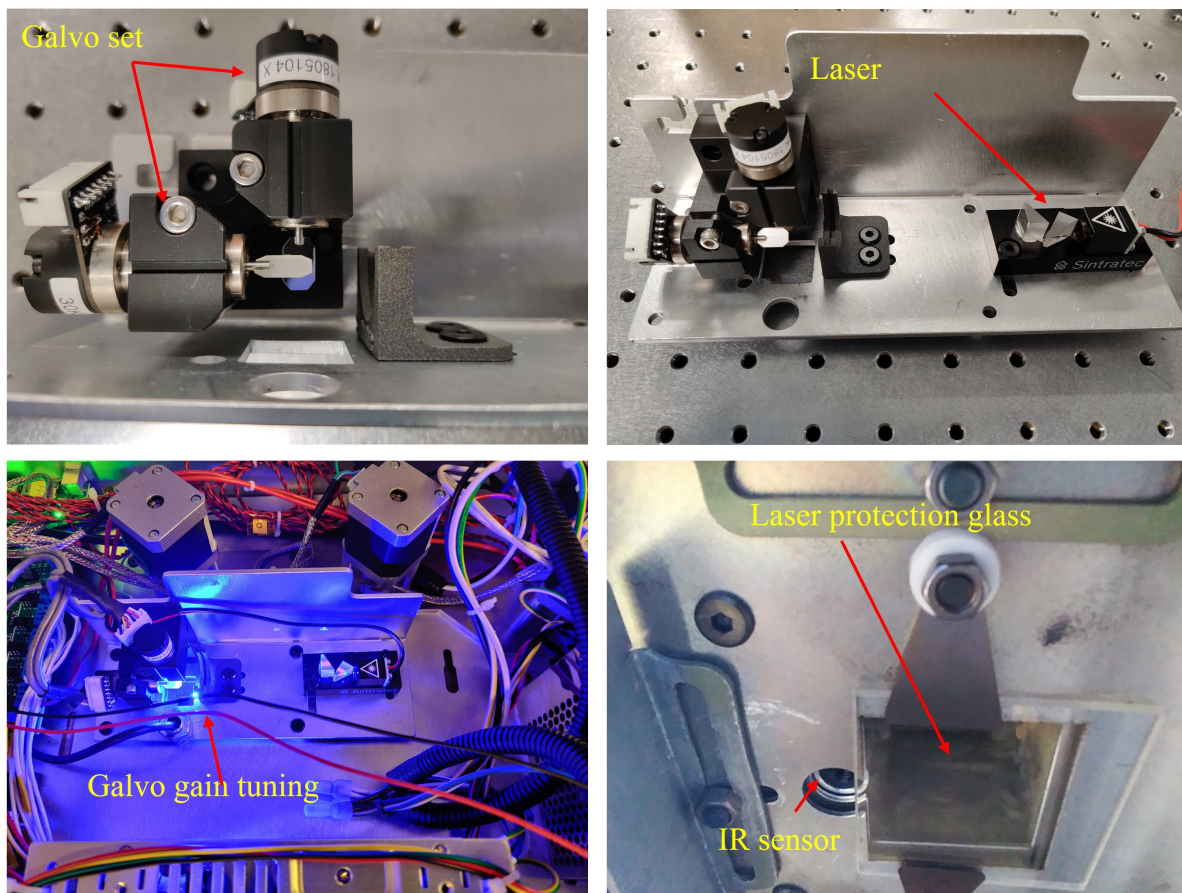4. Clean the laser glass before each print. Over time, soot and dust accumulate on the laser gas

Figure A.3: Laser and galvo set installation.

during each print cycle. This buildup can impact the printer's performance and the quality of printed parts. It is also advisable to clean the laser glass immediately after completing a print.

5. Add an extra 30 mm of powder material to the reservoir chamber beyond the required print height. Ensure that both the reservoir and the print bed have powder evenly distributed before starting the print. Check for any anomalies such as powder leakage or lamp malfunctioning.

6. Turn the laser key clockwise before starting the print.

7. Do not open the printer door while printing is in progress. Opening the door will shut off the laser and disrupt the print.

8. Avoid placing your hands into the printer immediately after the print is completed, as the print chamber will be very hot. Allow the printer to cool down before handling.
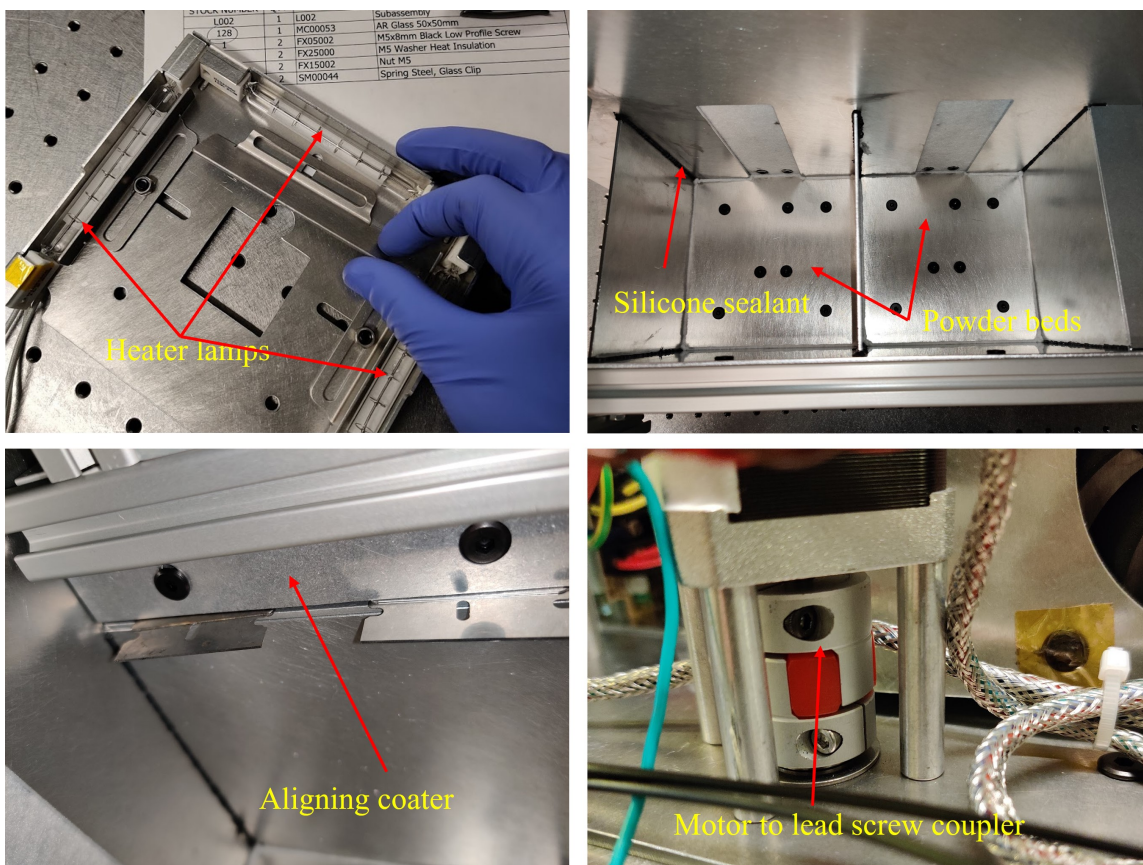

Figure A.4: Detailed look at some crucial sections of the printer.

9. Wear gloves whenever handling the powder or cleaning the printed parts. It is highly recommended to wear an N95 mask whenever the printer is in operation or while handling the powder.
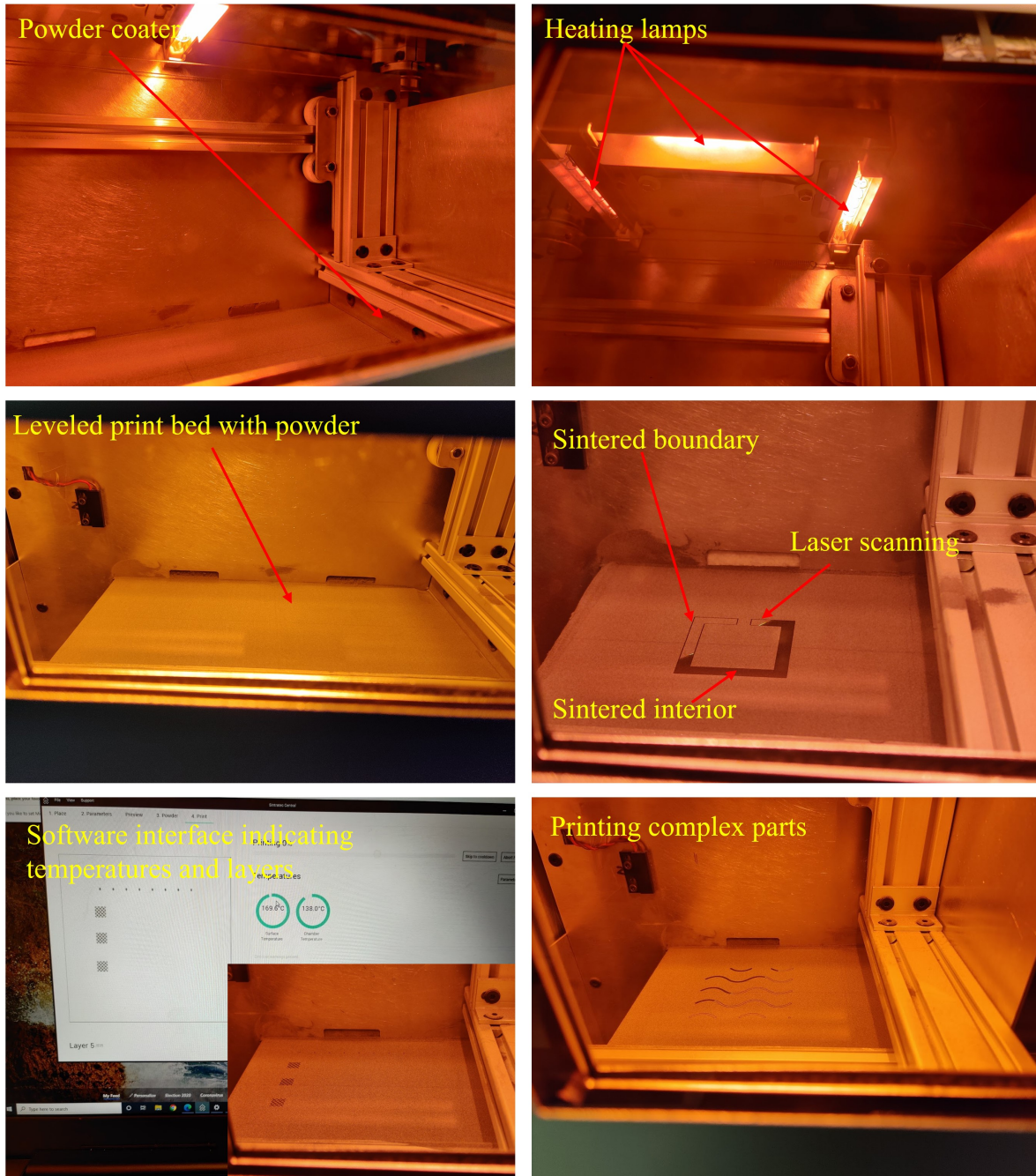

Figure A.5: Print chamber and print bed during the printing. The temperatures inside the chamber go as high as 150° C, while the sintering area that is exposed to the laser gets as hot as 210° C.

10. Vacuum the print bed and the left chamber that contains excessive powder after retrieving your printed part. Carefully sieve the cleaned powder and store it for reuse. It is recommended to not use the powder that went into the heating cycle inside the lamps again without mixing it with new powder. Otherwise, sintered parts tend to be very brittle and also often result in failed prints.

11. The part often requires removing the powder that acted as support during the printing process. Therefore, first, the part is cleaned using fine filing tools. Then the part is sandblasted using gsandblaster located in the GALCIT machine shop. Sandbalster containers very fine glass beads that are impinged at very high speeds on to the part. They erode the weak non-sintered hardened powder that acted as support material. This ensures a smooth surface finish for the part.
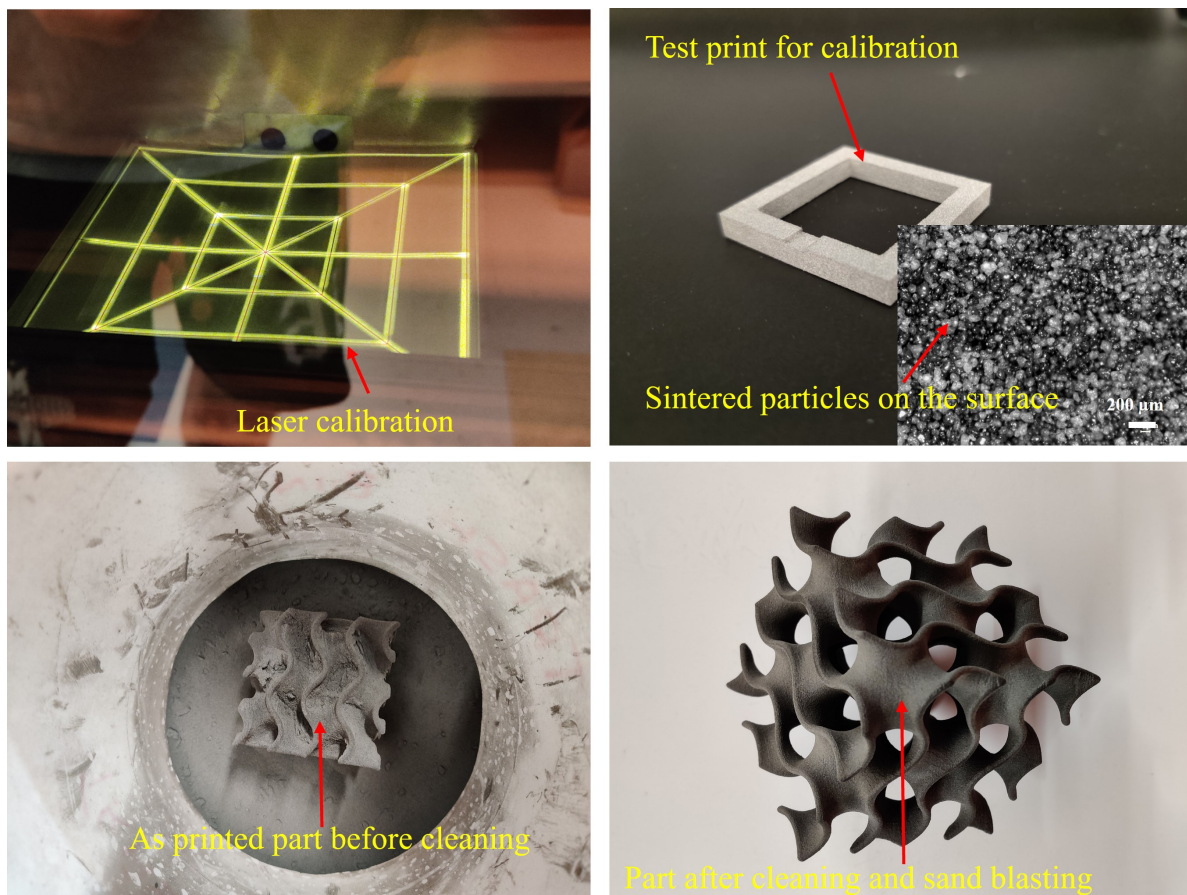

Figure A.6: Laser calibration and test print (top row). Printed part cleaning (bottom row).

A.4 Maintenance and troubleshooting of the Sintratec Kit 3D Printer

Regular maintenance is essential to keep the 3D printer in optimal working condition and to extend its lifespan.

Maintenance:

1. **Cleaning**: The build chamber, laser optics, and powder handling system require regular cleaning to prevent powder buildup and ensure accurate printing as shown in Fig. A.8. Special care must be taken to clean the laser lens and mirrors, as any contamination can affect the laser's performance. It is recommended to clean them atleast once every 5–10 prints.

2. **Inspection and Replacement of Wear Parts**: Components such as the laser, build platform, and heating elements are subject to wear and tear. Regular inspection and timely replacement of these parts are necessary to maintain the printer's performance. For instance, the laser tube might need replacement after a certain number of operating hours.
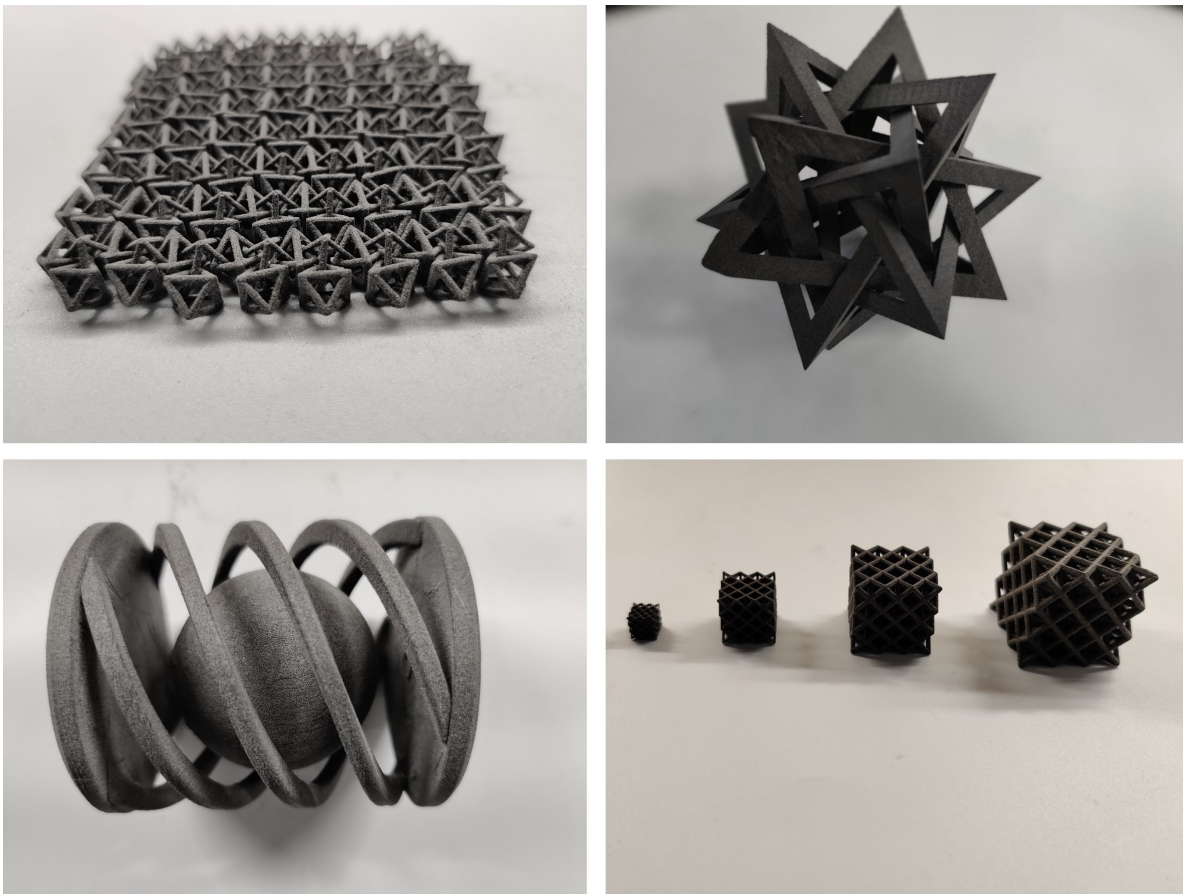

Figure A.7: Exemplary printed parts with distinct interlocked shapes and fine features.

Figure A.8: Maintenance and cleaning of the printer.

Troubleshooting:

Several issues arose with various components during the operation and the maintenance of the printer, as shown in Fig. 2.9. The reasons include

1. High-power cables from power supply units interfered with the stepper motors, necessitating the rerouting of the cables due to EMC issues.

2. The heat break sensor was positioned too close to the copper heater, resulting in incorrect readings. Its position had to be manually adjusted.

3. The accumulation of dust on the laser glass led to poor-quality prints or missing features in the parts.

4. The mechanical coupler that connects the motor to the lead screw, which moves the print chambers vertically, failed. This caused the print chambers to remain stationary while the software assumed they were moving, leading to homing issues with the powder print axis. Replacing the coupler screws was quite challenging due to their difficult-to-reach location.

5. The cable that moves the coater blade malfunctioned, resulting in the spring slipping over the pulley. The coater receded to the right during printing, causing a pileup of powder on the left, which reduced the build volume and hampered build time. Replacing the reed switch resolved the issue.

6. Despite proper sealing, powder leaked into the back of the print chambers. Over time, the screws securing the guiding rails to the back of the print chamber walls became loose, causing

this issue to recur approximately every 20 prints. It is recommended to tighten these screws during maintenance to prevent this problem.

7. The power supply and emergency stop switch experienced failures and required replacement. It was noted that these components are prone to failure with regular use. Higher-quality components would have been included in the kit to prevent such issues.

8. It was believed that software updates once caused unusual scaling of the STL files.

9. Failures in the reed switches led to homing issues with both the reservoir and coater axes, causing prints to abort midway. To prevent future faults, the reed switches were later repositioned slightly away from their original positions. The reed switches contain magnetic components that were prone to easy failure.

10. Nuts in crucial functional areas with significant vibration became loose. It would have been beneficial to apply a small amount of thread locker during assembly. Additionally, a torque wrench would have been useful to apply proper and uniform torque to all the screws.

11. Improper installation of the lamp shades led to overheating in certain areas. Additionally, reusing powder from the print chamber that had not been exposed to the laser caused warping of parts during subsequent prints.

A.5 Conclusion

Working on this project has been an invaluable experience, exposing me to a diverse range of engineering principles and significantly broadening my knowledge and skills. I gained a deeper understanding of heat transfer, which was crucial for managing the thermal aspects of the 3D printing process. Certain improvisations had to be made as the pictures shown in the initial manual were not up to date with the updated version of the printer design that was shipped. This experience enlightened me on the importance of modularity in product design, especially useful when troubleshooting and accessing intricate corners once everything is assembled. Additionally, I worked with optics for laser calibration, allowing me to fine-tune the laser's focus and ensure precise sintering. I also encountered and addressed challenges related to electromagnetic interference, ensuring the smooth operation of the printer's electronic components. This comprehensive experience has significantly broadened my engineering knowledge and skills. This accomplishment would not have been possible without the incredible help of Julian Cecil (from 3D Chimera), Petros Arakelian, and Alex Ogren.

Figure A.9: Troubleshooting the printer during regular operation.